EPFL

Thèse n° 10 365

MEMS-based Tunable Metasurface for Reflective Display Applications

Présentée le 23 février 2024

Faculté des sciences et techniques de l'ingénieur
Laboratoire de systèmes nano-électromécaniques
Programme doctoral en microsystèmes et microélectronique

pour l'obtention du grade de Docteur ès Sciences

par

Dorian Giraud HERLE

Acceptée sur proposition du jury

Prof. H. Shea, président du jury
Prof. L. G. Villanueva Torrijo, Prof. N. Quack, directeurs de thèse
Dr W. Noell, rapporteur
Prof. P. Steeneken, rapporteur
Prof. J. Brugger, rapporteur

École polytechnique fédérale de Lausanne

2024

MEMS-based Tunable Metasurface for Reflective Display Applications

Doctoral Thesis, 2023

Dorian Herle

École Polytechnique Fédérale de Lausanne

EPFL

MEMS-based Tunable Metasurface for Reflective Display Applications

by

Dorian Herle

Thesis Director: Luis Guillermo Villanueva
Thesis Co-Director: Niels Quack

Cover: The Rolex Learning Center at EPFL (Modified)
Style: EPFL Report Style, with modifications by Batuhan Faik Derinbay

EPFL

Acknowledgements

This thesis, a culmination of my academic journey at EPFL, has been a profoundly enriching experience, thanks to the support and guidance of many distinguished individuals. I am deeply grateful to Prof. Niels Quack for his exceptional supervision, his always positive attitude, motivational drive, and for creating a joyful and supportive group atmosphere. His dedication, evidenced by traveling from Australia for my private defense, and his valuable feedback from grant writing to thesis publication have been indispensable. I extend my heartfelt thanks to Prof. Guillermo Villanueva for "adopting" me into his group halfway through my journey, providing expert guidance in cleanroom work, and contributing significantly to my professional growth. I would also like to thank my jury members, Prof. Jürgen Brugger, Dr. Wilfried Noell, and Prof. Peter Steeneken, for their expertise and invaluable feedback. Next to my direct supervisors, special appreciation goes to Prof. Philippe Renaud and Prof. Olivier Parriaux. Prof. Renaud has been a supportive mentor for over eight years now, playing a crucial role in my decision to pursue a Ph.D. at EPFL, particularly with my own idea, offering ongoing support and numerous enriching discussions. Prof. Parriaux, whom I met early in my EPFL career, has enriched my research with numerous discussions, simulations, and private optics lectures. To both of you, I owe a great amount of gratitude. Additionally, I would like to express my profound gratitude to Prof. Olivier Martin for his invaluable assistance in the development of the phenomenological model and his exceptional guidance in writing my papers. From the same lab, the Nanophotonics and Metrology Laboratory, I am immensely thankful to Hsiang-Chu for his crucial help in measuring the reflection spectra of my devices. I also extend my sincere thanks to Andrei Kiselev for his guidance and assistance in understanding the physics of the device. A sincere thank you also goes to both the Q-Lab and ANEMS research groups for their part in my Ph.D. journey. In the Q-Lab, I am grateful to Beatrice Raball, Marcell Kiss, Teodoro Graziosi, Sichen Mi, Adrien Toros, Yu Zhang, Gergely Huszka, Anna Varini, Elena Losero, Duarte Silva, Luigi Basso, Hernán Furci, Anton Lagosh, Hamed Sattari, Micol Previde Massara, and Yuji Takabayashi for a stimulating and joyful 2.5 years. Hamed, Micol, and Yuji, in particular, have been exceptional colleagues and friends. To Hamed, also a particular thank you for your expert guidance during my Master's project and later in my Ph.D. on anything related to optics. Yuji, your unconditional support inside and outside the cleanroom, the numerous delicious dinner invitations, and the many fun times we had in the office! Thank you so much for being such a true friend. In ANEMS, I extend my gratitude to Seniz Küçük, Damien Maillard, Yara Abdela, Fatemeh Arefi, Furkan Ayhan, Saba Gholizadeh, Florian Hartmann, Marco Liffredo, Jasmin Spettel, Silvan Stettler, Federico Peretti, and Daniel Moreno. Dani, thank you for the fun times, our memorable conference in Belgium, and your help in anything lab-related. To this end, I would also like to thank Elena for organizing many enjoyable outings, and both of you for being such wonderful friends. I am also thankful to the excellent students I supervised: Laetitia Imstepf, Kilian Scheiwiller, Sara Chehtite, Lianyi Ni, and Sylvain El-Khoury. Lianyi's contributions to the collimator design and Sylvain's work on nano-trench filling have been particularly noteworthy. Then, also a big thank you to the CMi staff members, in particular to Cyrille Hibert with whom I discussed a large number of various process flows, and whose expert opinion has always helped me make educated decisions on how to improve or achieve certain fabrications. Next to the laboratories, I would also like to thank a few people, notably: Andrea, you made a significant part of my Ph.D. journey very special! Thank you so much, Sippi! Thank you to Tiberiu and Justin for the 'inck' project and friendship, Bartosz for contributions to the 'BOOCs' project, and the LMIS1 crew: Berke Erbas, Reza Farsi, André Chatel, Roberto Russo, and Pol Vila, as well as Annie and Mrudhula, for the numerous social events. Vero, thank you very much for the great times we shared and your excellent cakes! In addition to my academic circle, my heartfelt thanks extend beyond the boundaries of EPFL to the Klaeger Family—Corina, Andres, Amanda, and Adrian. Your role as my 'Swiss Family' has been invaluable, providing a sense of belonging and unwavering support throughout my entire journey at EPFL. To Amanda, a special merci pour tout, for the great times we've shared and our ongoing friendship. I also want to give a shout-out to Rafael for his enduring friendship, to Sam for his invaluable help in revising my thesis, and to Alex, who has been a constant presence and support

throughout what feels like my entire life. Lastly, my profound gratitude to my parents, Marina and Christoph, and my sisters, Livia and Clelia, for their unconditional support and love.

This journey would not have been the same without each of you. Thank you.

Abstract

In an era where portable electronic devices are indispensable for a wide range of activities, the need for displays that provide both long-lasting battery life and excellent visibility in different lighting conditions is increasingly important. Emissive displays, which are widely used in current technologies, face challenges in adapting to changing environmental lighting. Unlike the human visual system that naturally sustains a consistent perception of visual elements in varying lighting conditions, emissive displays struggle to adapt their brightness effectively to diverse ambient settings. This inefficiency leads to greater power consumption to keep the screen visible, especially in well-lit areas, which in turn shortens the device's battery life. The issue can further lead to eye strain, caused by the disparity in luminosity between the display and its immediate surroundings. Reflective displays emerge as a promising alternative that leverages, rather than tries to match, ambient light.

This thesis investigates the development of a MEMS-based technology designed for tunable metasurfaces, aimed at enhancing reflective displays in mobile devices. The MEMS system features a unique electrostatically actuated membrane. This membrane is distinctive for its array of holes, each housing a stationary amorphous silicon (aSi) pillar. The key innovation here is the ability to switch between a flat surface and a nanostructured surface. This switch is achieved by controlling the vertical movement of the membrane: when the membrane moves downwards, the aSi pillars protrude, creating a nanostructured surface. Conversely, when the membrane is in its original position, the top surface appears flat. The optical characteristics of this dynamic surface are analyzed using Rigorous Coupled-Wave Analysis (RCWA) simulations and integrated with particle-swarm optimization (PSO) to optimize the system's dimensions. This approach aims to exploit Mie resonance for enhanced absorption in the nanostructured state or Fresnel Reflection in the flat state to achieve optical contrast.

The research progresses through several stages, beginning with the development of a static prototype that uses amorphous silicon (aSi) nanopillars and flat areas to achieve a contrast ratio of 1:50 between reflective and absorptive states. Building on this initial work, a dynamic prototype featuring electrostatic actuation is successfully developed. The device achieves a notable contrast ratio of 1:3 and demonstrates a switching time of 54 ms. While the optical and mechanical performance present opportunities for further optimization due to strain-induced deformations affecting the geometry and high electric resistivity, they nevertheless showcase the prototype's capability to alter the optical response. Furthermore, the thesis delves into scalable manufacturing processes, with a strong emphasis on self-alignment methodologies. Various deposition techniques are scrutinized, and the feasibility of this self-aligned, scalable manufacturing process is experimentally validated, despite some unresolved actuation failures.

Additionally, the thesis incorporates a computational aspect, involving the development of a Python wrapper for commercial Rigorous Coupled-Wave Analysis software. This computational framework facilitates advanced geometric definitions, input configurations, and a wide range of post-simulation visualizations, from spectral data to near-field electromagnetic plots.

In summary, this thesis provides a comprehensive investigation into the technological feasibility and scalability of MEMS-based tunable metasurfaces as a promising avenue for future reflective displays, while also highlighting areas that require further research.

Keywords: MEMS, NEMS, Optics, Reflective Display, Metasurface

Zusammenfassung

Tragbare elektronische Geräte sind heute unverzichtbar und erfordern lange Akkulaufzeiten sowie gute Sichtbarkeit unter verschiedenen Lichtbedingungen. Allerdings haben traditionellen emissiven Displays wie LCD oder OLED oft Schwierigkeiten, sich an letztere anzupassen, und wenn doch, dann meist auf Kosten der Energieeffizienz. Im Vergleich zum adaptiven Sehvermögen des Menschen, das eine konsistente Wahrnehmung über ein breites Spektrum von Lichtbedingungen ermöglicht, können aktuelle emissive Display-Technologien sich nur bedingt anpassen. Diese Ineffizienz führt zu einem erhöhten Stromverbrauch, um die Sichtbarkeit aufrechtzuerhalten, insbesondere in hellen Umgebungen, und verkürzt so die Batterielebensdauer des Geräts. Zudem führt die Diskrepanz zwischen suboptimaler Helligkeitsanpassung des Displays und den variierenden Umgebungslichtbedingungen häufig zu einer Überanstrengung der Augen. Reflektierende Displays stellen eine vielversprechende Alternative dar. Die Technologie nutzt das Umgebungslicht, anstatt sich dessen anpassen zu müssen.

Diese Doktorarbeit widmet sich der Entwicklung einer innovativen Displaytechnologie mit reflektiven Pixeln auf MEMS-Basis. Diese ermöglichen einen dynamischen Wechsel der Oberflächenstruktur zwischen flach und nanostrukturiert. Dieser Ansatz verfolgt das Ziel, Mie-Resonanz für eine erhöhte Absorption im nanostrukturierten Zustand oder Fresnel-Reflexion im flachen Zustand zu nutzen, um einen optischen Kontrast zu erzielen. Zentrales Element dieses Systems, ist eine gelöcherte Membran, die in jedem Loch einen feststehenden, amorphen Silizium (aSi) Pfeiler beherbergt. Bewegt sich die Membran nach unten, treten die aSi-Pfeiler hervor und bilden so eine nanostrukturierte Oberfläche. Im Gegensatz dazu erscheint die Oberfläche flach, wenn die Membran in ihrer Ausgangsposition ist. Die optischen Eigenschaften dieser dynamischen Oberfläche werden mittels Rigorous Coupled-Wave Analysis (RCWA) Simulationen analysiert und in Kombination mit Partikelschwarmoptimierung (PSO) genutzt, um die Dimensionen des Systems zu optimieren.

Die Forschung durchläuft mehrere Stufen, beginnend mit der Entwicklung eines statischen Prototyps der das grundlegende Prinzip nachweist, dass nanostrukturierte Oberflächen zur Erzeugung der Absorption – sprich eines schwarzen Pixels – möglich ist. Ein Kontrastverhältnis von 1:50 zwischen reflektierenden flachen amorphes Silizium (aSi) und Licht absorbierende Nanosäulen wird erzielt. Es folgt ein dynamischer, elektrisch ansteuerbarer Prototyp, der ein Kontrastverhältnis von 1:3 erreicht. Die optische Leistung wird jedoch durch mechanische Verformungen beeinträchtigt, die die Geometrie und damit die Optik beinträchtigt. Die relativ langsame Schaltzeit ist dem hohen spezifischen Widerstand von amorphem Silizium zuzuschreiben. Schlussendlich befasst sich die Arbeit mit einem skalierbaren Herstellungsprozess, der es ermöglichen soll, eine große Anzahl an Pixeln – wie es in einem realen Display von Nöten ist – herzustellen. Es werden verschiedene Abscheidungsverfahren untersucht. Die Machbarkeit dieses selbstausrichtenden, skalierbaren Herstellungsverfahrens wird experimentell validiert.

Darüber hinaus beinhaltet die Arbeit einen computergestützten Aspekt durch den Einsatz von Partikelschwarmoptimierung und die Entwicklung eines Python-Wrappers für die kommerzielle Software zur optischen Simulation, die auf Basis der Rigorous Coupled-Wave Analysis arbeitet. Der Wrapper erleichtert geometrische Eingabekonfigurationen und bietet eine breite Palette von Post-Simulations-Visualisierungen, von Spektraldaten bis zu elektromagnetischen Nahfelddiagrammen.

Zusammenfassend fokussiert sich diese Arbeit auf die technologische Machbarkeit und Skalierbarkeit eines MEMS-basierten Elements, das durch dynamische Modulation der Oberflächenmorphologie die Variierung der Reflektionsintensität ermöglicht und somit potenziell als zentrales Pixelelement in einem reflektierenden Bildschirm Anwendung finden kann.

Stichwörter:MEMS, NEMS, Optik, Reflektierende Displays, Metasurface

Contents

1

Introduction

In today's world, the increasing portability of electronic devices has amplified the demand for displays that offer both long battery life and high visibility in a variety of lighting conditions. Most current devices use emissive display technology, which is less adept at posing as a solution. To understand why that might be the case, one has to delve into the intricacies of how emissive displays interact with the adaptive nature of human visual perception under varying ambient lighting conditions. The human visual system exhibits a remarkable ability to maintain a consistent perception of colors and brightness levels across varying lighting conditions, a phenomenon known as ”color constancy” and ”brightness constancy” [1]. This ability guarantees that a white object retains its perceived whiteness across a range of lighting conditions. An example of such an object is paper. The perception of it being white remains whether it is viewed indoors with softer lighting or outside under bright sunlight. This constancy occurs despite the absolute level of light reaching the eyes from the paper being vastly different in these scenarios. Emissive displays, by design, generate their own light, with a fixed luminance value. However, as ambient lighting conditions shift, the human visual perception of what constitutes ”white” in terms of luminance will adjust. In brighter ambient conditions, the ”white” produced by an emissive screen might begin to appear more gray or dull, as the human visual system has recalibrated its reference point for white based on the higher luminance levels of the ambient light. Thus, in bright conditions, an emissive display will have to produce more light to maintain a level of luminance contrast that aligns with the viewer's recalibrated perception of ”white.” The requirement to increase luminance output in brighter conditions presents a challenge, particularly for portable devices where energy efficiency is crucial, as it leads to increased power consumption, reducing the battery life of the device. Utilizing more efficient light generation such as organic light-emitting diodes (OLED) or micro-LED technology can partly lessen the effect, yet it remains an inevitable challenge. Moreover, eye strain is often caused by a severe luminosity difference between the monitor and the surrounding lighting, which can easily be the case with emissive displays that don't reach sufficient brightness levels.

Reflective display technology emerges as a more elegant solution to these challenges. Adhering to the adage, ”if you cannot beat them, join them,” reflective displays leverage ambient light instead of competing against it. Unlike emissive displays, which generate their own light, reflective displays utilize the surrounding light to show their image. Each of the pixels of a reflective display can change the amount (brightness) and/or the reflected wavelength (color) of the ambient light rays that bounce off its surface. In that sense, printed media, such as a book, can be seen as static versions of a reflective screen, where the black ink absorbs most of the incoming light and the white paper reflects it, creating a visible discernible contrast in any lighting condition. Within the years there has been a vast amount of different propositions on how to build reflective displays, only a few such as reflective liquid crystal displays (LCD) or micro-capsule electrophoretic displays have seen commercial success. A commonplace example of reflective LCD technology is observed in typical calculator screens, which remain legible even under direct sunlight without the necessity of a backlight. Transitioning to a more sophisticated implementation, Amazon's Kindle e-readers utilize micro-capsule electrophoretic display technology, commonly referred to as E Ink (from the eponymous company), to provide a paper-like reading experience. Readability in the dark is assured through a dedicated

front-light. The relatively low reflection of around 30% for reflective LCDs and the slow switching times of about 120 ms for electrophoretic displays have led to continued research efforts to find more performing solutions.
The aim of this thesis is to suggest a Micro-Electro Mechanical Systems (MEMS) based technology that could have potential applications as reflective displays for mobile devices. More specifically, this technology is a MEMS-based tunable metasurface, capable of switching the reflective state of each pixel. The term "meta" originates from the ancient Greek word "$\mu\varepsilon\tau\alpha$", which means "beyond", "after", or "behind". This etymological background can still be seen in classical terms like "metaphysics". In this context, the translation of "beyond" is appropriate, basically stating that the technology ventures beyond the conventional surface properties. Classical materials exhibit a narrow set of optical properties, and thus often fail to address the need for the ever-growing demand in performance and miniaturization. On the contrary, specially designed subwavelength structures permit an unprecedented manipulation of the constitutive parameters, namely, the electrical permittivity, ϵ, and the magnetic permeability, μ. Consequently, metasurfaces have paved the way for novel advancements across a spectrum of applications. Recent demonstrations encompass femtomolar bio-sensing for antibody and antigen detection [2], high-resolution optical microscope imaging at the diffraction limit enabled by flat metasurface lenses [3], improving the inspection of materials with novel short-wave infrared imagers [4], unprecedented 100K DPI images [5] or THz bandpass filter for medical use and security screening [6]. These cited examples are passive components. In this thesis, the interest lies in active components. Metasurfaces alter the electromagnetic response through both material and geometric attributes. Active modulation techniques target these two fundamental aspects to induce desired changes [7], opening up new venues. Next to reflective displays, other application fields of tunable metasurfaces are, for example, optical beam steering for Light Detection and Ranging [8] and laser machining. On a material level approach, different methods can be employed to modify the refractive index of the material, such as utilizing phase change mechanisms [9], incorporating non-linear materials [10] or liquid crystals [11]. Conversely, geometric modifications can be attained through a multitude of approaches encompassing the stretching of flexible substrates [12], or more broadly, via the employment of MEMS-based technology [13]. MEMS technology, in particular, harbors substantial potential for metasurface tuning as it facilitates pronounced alterations in the local field, thus providing a vast range of electromagnetic responses, rendering it a formidable option for the advancement of metasurface modulation.

1.1. Concept

In this thesis, the alteration of a surface's reflectivity is accomplished through the use of MEMS. The key idea is to switch between a flat reflective surface and a nanostructured absorptive surface. This transformation is realized as follows: As visualized in Figure 1.1, a suspended membrane is perforated with multiple holes. Within each hole, a nanopillar is situated, separated from the membrane by a predetermined gap and anchored to the substrate. In its ideal state, the top surfaces of the membrane and the nanopillars align, presenting a nearly continuous flat surface, interrupted only by the ring openings caused by the gap. In the actuated state, electrostatic forces are utilized to draw the membrane downward, causing the nanopillars to protrude into incoming light and effectively create a sub-micron roughness on the surface. Essentially, a MEMS-based tunable metasurface is envisioned that allows for dynamically tuning the absorption of such, thereby controlling the amount of light reflected, creating bright and dark states. Combining multiple of these devices can create a segmented or pixelated display unit. From a material perspective, silicon is an excellent candidate for the proposed tunable metasurface. It is the most abundantly used element in microtechnology, offering many established processing methods. Black silicon is a commonly used term to describe nano- or microstructured silicon that shows a high amount of light absorption, rendering the surface dark black to the naked eye [14]. It has found applications in solar cells [15], photoelectric catalytic substrates [16], and photodetectors [17]. From a manufacturing point of view, amorphous silicon exhibits distinct advantages over crystalline silicon, such as deposition on topography, compatibility with a wide range of materials, and process temperatures. Thus, in this thesis, the primary focus lies on a device with amorphous silicon (aSi) nanopillars and an aSi membrane.

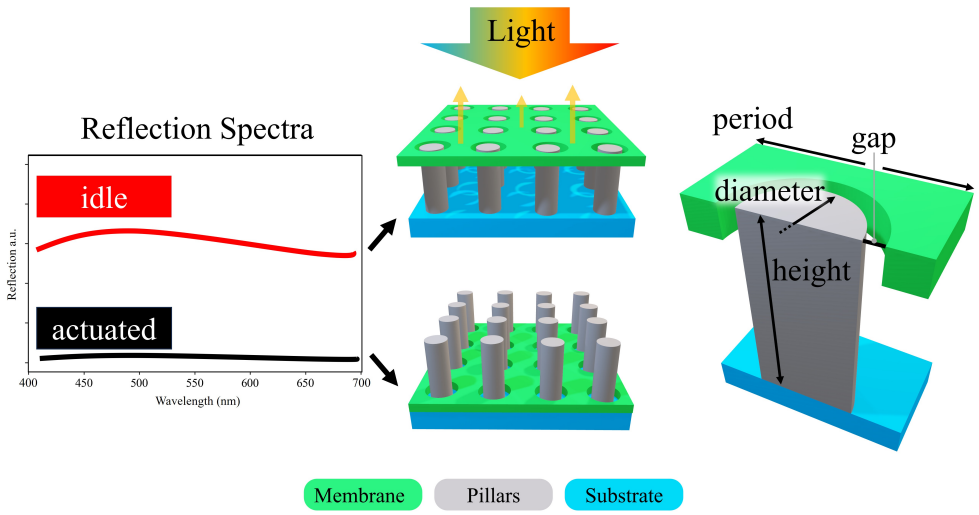

Figure 1.1: Concept visualization. MEMS-based tunable reflectivity by changing from a flat surface to a nanostructured surface. This is accomplished using a membrane (A) interleaved with a nanopillar array (B) that can move along the axis of said array, thereby going from a flat idle state to an actuated state to a structured state. Substrate (C) should be a dielectric isolation layer.

In the investigation of the underlying physics of the proposed concept, the device design is initially simplified, as illustrated in Figure 1.2a. Initially, the gap between the pillars and the membrane is omitted for simplification. In the idle state, when the membrane is at the top, the configuration essentially becomes an amorphous silicon (aSi) layer, provided the membrane is optically thick. Subsequently, RCWA simulations reveal that in intermediate states, the membrane serves as an optical cut-off, rendering any features below it optically irrelevant. As demonstrated in Fig. 1.2b, the far-field reflection spectrum in these intermediate states closely resembles that observed with nanopillars on an aSi substrate. In this case, the height of the nanopillars corresponds to their extent of protrusion beyond the membrane. Given these observations, the phenomenological model is further simplified to consist of an array of nanopillars on an aSi substrate for the actuated state, and simple bulk aSi for the idle state.

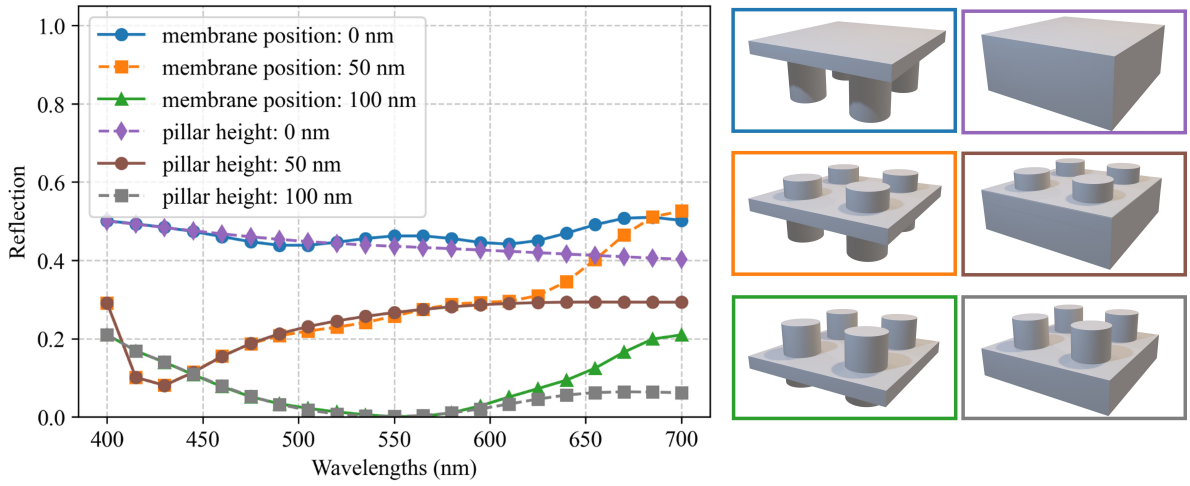

Figure 1.2: Simplified geometrical model of the device for investigating its underlying physics. Exemplary RCWA simulated reflection spectra for different membrane positions from the top, and corresponding pillar heights on an aSi substrate, indicating that the far-field reflection spectra closely resemble that of nanopillars on an aSi substrate. Geometry: period of 400 nm, diameter of 260 nm.

Light absorption in an array of aSi nanopillars is influenced by resonance-induced absorption, which draws its name from Gustave Mie's seminal work on electromagnetic radiation scattering by small entities [18]. This resonance effectively extends the light path within the material, resulting in amplified absorption, especially in lossy materials like aSi. As shown in Figure 1.3, the reflection dips, and the corresponding resonance wavelengths shift towards the red end of the spectrum as the diameter of the nanopillars increases (from 50 nm up to 200 nm). This trend mirrors the redshift behavior seen in Mie resonances for standalone nanoparticles [19]. The pronounced dip at 400 nm, which is equal to the array pitch, can be described by Rayleigh anomaly [20], [21].

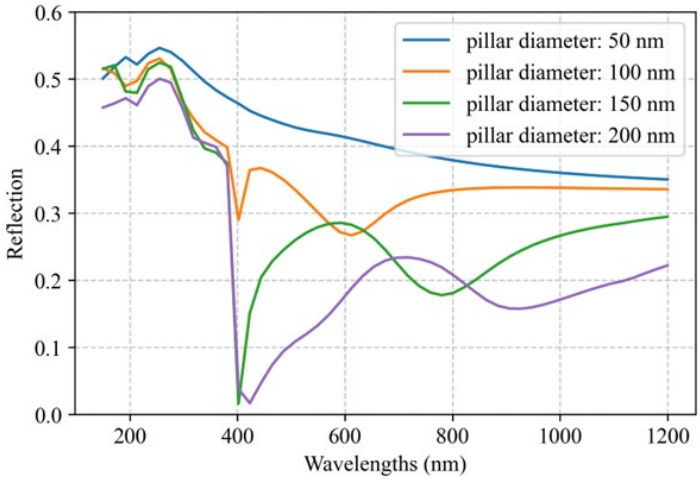

Figure 1.3: Redshift in Reflection Minima for aSi Nanopillar Arrays of Varying Diameters. The plot illustrates a redward shift in resonance wavelengths as nanopillar diameter increases from 50 nm to 200 nm, in agreement with Mie theory. A distinct dip at 400 nm corresponds to the array pitch and is explained by Rayleigh anomalies [21].

Hereafter, the influence of the different geometric parameters on the spectrum-averaged absorption is analyzed. Figure 1.4 analyzes the relation between the diameter-to-period ratio and the pillar height for different periods.

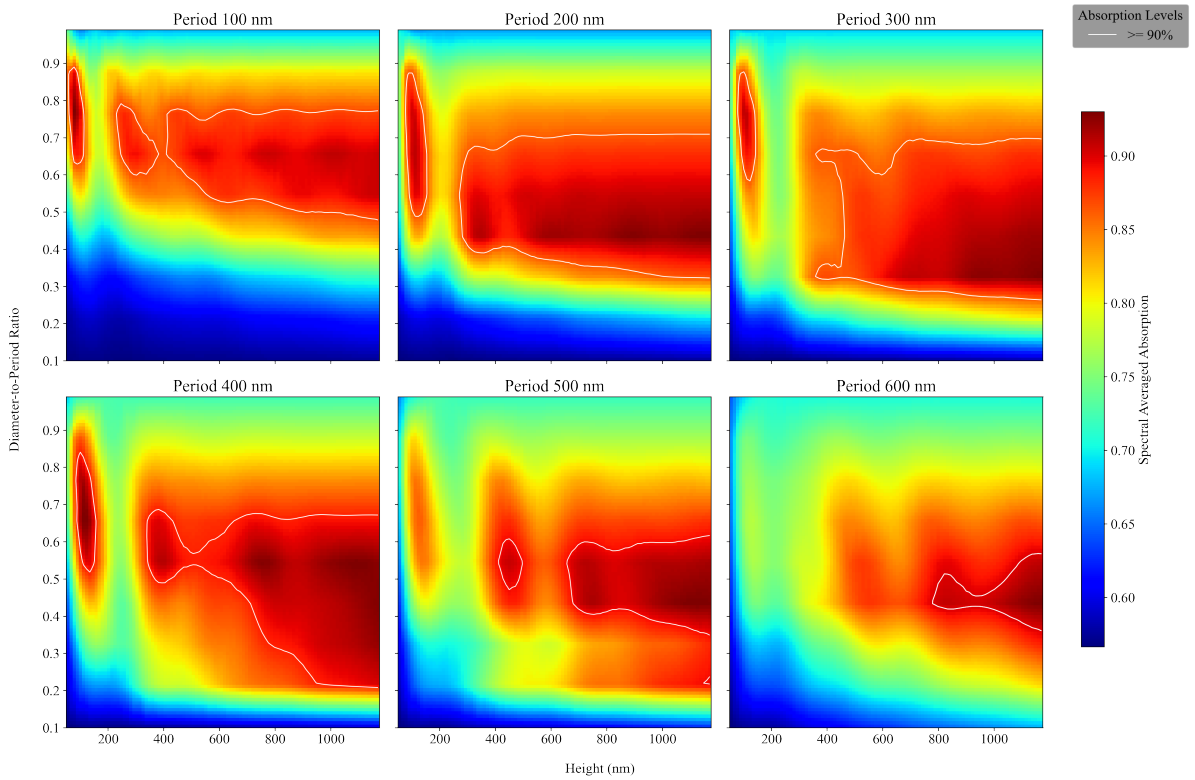

Figure 1.4: Spectrum-averaged Absorption vs. Pillar Density and Height. Enhanced absorption correlates with increased height and close-packed density, attenuating at extreme densities [3,4]. Undulations between 100-200 nm heights indicate effective medium behavior [3].

One can observe that generally increasing the pillar height results in higher absorption [22]. Increasing the pillar height allows for more modes to exist, thus allowing for more absorption to happen in the material. This can be seen in the addition of further dips in the far field reflection plot. As for the diameter-to-period ratio, one can perceive that more absorption is exhibited for higher percentages, a result attributed to a smoother refractive index gradient [23]. Naturally, this trend drops again at very high ratios since the density is getting so dense that the film begins to resemble the bulk material again. Furthermore, one can observe undulations in the absorption as the pillar height increases. This is especially prominent between 100 nm and 200 nm pillar height. Such behavior is attributed to the array functioning as an effective medium, closely approximating the characteristics of a single-layer thin film. The observed maxima and minima in reflectance are a consequence of the interference between reflections originating fromthe top and bottom surfaces of the layer as the height of the pillar is increased [22]. The thin white line in Figure 1.4 denotes the geometric conditions of the nanopillar array that result in a spectral averaged absorption of at least 90% or more. These are geometries that are potentially interesting as pixel designs. The influence of the gap width on the contrast ratio is intricate. Figure 1.5 showcases the relationship between the contrast ratio and gap width for various diameter-to-period ratios, exemplified for a period of 400 nm, a pillar height of 200 nm and an actuated state of 100 nm membrane displacement.

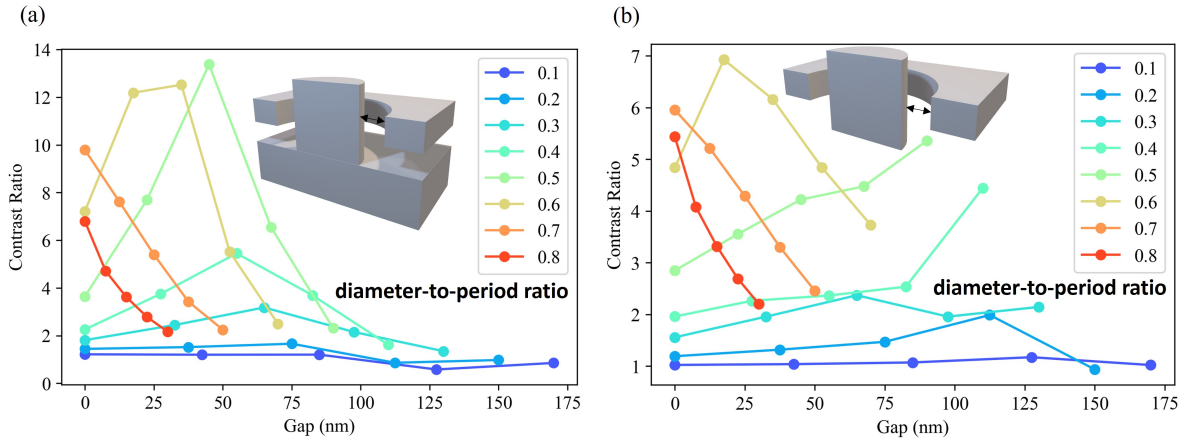

Figure 1.5: Influence of the gap on the contrast ratio. (a) Contrast ratio versus gap width for different diameter-to-period ratios, with an aSi substrate. (b) Contrast ratio versus gap width for different pillar-to-period ratios, with an air substrate. Geometry: period of 400 nm, pillar diameter of 260 nm, and membrane displacement of 100 nm for the actuated state.

Figure 1.5a and b distinguish the effects of an aSi substrate from an air substrate. As perceivable by the difference in plotted curves, having a gap makes the optical characteristics of the device more susceptible to the substrate. Furthermore, the contrast ratio, which is defined as the average reflection in the idle state divided by the average reflection in the actuated state, tends to decline for gaps wider than 50 nm. However, this relationship also varies with the diameter-to-period ratio. Median ratios initially experience an uptick in contrast ratio, which subsequently declines, while higher ratios see a steady decrease in contrast ratio as the gap widens.

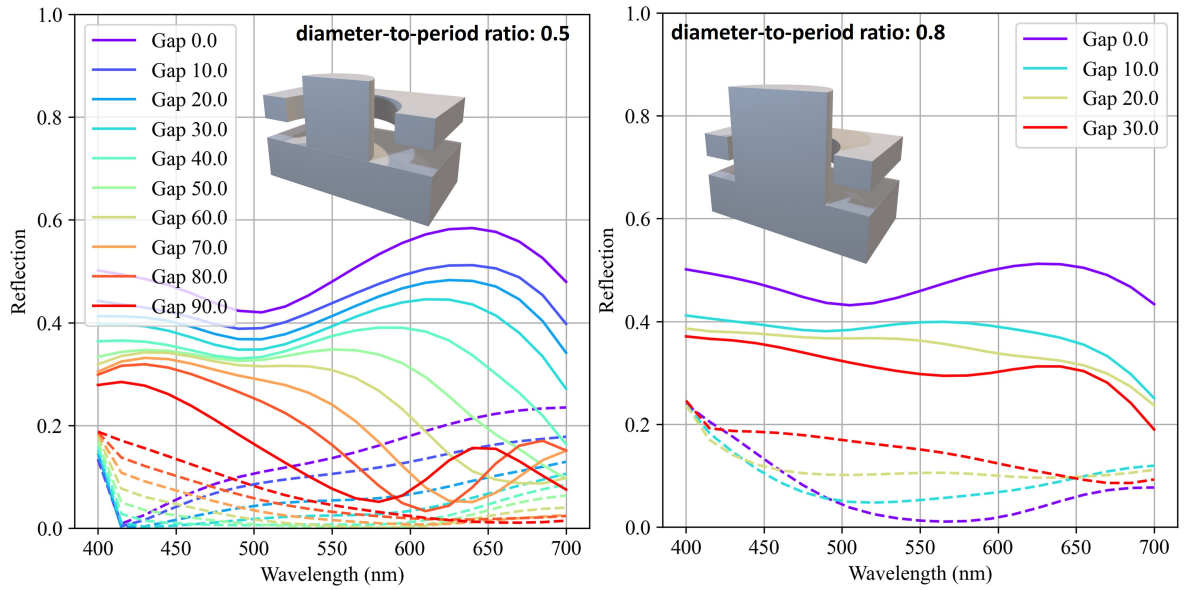

Figure 1.6: Influence of the gap on reflection spectra. (a) Pillar-to-period ratio of 0.5. (b) Pillar-to-period ratio of 0.8. Straight line: device in idle state; Dotted line: Membrane displaced by 100 nm downward; Period: 400 nm; Pillar height: 200 nm

The uptick at around 25-50 nm gap for medium ratios can qualitatively be explained by an increased absorption in the actuated state. It is hypothesized that the additional corrugation of the surface added by the gap leads to enhanced light trapping. While a certain gap width can lead to increased absorption in the actuated state, in the idle state the gap leads to reduced reflection. As will be outlined in chapter 2 for decent paper-like reflective display performances high white state reflectivity is also very important next to a good contrast ratio. Thus, in most cases, it is advised to choose

the smallest possible gap and optimize the remaining parameters to gain an acceptable contrast ratio. In either way, introducing the gap increases the complexity of the physics, and thus in this thesis the optimal geometric parameters are deduced using computational gradient-free optimization combined with rigorous electromagnetic (EM) simulations. The primary objective of this thesis is to investigate the development and operational principles of a new MEMS tunable metasurface, with potential application in reflective display technologies. The research journey delineated in this document adheres to a conventional developmental process. Chapter 2 provides an exhaustive state-of-the-art analysis, concluding that MEMS-based reflective display pixel units show promising capabilities in terms of power consumption, switching speed, contrast ratio, and reflectivity. Following this groundwork, Chapter 3 elaborates on the optical design methodology employed, and discusses, in particular, the Python framework built to facilitate the latter. Chapter 4 inaugurates the experimental phase of the research by detailing the construction of an initial static prototype. This basic model serves to validate the core hypothesis that a nanostructured surface can be engineered to achieve a dark optical state, while a flat surface configuration is employed for a brighter state. Subsequent to this validation, Chapter 5 advances the study by focusing on the fabrication of a more sophisticated prototype capable of dynamic state-switching. This crucial step substantiates the functional viability of the MEMS components integrated into the metasurface architecture. Chapter 6 concludes the research by outlining a process flow that enables the scaled fabrication of large arrays of units, a critical consideration for their potential deployment in pixelated reflective displays. Finally, Chapter 7 summarizes the key aspects and points towards future prospective avenues to further improve the design and manufacturing.

2

State of the Art

Disclaimer: Major parts of the state of the art have been adapted from a recently submitted review paper on reflective displays to the Journal of Optical Microsystems (JOM) under the title "Emulating Paper: A Review of Reflective Display Technologies". The JOM tracking number is 23034V.

Authors List: Dorian Herle, Olivier J.F. Martin, L. Guillermo Villanueva, Niels Quack

Doctoral candidate's contribution: The doctoral candidate performed the literature search, data collection, validation, analysis, summarization, and complete redaction of the paper.

2.1. Print Media as Benchmark for Reflective Displays

A commonly employed benchmark for assessing the static performance of reflective displays is the extent to which they can emulate the visual characteristics of traditional print media. These characteristics include elements such as ambient contrast ratio, white state reflectivity, color, and bistability. While these benchmarks serve to gauge the performance of reflective displays, they also align with foundational measurement parameters highlighted in the broader context of display technologies[24]. By focusing on these four key characteristics, this chapter aims to offer a comprehensive understanding of how reflective displays measure up to print media in terms of readability and visual comfort.

2.1.1. Ambient Contrast Ratio

White paper can be described as a close approximation of a perfectly diffuse, or Lambertian, surface [25], making it appear bright from any viewing angle. At the same time, black pigments will absorb most of the light. The ratio between the brightest and darkest state is commonly referred to as "contrast" or contrast ratio (CR). Although emissive displays frequently exhibit exceedingly high contrast ratios, it is important to note that these values are typically attained under dark environmental conditions. Under bright ambient conditions these values usually greatly deteriorate for emissive displays, as can be seen in Figure 2.1.

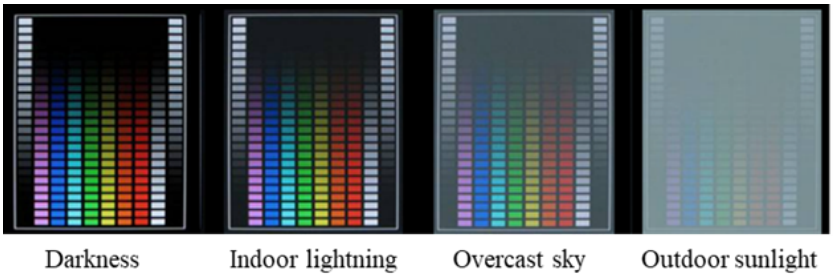

Figure 2.1: Qualitative photographs of a representative emissive display under different ambient conditions. Photographs are taken in darkness (0 lux), indoor lighting (1k lux), overcast sky (5k lux), and outdoor sunlight (40k lux). Adapted with permission from Ref. [26]. Copyright (2021) DisplayMate Technologies.

The ambient contrast ratio (ACR), as defined in Eq. 2.1, offers a more accurate approach for evaluating display performance, particularly for reflective displays, as it takes into consideration the real-world lighting conditions in which these devices operate [27].

$$ACR = \frac{L_{\text{on}} + L_{\text{Ambient}} R_L}{L_{\text{off}} + L_{\text{Ambient}} R_L}, \tag{2.1}$$

where L_{on} and L_{off} are the display's 'on' and 'off' luminance, L_{Ambient} is the ambient light, and R_L is the display's luminous reflectance [28]. The latter quantifies the amount of visible light reflected by a display panel under ambient lighting conditions, considering the human eye sensitivity V(λ) (i.e., CIE 2° Standard Observer), the spectrum of the incident ambient light S(λ) (i.e., CIE standard D65 light source), and the spectral reflectance of the display $R(\lambda)$. Mathematically, defined as follows:

$$R_L = \frac{\int_{\lambda_1}^{\lambda_2} V(\lambda) S(\lambda) R(\lambda) d\lambda}{\int_{\lambda_1}^{\lambda_2} V(\lambda) S(\lambda) d\lambda} \tag{2.2}$$

R_L serves as an index for evaluating the undesirable reflection of environmental light, which could compromise the legibility and visual comfort of the display interface. Using Eq. 2.1, an average R_L of 4%, and a typical portable display luminance of 1500 lux, the ambient contrast ratio drops to below 2 in direct sunlight (40 K lux), which renders the screen illegible. Table 2.1 describes human readability within terms of ACR.

Table 2.1: Ambient Contrast Ratio and Readability.

Ambient Contrast Ratio	Readability
1-2	Illegible under direct sunlight
3-4	Sufficient readability in shade; marginal legibility under direct sunlight
5-9	Adequate readability in sunlight; satisfactory appearance
10	Highly legible in sunlight; visually appealing
15	Exceptional readability; aesthetically pleasing
20	Superior performance; outstanding readability

2.1.2. White State Reflectivity

Next to ACR, white state reflectivity is important to mimic the appearance of paper. Figure 2.2 compares the black and white reflectance of three different media: high-quality glossy print, standard print, and LCDs, respectively. As can be seen, glossy prints have a white state reflectivity of around 80%, which sets them apart from the average 30% reflectivity found in reflective LCDs.

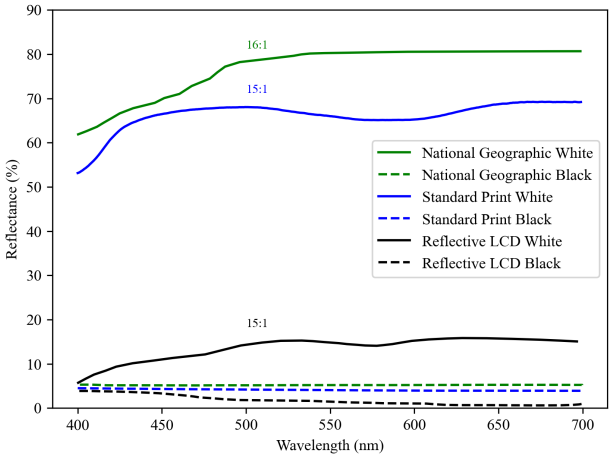

Figure 2.2: Reflectance spectra for white and black states of a high-quality magazine print (National Geographic), standard print, as well as a reflective LCD. Contrast ratios are indicated on top of the white reflectance lines. Data for Reflective LCD and national geographic sourced from [29] .

2.1.3. Color

Color reflective displays pose another layer of difficulty in obtaining bright vivid colors. Much of it boils down to the right color system choice. Emissive displays predominantly employ an RGB (red-green-blue) system or an augmented RGBW (red-green-blue-white) system. In the context of reflective displays, using an RGB system leads to a maximum white-state reflectance of 33%, as each subpixel in an RGB configuration only contributes 33% of the light. Similarly, an RGBW system can achieve a maximum white-state reflectance of 50% due to the added white subpixel, which further contributes to the overall reflectance. These values assume fully saturated color filters and are usually lower in practice.

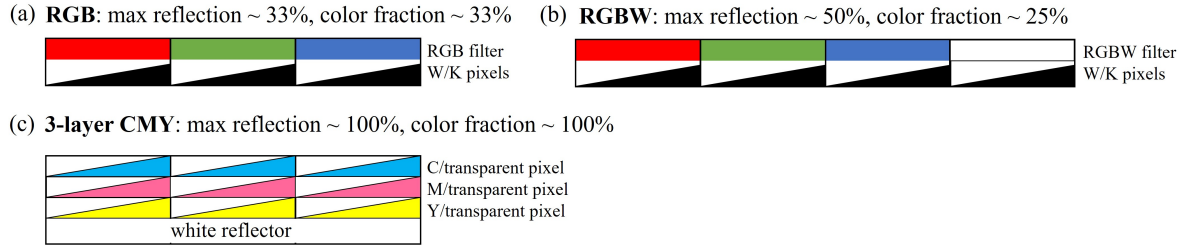

Figure 2.3: Schematic representation of different color systems. (a) Red-Green-Blue (RGB) color filters on top of white-black switching pixels, result in a maximum reflection of 33% and a color fraction (the effective area over which saturated color can be displayed) of also 33%, (b) Red-Green-Blue-White (RGBW) color filters add a white filter, increasing maximum reflection to 50%, however at the cost of a reduced color fraction of 25%, (c) 3-layer Cyan-Magenta-Yellow pixels with a white reflector yield an exceptional maximum reflection and a color fraction of 100%. This configuration is mostly used in print media. Adapted with permission from Ref. [30]. Copyright (2011) Society for Information Display

Subtractive color systems such as CMY (cyan-magenta-yellow) or CMYK (cyan-magenta-yellow-black) have traditionally been used in the printing industry, and usually employ a stacked architecture that greatly enhances light conversion. An optimal white state and maximum color fraction, defined as the effective area over which saturated color can be displayed[30], can be realized through the incorporation of a tri-layered structure featuring CMY (cyan-magenta-yellow) switching layers in the display system [31],[32]. At the same time, stacked displays increase costs and complexity because they require more materials, additional backplanes, and complex driving electronics. In addition, pixel resolution must be limited to maintain enough clear aperture, which helps reduce optical losses and parallax problems. To avoid significant parallax issues, the distance between the front

and rear pixels in a multi-layer stack should not be larger than the pixel size itself. This becomes challenging when dealing with very high-resolution displays. It is clear that subpixels capable of switching not only between more than two color states, offer the potential to develop single-layered display systems capable of achieving 100% color reproduction[30].

2.1.4. Bistability

Once printed on paper, no further energy is required to see the image or text. Ideally, this should be mimicked in reflective display technology. Bistability, a desirable feature for display devices, refers to the ability to maintain image persistence in two stable states without requiring continuous energy. This means that once the image or text is printed, it can be seen without the need for additional energy.

2.2. Reflective Display Technologies

Reflective display technologies have been evolving since the 1970s, with the introduction of "Gyricon" at Xerox's Palo Alto Research Center[33]. Over the years, numerous e-paper technologies have been developed and can be broadly classified based on their tunability mechanisms. These categories are shown in Figure 2.5, and encompass electrophoretic, liquid crystals, MEMS, electrowetting, phase change, and electrochromic, as well as tunable photonic crystals.

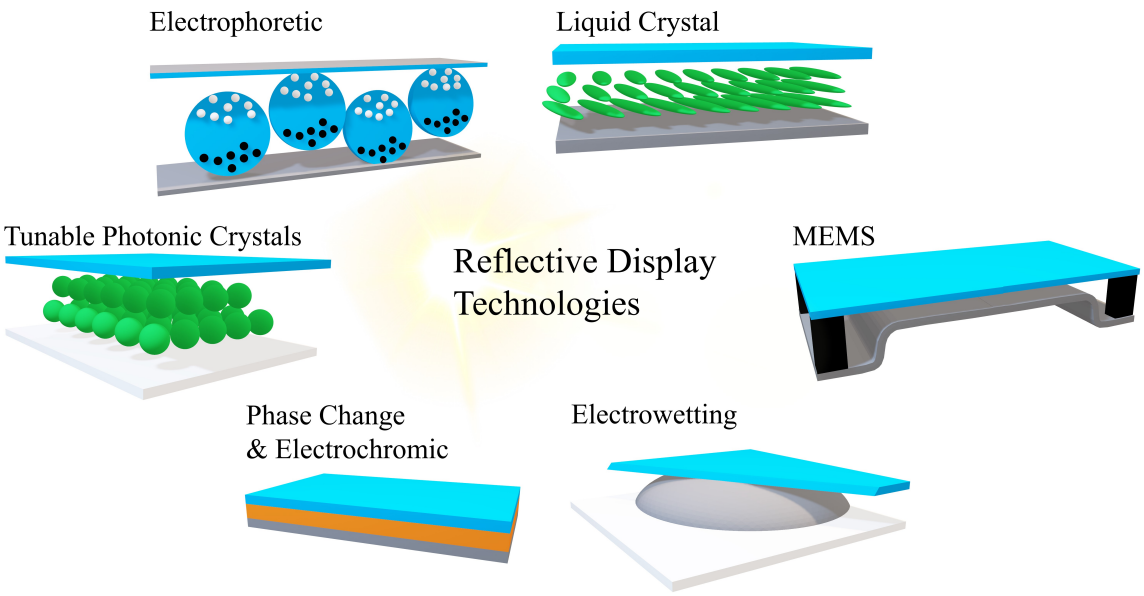

Figure 2.4: chematic visualization of the discussed reflective display technologies. Light manipulation principles across these display technologies: LCDs - polarization; MEMS (IMod) - interference; Electrowetting and Electrophoretic - absorptive media transport; Phase-Change - refractive index; Electrochromic - band-gap adjustment; Photonic Crystals - diffraction.

In the following sections, we will delve into each actuation mechanism, discussing the fundamental principles, implementations, and possible outlooks. By examining these technologies in detail, we aim to provide a comprehensive understanding of the diverse e-paper landscape and its ongoing developments.

2.3. Electrophoretic

Electrophoresis describes the motion of charged particles relative to a fluid under the influence of an external electric field. While the beginning of electrophoretic displays can be attributed to the printing company Xerox, who was granted a patent on "Color Display Device" in 1971 [34], it was the introduction of microencapsulation of the charged particles by Comiskey et al. [35] from MIT that allowed this technology to mature to commercial readiness, resulting in the creation of the commercial entity EInk. Despite its progress, the lack of video compatibility in electrophoretic displays is a significant challenge for widespread adoption in mobile devices. This limitation triggered the exploration of innovative solutions, one of which has been the employment of total internal reflection (TIR) modulation, allowing for a much-reduced particle traveling distance. The electrophoretic TIR display has been commercialized by the company "CLEARink Displays, Inc." short for "Charged Liquid Electro-Active Response". CLEARink Displays emerged as a separate entity from the University of British Columbia in 2012 [36]. Both technologies are presented in the following sections.

2.3.1. Working principle

In general, an electrophoretic display operates by displacing charged pigments in and out of sight using electrostatic fields. Equation 2.3 describes the particle velocity (with initial condition $v_0 = 0$). The formula can be derived by equating the electric attraction forces acting on a charged particle due to an external electric field with the fluidic drag forces counteracting the particle mobility, which are given by Stoke's law[37].

$$v = \frac{qE}{6\pi\mu d}\left(1 - e^{-\frac{6\pi\mu d}{m}t}\right) \tag{2.3}$$

where v is the particle velocity, E the applied electric field, q_P the particle charge, μ the fluid's viscosity, d the particle's diameter, m the mass of the particle.
As can be observed from Eq. 2.3, the particle velocity, and thus the speed at which a single pixel can switch state, is influenced by several factors. One of the key determinants is the particle charge. It is most often deduced from the Zeta potential, which is a measure of the electrostatic potential difference between the fluid and the outer layer of the electrical double layer surrounding the particle. This parameter provides a nuanced measure of the particle's effective charge and its interactions with the fluid. For low-dielectric media, it is proportional to the particle charge [38]. A high absolute value of the Zeta potential ensures better dispersion of the particles, reducing aggregation and enhancing the display's long-term reliability. Separately, it's important to note the limitations imposed by the applied electric field. Research efforts have been focused on reducing the required traveling distance, reducing the electrode spacing, and improving the chemical properties of the system.

2.3.2. Implementations

Microcapsule electrophoretic displays utilize electric fields to move highly scattering or absorbing microparticles vertically within a microcapsule. A multitude of those microcapsules forms one pixel and monochrome or color systems can be developed.

Monochrome system

To this date, vertical dual-particle electrophoretic-based displays have been the most commercially successful reflective display technology on the market. As can be seen in Figure 5, depending on the applied electric field, different colored particles with either positive or negative zeta potential are selectively moved to the surface, creating the desired image or text.

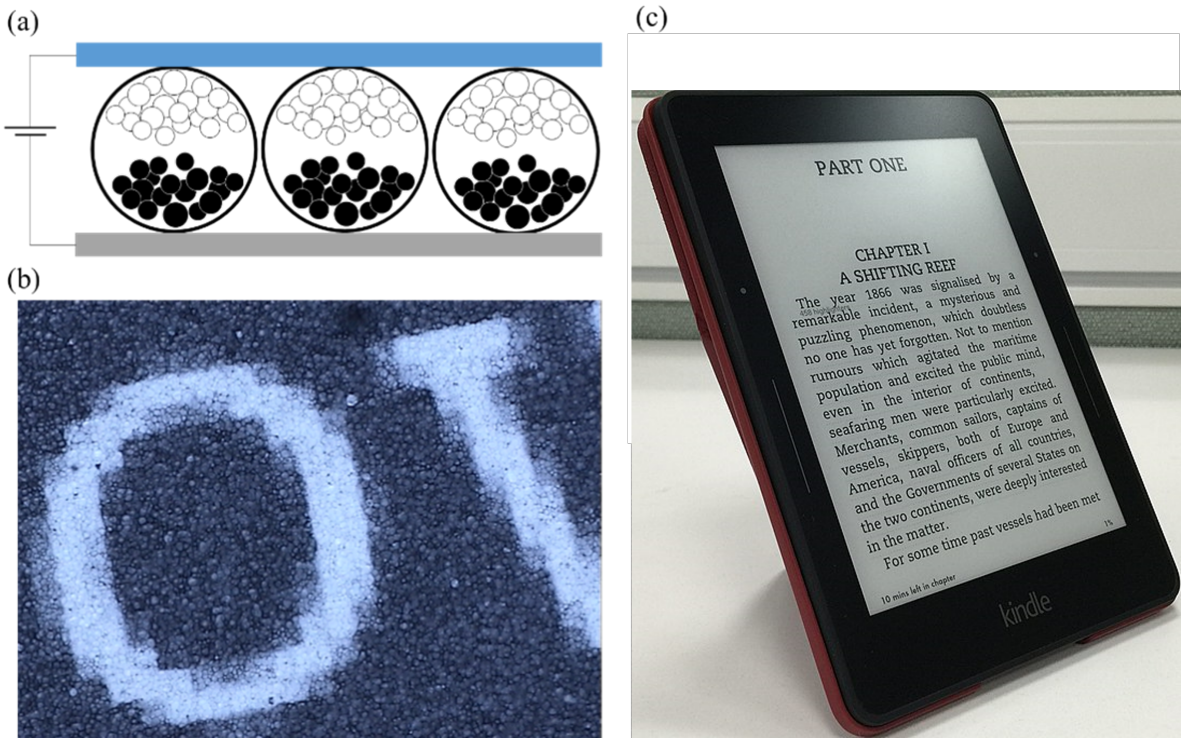

Figure 2.5: Microcapsule electrophoretic display. (a) Schematic representation of an electrophoretic microencapsulated black and white ink, wherein the displayed color is controlled by the polarization of the electric field and the resulting vertical position of the charged nano-pigments. (b) Microscope image of microcapsules in a working prototype. Image from Ref. [39], used under a Creative Commons Attribution 2.0 Generic (CC BY 2.0) license. (c) A photograph of the Amazon Kindle e-reader tablet adapted from Ref. [40], used under a Creative Commons Attribution 2.0 Generic (CC BY 2.0) license.

White particles often consist of inorganic pigments, such as TiO_2, ZrO_2, ZnO or $Al2O_3$, whereas black particles are often made from Color Index black pigments, iron oxide, or carbon black [41]. These particles are dispersed in a non-polar fluid, which helps reduce leakage currents within the display. Surfactants are added into the system to prevent particle agglomeration[42] and to aid particle charging [43]. To reduce switching voltage, a coating formulation[44] is deposited capsules in a monolayer, allowing for close and thinner packaging of the microcapsules. In addition, it is found that adding an oil-soluble high molecular weight polymer to the electrophoretic fluid increases image stability to 12 days, and, importantly, without increasing the fluid viscosity [45]. In the initial stage of electrophoretic display developments, a ”flash reset” was necessary prior to rendering a new image. This process involved resetting the positions of all particles to a uniform, known state, allowing for a more predictable and reliable transition to the desired grayscale level in the subsequent image. Using an algorithm[46] that stores the history of each pixel's switching for a certain amount of time allows addressing 16 levels of grayscale without flashing. Parasitic polarization in the microcapsule polymeric binding material leads to a dwell time dependence[47]: the impulse required to switch a pixel to a new optical state depends on the time that the pixel has spent in its previous optical states. This issue has been greatly researched and resolved through careful selection of the materials used[48], [49].

Color System

Color display for dual particle systems has been achieved through the addition of a color filter array (CFA) as visualized in Figure 6a or multi-particle systems, visualized in Figure 2.6b.

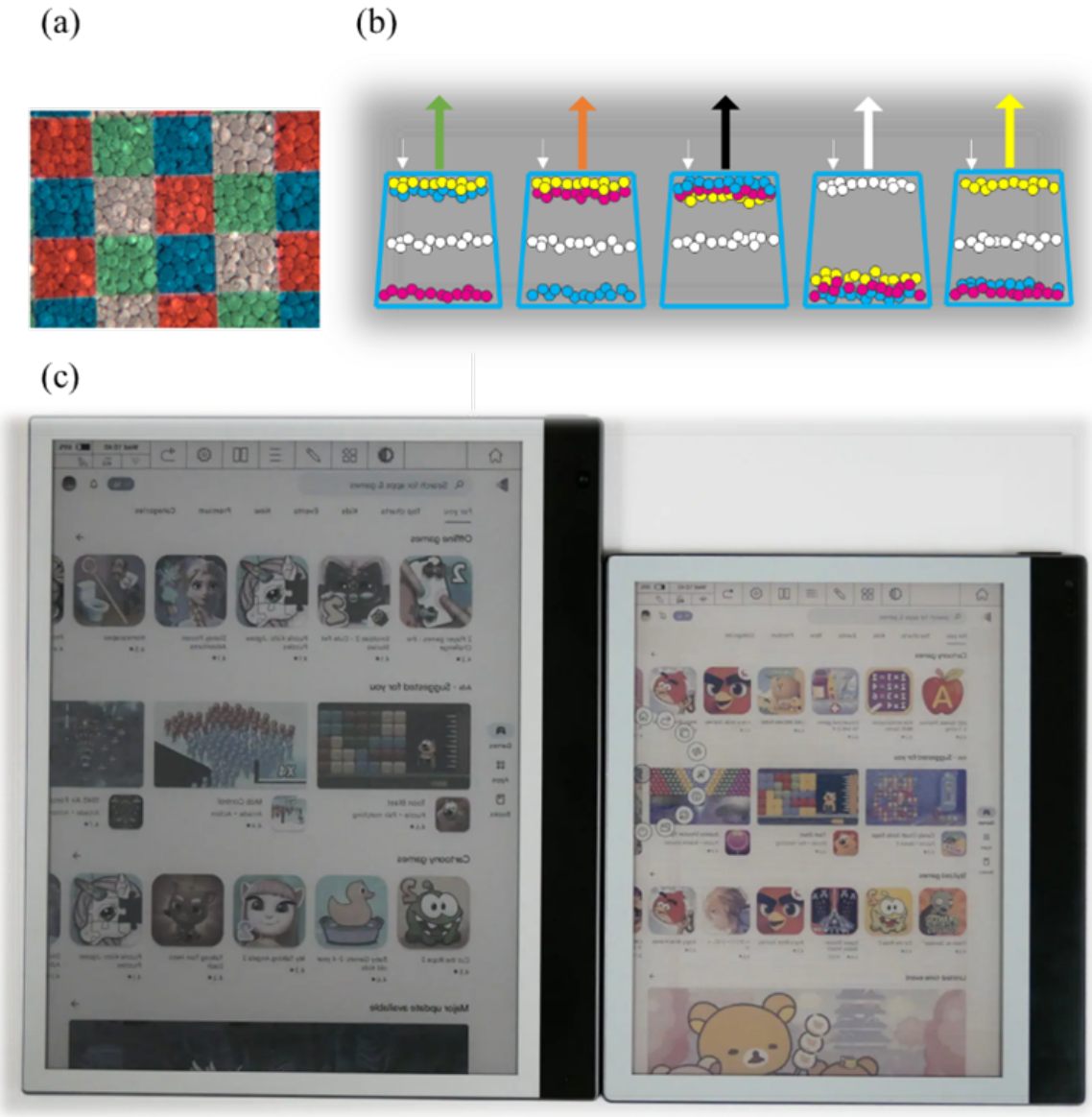

Figure 2.6: Color electrophoretic reflective display technology, based on (a) superimposed color-filter arrays. Image from Ref. [50] with permission. (b) A multi-color particle system. Image from Ref. [51] with permission. (c) CFA-based device "Inknote Color Plus on the left and "Bigme Galy" device on the right with a multi-particle system offering brighter colors [52]. The image is taken at the same location and same illumination, showcasing the increased brightness of multiparticle systems. Image Ref. [53]. Copyright (2023) Good e-reader.

Different methods have been explored to create CFA, such as direct printing[54] or photolithography[55] of a color resist, and laminated CFA films[56]. However, color filter arrays, such as RGB or RGBW, use area sharing, where each full-color pixel consists of three, respectively four sub-pixels. This method limits the display area for each color, leading to suboptimal brightness levels. Furthermore, the implementation of a color filter to divide monochromatic pixels into three colored pixels inevitably leads to a reduction in the overall resolution.
To overcome these limitations in filter-based color electrophoretic displays, current research is exploring multi-particle systems. The key concept behind multi-particle systems is to make use of different electrophoretic mobilities as well as charge polarity and intensity to separate the particles [57]. Using waveforms, these particles are pushed and pulled to mix colors and produce specific shades. The E Ink Spectra system uses black, white, and colored particles (either red or yellow). For full-color displays, EInk's Advanced Color ePaper (ACeP) combines white with cyan, magenta,

and yellow particles, enabling it to render up to 50,000 colors[51], akin to newspaper prints. Figure 6c compares two commercial displays using CFA (left) and a multi-particle system (right) under the same illumination condition. The brightness difference is clearly perceived.

2.3.3. Improving switching speed of microencapsulated electrophoretic display device

Various studies have been carried out to improve the response time. One approach is to use low viscosity[58] to increase electrophoretic mobility, however this deteriorates bistability. Other approaches focus on improving the driving waveforms[59], or on picture drawing algorithm based on the content[60]. Yet another suggestion is to use the inverse electrorheological (IER) effect[61], essentially reducing the viscosity briefly during the switching time. It was found that such an IER effect can be induced by the rotation of liquid crystal molecules[62], briefly leading to some carrying hydrodynamic motion. Adding LC molecules leads to a 2.8 times reduction in response time and at the same time cuts the applied voltage in half.

2.3.4. Total Internal Reflectance Electrophoretic Displays

TIR displays use total internal reflection for bright images and "frustrated" TIR for dark ones, achieving high contrast and fast visual changes. In TIR, light in one medium reflects internally when hitting a lower-index medium at a steep angle. Frustrated TIR happens when a third, higher-index medium is close to the interface, letting some light pass or be absorbed. This technology was first reported in 1997[63].

Working principle

For TIR electrophoretic displays, the switching mechanism is achieved through the movement of charged particles in and out of the evanescent field[64]. To optimize the angular response, TIR displays are constructed using hemispheres[65]. Charged electrophoretic absorbing particles are hosted inside a liquid below the reflective hemisphere array. As depicted in Fig. 2.9, absorbing particles are pulled out or into the evanescent field, allowing the light to be reflected or absorbed respectively.

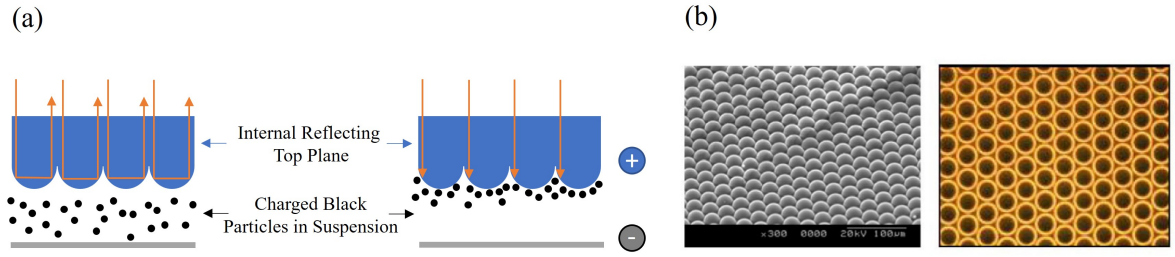

Figure 2.7: Total internal reflection (TIR) electrophoretic display concept. (a) Schematic representation[43] of the working principle, showing TIR reflection and frustrated TIR when the polarity of the applied electric field draws the absorptive charged black particles into the evanescence wave field. (b) SEM image (left) of a fabricated reflection plane consisting of spheres in an index matching layer, as well as an optical microscope image showing the reflection rings and dark areas of normal incident light. Image Ref. [66] with permission

The phenomenon of Total Internal Reflection (TIR) occurs when light is incident upon an interface from a high refractive index material n_1 to a low refractive index n_2 at an angle of incidence θ that exceeds the critical angle θ_c given by the Eq. 2.4.

$$\theta_c = \arcsin\left(\frac{n_2}{n_1}\right) \tag{2.4}$$

For angles of incidence less than the critical angle, light is transmitted through the interface. Conversely, for angles of incidence greater than the critical angle, the light undergoes TIR and is reflected back into the first medium. As depicted in Fig. 2.9, upon normal incidence light, these

hemispheres exhibit a bright reflective ring until the light's angle of incidence surpasses the critical angle, causing the hemisphere's center to reflect less light. It can be shown (see Appendix A.2) that for normal incidence, the reflection is given by Eq. 2.5.

$$R = 1 - \left(\frac{n_2}{n_1}\right)^2 \tag{2.5}$$

In practice, the said hemispheres are formed from high refractive index nano-composite material $(n_1 \sim 1.9)$ and low-index adjacent medium such as Fluroniated hydrocarbon $(n_2 \sim 1.2)$ normal incidence reflections on the order of $\sim 60\%$ can then be expected.
The size of the hemispheres can be made as small as $2\mu m$ in diameter. This reduces the device thickness and, thus the required travel distance for the absorbing nanoparticles, yielding higher switching time and reducing energy consumption, as well as easing the material constraints with respect to the material attenuation coefficient. Color displays are achieved by incorporating CFA on top of the microsphere array, as depicted in Fig. 2.8.

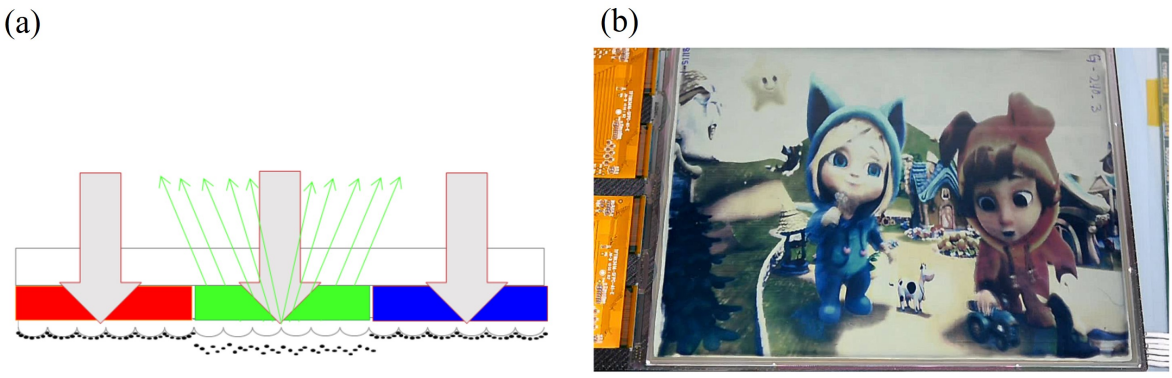

Figure 2.8: TIR electrophoretic color display. (a) Schematic of TIR display with an RGB color filter array; green is in a reflective state, whereas red and blue are in the absorptive state, (b) a picture of a tablet implementing this technology. Adapted with permission from Ref. [67].

CLEARink released a number of working prototypes, for example at SID 2019[67] a 9.7" diagonal eTIR display demonstrating video and color capabilities including grayscale (see Fig. 2.8b), showcasing a very small power consumption of merely 0.029 mJ/cm^2.

2.3.5. Outlook

The main challenge of microcapsule electrophoretic displays is the switching speed. The response time is usually as long as hundreds of milliseconds[68] . This limits the application to static or slow-moving images. Current challenges for TIR electrophoretic are mostly related to commercial scalability, as well as improving the color gamut, video speeds, reducing ghosting, and the general reliability of the device. A potential long-term issue for TIR-based reflective displays is that they cannot operate in transmission by design. Thus, this makes a stacked CMY(K) pixel design difficult and ultimately limits the potential for achieving high color saturation/brightness.

2.4. Liquid Crystal

Backlight liquid crystal displays make up most of commercially available emissive displays, and at the same time presented one of the first reflective display technologies. LCDs were first suggested for display applications in 1968 at the International Liquid Crystal Conference in Ohio. The prototype presented by George Heilmeier of RCA [69] generated substantial interest and triggered the start of LCD developments for many industrial companies. The next crucial step towards a robust, "television-ready" LCD was the invention of the Twisted Nematic display (TN-display) by Martin Schadt and Wolfgang Helfrich in 1970[70]. The TN principle and technologies derived from it remain one of the central foundations of most LCDs to this day. However, one of the challenges has been their continuous power consumption to maintain an image. This led to the exploration of

more power-efficient display technologies. A significant breakthrough came in 1994, when Yang et al.[71] demonstrated that by dispersing a polymer in cholesteric liquid crystals (ChLCD), or using a cell with inhomogeneous surface anchoring, resulting in long-term bistability. This bistable property enables the liquid crystal molecules to maintain their original orientation for a long time even after the electric field is removed, greatly reducing power consumption for static images. Both Twisted Nematic and Cholesteric LCD technologies are presented in the following sections.

2.4.1. Twisted-nematic Liquid Crystal Displays

Working Principle

The TN-cell[72] is the most basic LCD technology, consisting of a liquid crystal sandwiched between two crossed polarizers and a reflective layer on the backside. The first polarizer in this setup polarizes incoming light in one direction. When turned off, the liquid crystal rotates the polarization of the traversing light by 90°, allowing it to pass through the second polarizer and be reflected on the backside mirror. When the liquid crystal is turned on, the incoming light's polarization is no longer rotated and is blocked on the second polarizer (see Figure 9a).

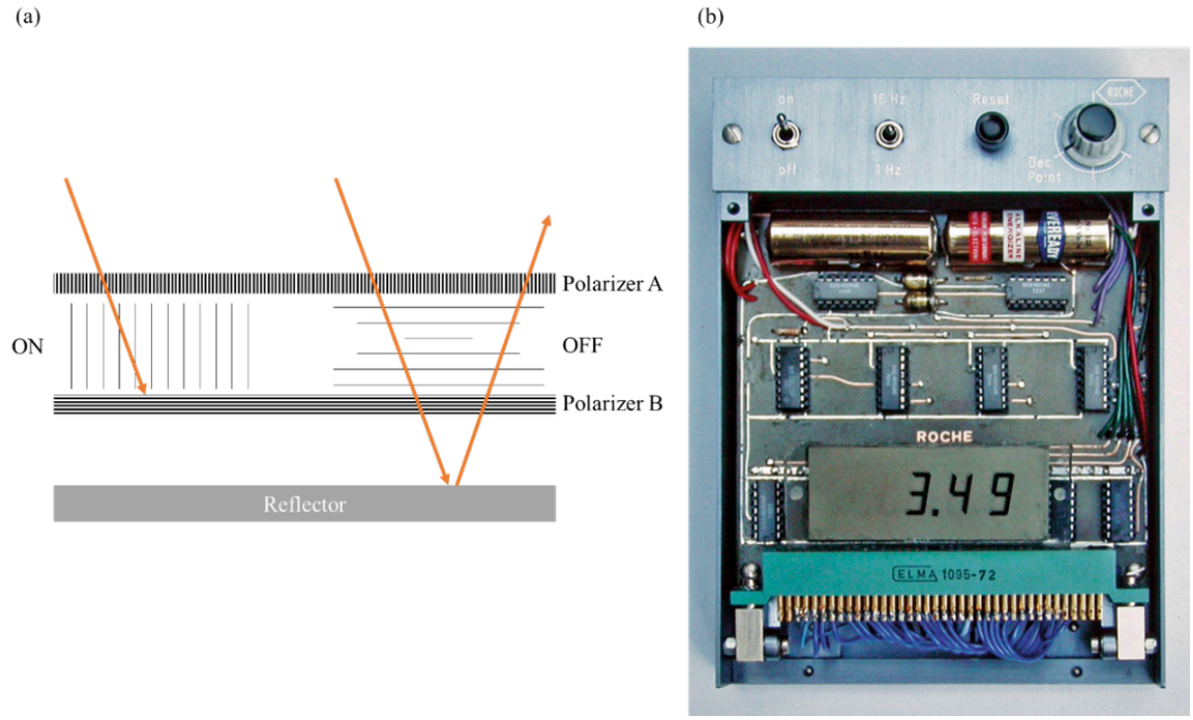

Figure 2.9: Reflective TN display: (a) Schematic representation: Unpolarized light first passes through Polarizer A, where it is linearly polarized. In the OFF state, the liquid crystal rotates this polarization by 90 degrees, enabling it to pass through Polarizer B and reflect off the back-reflector. In the ON-state, polarization isn't rotated, hence it's blocked by Polarizer B.(b) Early twisted nematic LCD prototype 1972. Adapted with permission from Ref. [73]. Copyright (2018) Springer Science and Business Media LLC

Polarizer-based liquid crystal technology can attain a maximum reflectivity of 50% since a polarizer filters out half of the unpolarized ambient light.

Implementation

TN-cell-based reflective LCD is not bistable by nature. Memory-in-pixel (MIP) technology is often employed to reduce power consumption[74]. MIP designates the technology of integrating static random-access memory (SRAM) circuits into every pixel unit, effectively holding the voltage until a pixel state needs to change. To further reduce energy consumption, it is suggested to only refresh the rows and lines of the display that need to display movement [75]. As MIP LCDs are fully digital displays compared to conventional analog active-matrix LCDs, attaining grayscale values is more

challenging. In terms of optical characteristics, light diffusion methods must be included in a reflective LCD to avoid a mirror-like look. Such diffusion can either be achieved through the addition of scattering back electrodes or top diffuser films.

Outlook
TN-cell-based reflective LCD has an economic advantage over other technologies as they can directly leverage the decades of emissive LCD manufacturing. MIP displays allow the reduction of power consumption significantly, but they also limit the range of available colors and grayscale. This is due to the intrinsic limitations in the amount of memory at each pixel site (bit depth), which in turn determines the number of colors that can be displayed. Currently, 6-bit color memory-in-pixel panels, 3-bit and 1-bit black-and-white panels are usually commercially available, restricting these displays to a smaller color palette (max. 64 here) and fewer grayscale levels. Finally, white state reflectivity is still limited to within 7- 18% in commercial displays[76].

2.4.2. Cholesteric Liquid Crystal Displays

The terminology "cholesteric" was first introduced in the scientific community by Georges Friedel in 1922[77], recognizing the initial identification of this particular state of matter within cholesterol esters by Friedrich Reinitzer in 1888[78]. Subsequent to this initial discovery, instances of cholesteric liquid-crystalline states have been reported in a variety of substances that bear no inherent connection to cholesterol.

Working Principle
Cholesteric refers to a phase of the liquid crystal where the molecules are arranged in layers with a helical stacking pattern. For normal incidence the reflected wavelength is given by[79], [80]:

$$\lambda_0 = n_a p \cos(\theta) \tag{2.6}$$

where n_a is the average refractive index, p is the helical pitch, and θ is the angle between the helical axis and the direction of propagation.
As can be seen from Eq. 2.6, reflectivity is concentrated around a specific central wavelength. Consequently, wavelengths deviating from these central peaks contribute less to the total reflectivity, leading to an overall decrease. The bandwidth of the cholesteric reflection is given by:

$$\Delta\lambda = \Delta n p \tag{2.7}$$

where $\Delta\lambda$ is the birefringence of the liquid crystal and p is the pitch. The liquid crystal molecules have an inherent electric dipole moment. By applying an electric field, these molecules experience a torque, causing the liquid crystal molecules to align along the field direction. This alignment alters the pitch p, thus tuning the reflected wavelength λ_0. The key advantage of cholesteric liquid crystals display is their bistability, with two textures at zero electric field: the reflective planar and the non-reflective focal conic. Here, 'texture' refers to the macroscopic molecular arrangement, as shown in Fig. 2.10a.
Upon normal incidence, a cholesteric liquid crystal surface reflects the component of the light that is circularly polarized in the same handedness as the CLC, transmitting the other component, and thus cannot reflect more than 50% of unpolarized light[81]. At oblique incidence, the reflected or transmitted light becomes elliptically polarized.
The brightness can be significantly increased by using a stack of two cells with opposing helical twists. Each cell reflects light with a specific handedness of circular polarization. The first cell lets through the light of one handedness, which is then reflected by the second cell, enhancing the display's brightness. Defects in the cholesteric crystal structure lead to scattering and non-ideal reflection conditions. This can be improved using rubbed contact surfaces. "Rubbed" refers to surfaces that have been mechanically treated by rubbing them in a specific direction to align liquid crystal molecules. This rubbing process induces an alignment of the liquid crystal molecules along the direction of the rubbing, which helps to minimize defects in the cholesteric structure. As a result, this treatment has been shown to yield an increase in reflectivity up to 70%[82](see Fig. 2.10c).

Implementations

A single pixel (Fig. 2.10a) in a cholesteric reflective display is made up of a cross-section of multiple layers, each of which contributes distinct capabilities to the pixel's overall functioning. The topmost layer is a glass substrate that provides the pixel with physical structure and protection. Directly behind this is a layer of Indium Tin Oxide (ITO), which acts as a transparent, conductive layer, allowing electric fields to be applied across the pixel. The pixel's core layer is made of cholesteric liquid crystals. This layer's properties change in reaction to applied electric fields, allowing it to selectively reflect light with a specified circular polarization, or "handedness" and transition between various states, resulting in the display's brilliant and dark appearances.

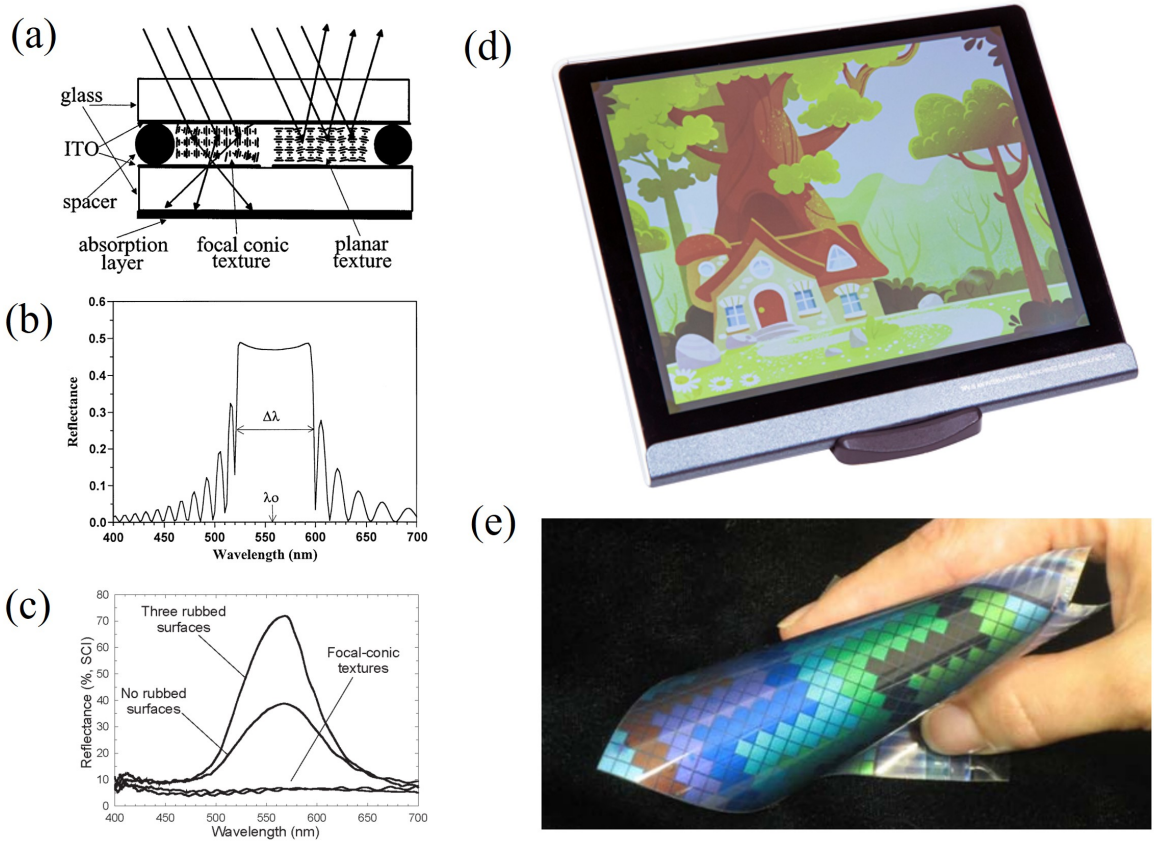

Figure 2.10: Bistable cholesteric reflective display design and examples. (a) The schematic design of a bistable cholesteric reflective display. Images from Ref. [83] with permission, illustrating the layered composition and functional elements. (b) exemplary reflection spectrum of said cell showing the reflection bandwidth $\Delta\lambda$ and central wavelength λ_0 [83], (c) 2-layer stacked cell with and without surface treatment (rubbing) to improve reflection. (d) 7.5-inch full-color ChLCD display, Image from Ref. [84]. Copyright (2023) AUO. (e) A flexible cholesteric display, demonstrating the technology's adaptability and potential for diverse applications. Image from Ref. [85] with permission.

A spacer separates the cholesteric liquid crystal layer from the bottom ITO layer. This spacer guarantees proper layer alignment and separation, which is crucial for preserving the liquid crystal's orientation and operation, since upon exerting shear stress on a cholesteric film, such as through substrate pressing, the system readily transitions back to the slightly more energetically stable planar texture[86]. The bottom ITO layer performs the same function as the top ITO layer, completing the pair of electrodes required to alter the state of the cholesteric liquid crystal layer. An absorption layer is often put directly beneath this, typically with black paint. When the liquid crystal is in the focused conic state, this layer absorbs forward diffracted and scattered light, improving the pixel's contrast and overall display performance. For display applications, the image needs to be temperature invariant. Since most cholesteric materials are temperature dependent[87], [88], much research has been dedicated to solving this issue, such as using dopants that show opposite changes in helical

twisting behavior with temperature to effectively cancel each other's influence[89]. Another important technological challenge is the peak wavelength on the incident angle, as can be seen from Eq.2.6. This dependence can be eased by integrating a diffuser film[90], and thus broaden the distribution of reflection angles, albeit at the expense of peak reflectivity. Recently, AU Optronics Corporation (AUO) has started to roll out reflective colorful ChLCD displays as shown in Fig. 2.10d. Figure 2.10e shows a flexible prototype by Kent Displays.

Outlook
Reflecting, and bistable cholesteric liquid crystal displays have been commercially accessible. These devices have evolved with features like increased luminosity, multi-color output via stacked layers, and high-contrast monochrome display from a single layer. Their current limitation is the switching speed which usually lies in the order of a second[91] limiting the potential applications in mobile devices.

2.5. Micro-Electro-Mechanical Systems (MEMS)

MEMS-based systems enable rapid, reversible, and often low-power geometric reconfiguration. These trademarks make them well-suited for reflective display technologies. Digital micro-mirror devices (DMD) have shown wide adoption in projection systems through the commercialization of micro-mirror arrays that pivot to modulate light [92]. Pixtronix's digital micro-shutter technology is an experimental emissive direct-view display that uses laterally translating shutters for light modulation [93]. By eliminating inefficient optical components, the Pixtronix MEMS-based shutters achieve over 50% optical transmission efficiency and reduced power consumption compared to LCDs. However, the technology has seen limited commercial adoption. However, MEMS-based direct view displays have not yet hit a wider market despite significant research efforts, most notably by Qualcomm with their "Mirasol" project, an interferometric modulators (IMod) display, originally introduced by Mark Miles in 1997[94]. Despite Mirasol not achieving the expected commercial success, MEMS-based direct-view displays continue to intrigue.

2.5.1. Interferometric Modulator Display (IMod)

Each sub-pixel of an IMod consists of a Fabry-Perot etalon composed of a movable metallic mirror and a semitransparent glass upper layer (see Fig. 2.11a). When light falls on the glass, it is split into two beams, with one beam reflected on the glass and one on the metallic surface. The traveled distance difference between the two beams results in a phase shift that affects the interference pattern of the reflected light. Tuning the gap between the glass and metallic layer changes the phase shift, and thus the wavelength at which constructive interference occurs. This sets the perceived color of the individual sub-pixels.

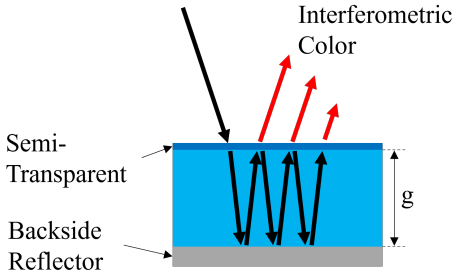

Figure 2.11: Schematic drawing of the interferometric modulator (IMod) concept. Incoming light strikes a semi-transparent layer, where it is partially reflected and partially transmitted into a resonant cavity. Within this cavity, the light undergoes multiple reflections between the layers. Outgoing light of a specific wavelength then constructively interferes with the incoming light, leading to the color perception of that element. This process allows for precise control over the displayed color by tuning the gap g between the layers

For the most simplistic IMod, which consists of a single layer with a reflective backplane, the gap (g) to enhance a specific wavelength λ is given by Eq. 2.8.

$$g = m\frac{\lambda}{\cos(\theta)2n} \tag{2.8}$$

where m is an integer $(1, 2, 3, \ldots)$ and n is the refractive index of the medium between the layers, and θ is the angle of incidence. For normal incidence $\theta = 0$ and considering air n $= 1$ as a medium, Eq. 2.8 simplifies to:

$$g = m\frac{\lambda}{2} \tag{2.9}$$

To create black, the gap g is reduced such that the reflected wavelength maxima is moved outside the visible spectrum and absorbed within a thin film within the stack. This is accomplished through electrostatic actuation, essentially collapsing the metal membrane onto the thin film stack. To avoid failure due to stiction in the collapsed state, stiction bumps are introduced[95]. In real devices, multiple layers might be used, in such cases, it is advised to refer to the transfer matrix method to compute the reflected color.

Implementations

Figure 2.12 shows the concept and full-scale realized tablet prototype of a Mirasol Qualcomm display. Each pixel can switch between a reflective colored state and an absorptive black state, where the initial gap of the subpixel cavity controls the reflected wavelength.

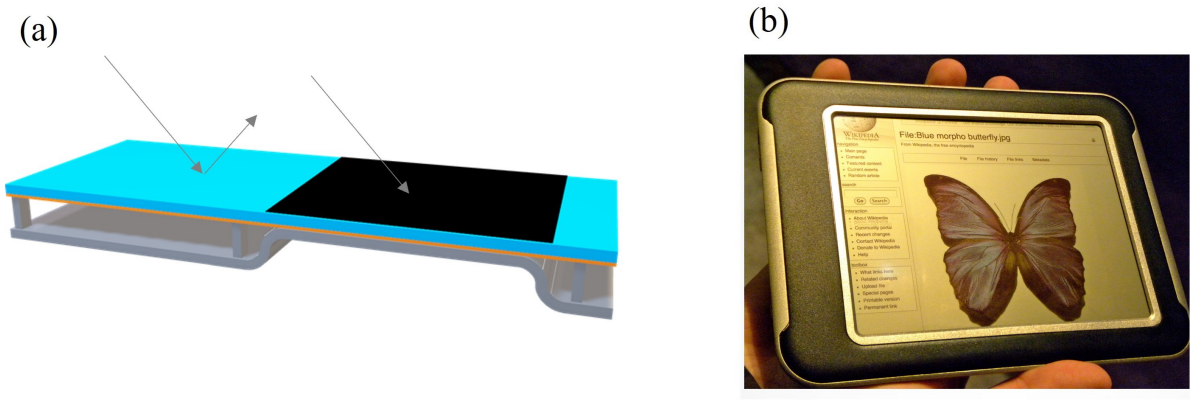

Figure 2.12: The IMod architecture and full-sized display prototype. (a) Schematic drawing of a pixel element showing the on (color) and off (state) [96]; (b) Picture of a prototype tablet utilizing the Qualcomm Mirasol. Image from Ref. [97], used under a Creative Commons Attribution-NonCommercial-NoDerivs 2.0 Generic (CC BY-NC-ND 2.0) license.

As can be deduced from Eq. 2.8, interferometric modulators possess by design an inherent property of incident-angle sensitivity, resulting in observable variations in perceived colors dependent upon the angle of incidence. Figure 2.13 shows a Mirasol display at different angles of incidence. One can clearly perceive the color shift in Fig. 2.13a, when observing from 10 degrees or 40 degrees. To mitigate this issue, a diffuser can be introduced on top of the IMod pixel array[98], as depicted in Fig. 2.13c.

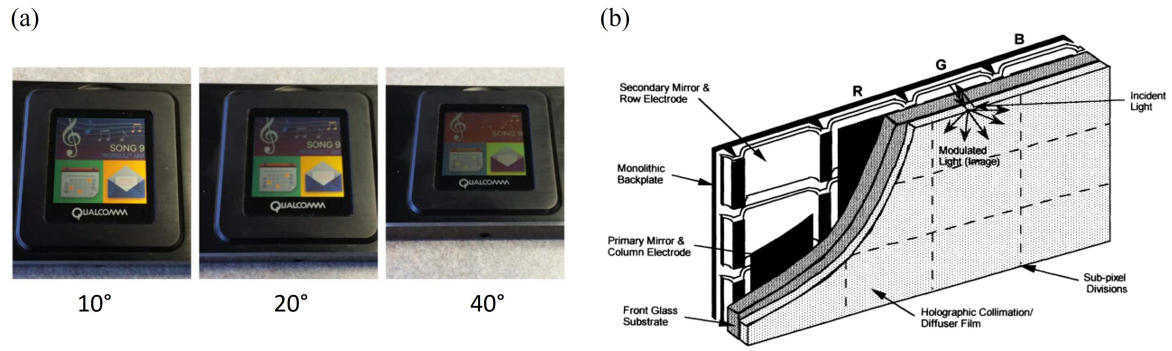

Figure 2.13: Off-axis viewing examples: (a) camera directed at 10° off surface normal, 20°, and 40°. Image from Ref. [99]. Copyright (215) Optica. (b) Schematic view of a Qualcomm Mirasol display unit, including, in particular, a front-facing diffuser film to reduce angle dependence. With permission from from Ref. [100]. Copyright (1999) Society of Photo-Optical Instrumentation Engineers (SPIE).

As mentioned in the previous section, the initial height of the IMod sub-pixel defines the reflected wavelength. However, as in all reflective display technologies, the use of a horizontal RGB will lead to suboptimal contrast due to area sharing, which reduces the white state reflectivity. Thus, an innovative single-mirror continuously tunable pixel design was also proposed, that uses interferometric absorption[101], instead of reflection. In this case, color regulation is achieved using interferometric absorption (see Fig. 2.14a). Incoming light, interfering with reflected light, produces standing waves with varying peaks and nulls based on the light spectrum. By strategically placing a thin absorber at a null for a specific wavelength, selective non-absorption allows reflection of that spectral component. All other wavelengths are absorbed, resulting in a saturated color reflection. Figure 2.14 displays the reflected color as a function of the absorber-mirror gap. In practice, the mirror is mobile, while the absorber is fixed on the substrate. This essentially allows each pixel to be modulated over the entire visible spectrum as can be seen in the zoomed-in picture of Fig. 2.14, drastically increasing the reflectivity.

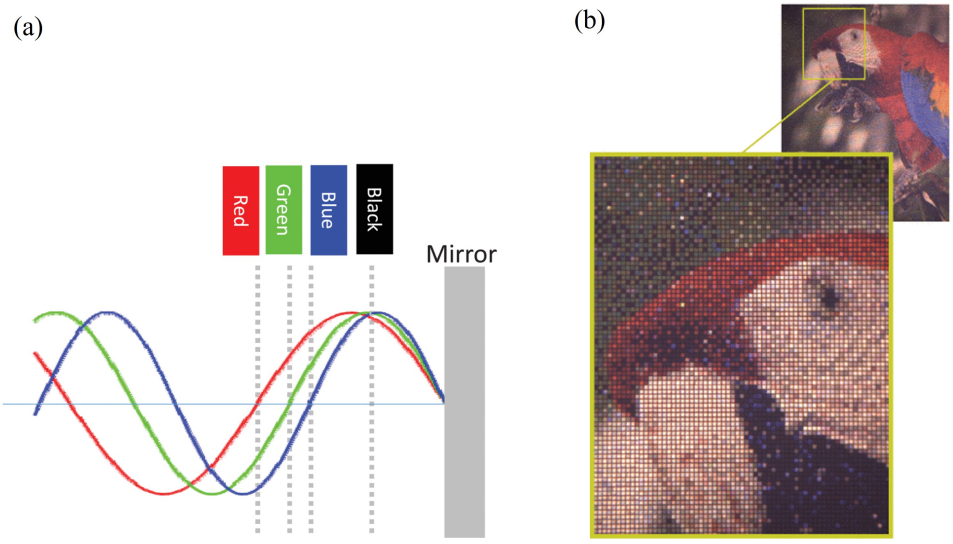

Figure 2.14: Interferometric absorption-based continuous color tuning: (a) Schematic illustrating the principle of color regulation through strategic placement of absorbers in standing light waves; (b) Implementation in a device, with an inset showcasing the capability to modulate individual pixels across the entire visible spectrum, enhancing reflectivity. With permission from Ref. [101]. Copyright (2017) Journal of Microelectromechanical Systems.

In recent years a graphene membrane-based interferometric modulator (GIMOD) was proposed[102], potentially allowing for refresh speeds of up to 400 Hz and 5 um pixel resolution, which translates

roughly into a smartphone with a 12K display resolution, which would be a 20 times increase in resolution compared to typical phone resolution (QHD, 2560x1440 pixels). Current designs of GIMOD are fabricated using graphene-covered micro-holes, essentially creating a voltage-controlled graphene micro-drum, where the initial cavity and the subsequent deflection of the drum control the reflected wavelength. This allows analog control over the pixel's color, yielding continuous full-spectrum reflective-type pixels. Simulations show a contrast ratio of 1:3 utilizing 29 layers of graphene. For vibrant reflective displays, this number must be increased by at least 3 times. Nevertheless, the high frame rate, resolution, and full-spectrum pixel are promising avenues.

Outlook
MEMS-based IMod reflective displays have been developed[103] to fully functional prototypes with impressive optical characteristics, such as 80% white state reflectivity and contrast ratios reaching 1:30[99], as well as providing fast switching times of 120 Hz[101] allowing for full video playback. As with any movable structure in the microscale, hermetic sealing and packaging become very important for the longevity of the device. Gas-impermeability of graphene might ease the packaging constraints for GIMOD devices, however, their contrast ratio of 1:3 needs to be improved.

2.5.2. Other MEMS-based reflective display technologies

Hereafter, two further early-stage MEMS-based potential reflective display technologies are briefly introduced. Both approaches still need substantial developments to move from early-stage demonstrators to large-scale production.

Mechanical Light shutter
A mechanical light shutter functions by actively introducing an object into and out of the light's trajectory, casting a shadow on an absorptive or reflective layer[104]. Such implementations can be observed in F. Jutzi et al. work[105], [106]. Figure 2.15 demonstrates the utilization of micro-flaps to alternate between a reflective state (flaps raised, producing a white pixel) and an absorptive state (flaps lowered, resulting in a black pixel). To optimize the contrast ratio, the anchoring system of the flaps should take as little visible area as possible, thus a good balance between flap size and anchor needs to be found. Increasing the size of the flaps comes with drawbacks such as slower switching speeds, reduced pixel density, and potentially compromised reliability. Nevertheless, this design offers the possibility of excellent contrast ratios.

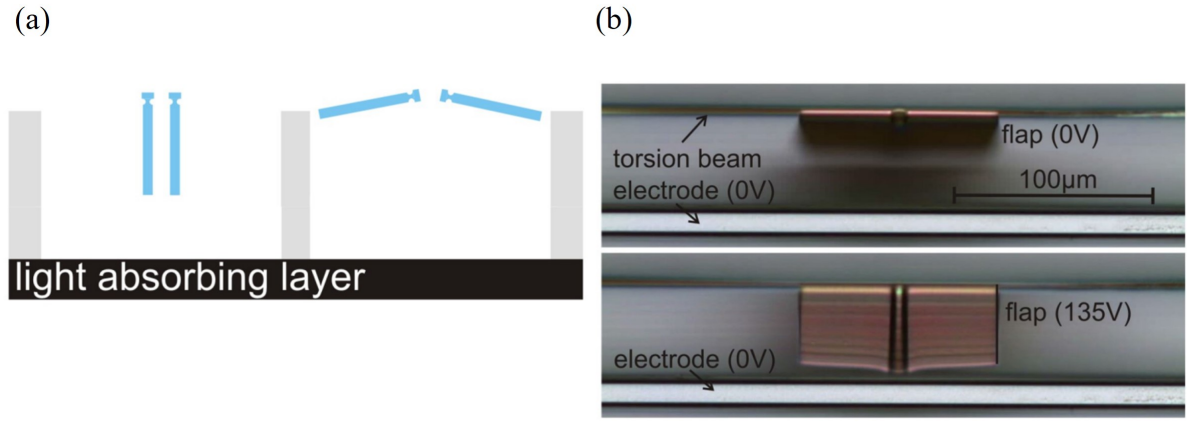

Figure 2.15: Micro-mechanical light shutter. (a) Schematic of the actuation method and (b) optical microscope image of the final prototype device[106]. The applied voltage was 135 V. Images with permission from Ref. [105]. Copyright (2010) SPIE Proceedings

2.6. Electrowetting

Electrowetting describes the act of applying an electric potential to modulate surface wettability. This phenomenon has found numerous applications in microfluidic devices[107] and varioptical lenses [108]. In 2002 Robert Hayes and Bokke Feenstra from Philips Research filed a patent[109]

and published[110] their results one year later, in which they demonstrated a video speed response time optical switch to be utilized in display systems, highlighting the potential of such systems. As with many reflective display innovations, the main motivation was to propose a video-capable solution. The key idea behind electrowetting-based reflective displays is colorant transport in and out of a light path by expanding and retracting colored liquids within a pixel unit. Similar to the Mirasol display, substantial research efforts by Philip's spinoff Liquidvista, later owned by Amazon and then Samsung, never fully substantiated into a commercial product.

2.6.1. Working Principle

The Young–Lippmann's equation[111] captures the electrowetting phenomenon in its most basic form. It describes how the contact angle of a conductive liquid changes in response to an applied voltage between a liquid and an isolated substrate.

$$\cos(\theta) = \cos(\theta_0) + \frac{CV^2}{2\gamma} \tag{2.10}$$

where θ is the contact angle after applying the voltage V, θ_0 is the initial contact angle, C is the capacitance between liquid and substrate, thus it depends on the insulation material $\left(\frac{\epsilon_0 \epsilon_r}{d}\right)$. Finally, γ is the interfacial tension.
In most electrowetting-based pixels, two fluids coexist. The first is usually an insulating oil ink. The second is a conductive transparent liquid electrolyte, such as DI water. At equilibrium, the colored oil film lays between a hydrophobic insulator coating of an electrode. With the application of potential, the stack becomes no longer energetically favorable, resulting in the water displacing the oil while reducing its contact angle from θ_0 to θ with respect to the hydrophobic layer, as can be seen in Fig. 2.16a. The colored oil film can essentially be opened and closed like a curtain.

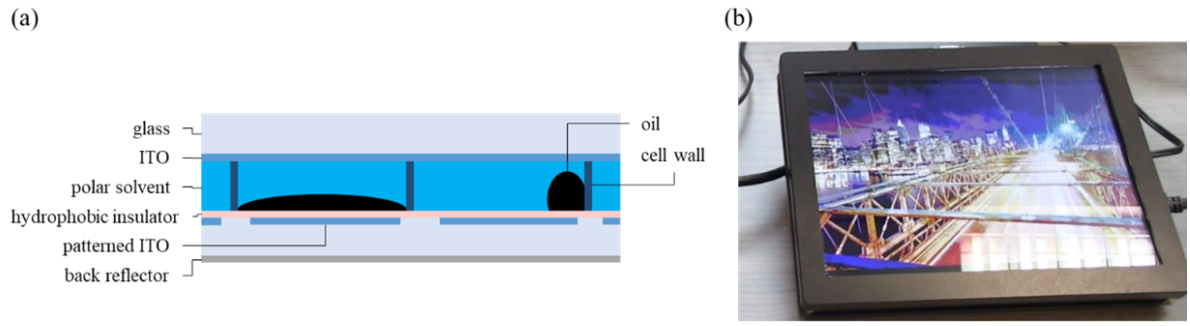

Figure 2.16: Electrowetting display mechanism: (a) Schematic of a unit pixel cell demonstrating the transition between expanded and contracted oil states, indicative of the 'curtain-like' movement of the colored oil film modulated by potential application; (b) Actual device implementation showcasing the technology in practice. Image from Ref. [112] Video The Electrowetting Display IEEE Spectrum YouTube channel.

The oil displacement happens in different stages[113], namely oil film rupture (initiation stage), oil-dewetting, and finally a slower oil drop rearrangement stage. A threshold voltage is needed for the initial oil rupture. Charges accumulate at the interface between oil and water when electricity is applied, creating pressure and causing the oil to undulate due to Rayleigh-Taylor instability[114]. As these undulations increase, the water ultimately breaks through to the dielectric substrate, resulting in a three-phase contact line. Due to the induced change in contact angle by electrowetting, the water then forces the oil to one side. The reverse mechanism or receding process is more straightforward, with the oil re-wetting the hydrophobic surface as the water retracts.

2.6.2. Implementations

Electrowetting-driven reflective pixels pose several challenges that need to be addressed for reliable operations and increased optical performance. For instance, the contrast between covered and uncovered states often referred to as "white area fraction", or "aperture", needs to be maximized. Naturally, the colored oil cannot completely disappear from the light path. In the retracted

state there will still be some fraction of the pixel that will display the colors of the oil. This fraction depends on the pixel size and oil film thickness. Figure 2.17a depicts the relation between pixel size and aperture for different oil thicknesses. The fraction is computed by assuming a hemispherical sphere oil droplet in the contracted state hosted in a rectangular pixel. Using volume conservation between expanded and contracted oil, the surface fractions can be easily computed.

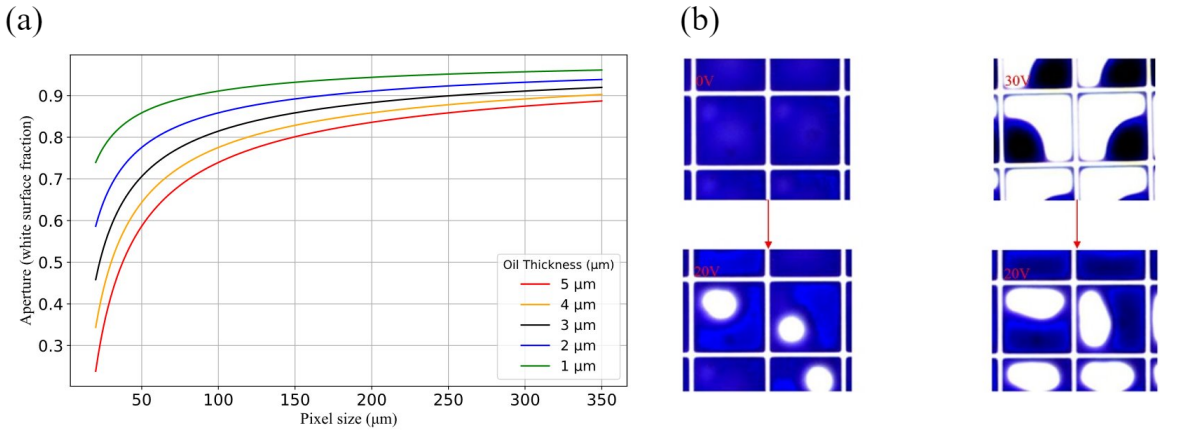

Figure 2.17: Electrowetting challenges. (a) Relationship between pixel size and aperture across different oil film thicknesses. In smaller pixels, thicker films decrease the visible white/transparent area. However, thinner films let more light through, which can lower the contrast. (b) Optical Microscope images showing contact angle hysteresis[115]. Adapted with permission from Ref. [115] under CC BY 4.0 DEED. Copyright (2021) Frontiers in Physics

One can observe that for pixel sizes below 40μm and 5μm oil thickness, the aperture drops below 50%. Thus, to increase display resolution, thinner oil thicknesses are needed. To minimize light bleeding through, oils with higher molar extinction coefficients are thus more desirable. Another challenge to overcome is contact angle hysteresis (CAH). CAH is a well-known physical phenomenon in electrowetting. It is defined as the difference between the advancing contact angle and the receding contact angle observed at the same voltage. Figure 2.17b illustrates an example where there is an aperture discrepancy albeit with the same final applied potential. Increasing the voltage from 0 to 20 V yields a smaller aperture than decreasing the voltage from 30 V to 20 V. CHA makes it more challenging to control precise gray levels in electrowetting displays. CHA has been attributed to random pinning forces, which are caused by surface heterogeneities at smaller scales[88]. These forces can be successfully reduced utilizing an increasing alternating voltage scheme[116] leading to sufficient vibrational energy to overcome the pinning forces.
Finally, it is also important to account for the so-called “Backflow Problem”. In electrowetting systems, a dielectric material is used to separate the conducting electrodes from the liquid. When applying a potential to the system charge trapping can occur in the dielectric layer. These remaining charges can cause the fluid to flow back, even when a constant DC voltage is applied. Charge trapping significantly impacts the stability of electrowetting-based devices. Asymmetric alternative polarity driving schemes[117] are said to reduce charge trapping. In essence, any remaining trapped ions are removed by applying a reset pulse, a small voltage drop with opposite polarity at the signal termination point.

2.6.3. Outlook

Electrowetting-based displays have undergone excessive research and development both in the commercial industry as well as in academic research. Despite their potential for color and video reflective display technology, this innovation never ventured beyond proof-of-concept prototypes. Manufacturing difficulties such as proper sealing and longevity under varying conditions might have been the cause. Moreover, with advancements in display technology, particularly in terms of resolution, electrowetting displays have become less competitive in terms of image quality since oil thickness and pixel size are tightly linked. Nevertheless, electrowetting technology remains a promising area of research with potential applications in areas such as e-readers, smart glasses, and flexible

displays. Current efforts are focused on low-power sunlight-readable electronic billboards, as this application is less stringent on display resolution.

2.7. Electrochromic

Electrochromism refers to the phenomenon where a material's optical properties - transmittance, absorbance, or reflectance - can be reversibly and semi-persistently modified under the application of an electrochemical potential difference. The word "electrochromism" was first introduced in 1961 by J. R. Platt[118] upon his findings that the absorption and emission spectrum of certain dyes could be shifted by applying an electric field. Eight years later, the use of electrochromic materials for display applications was suggested by S. K. Deb[119]. Already then, the slow switching speed was noted as a potential challenge. To this day electrochromism has been utilized in various applications, that do not require fast switching, most notably in smart windows, first reported by Granqvist and Carl M. Lampert Kim in 1984[120], [121], as well as auto-dimming rear-view mirrors[122], [123]. Further applications are protective eyewear[124], [125], or adaptive camouflage[126], [127].

2.7.1. Working Principle

The core principle of electrochromic materials is their ability to change their absorption bandgap, by adding or removing electrons through redox reaction. Electrochromic materials can most often be switched between a transparent ("bleached") state and a colored state, or between two colored states. Polychromic materials may exhibit several colors[128], [129]. The primary mechanisms to achieve a change in electron state are redox reactions, either directly induced or through ion intercalation. The specifics depend on the type of electrochromic material.

2.7.2. Implementations

Electrochromic materials can generally be classified according to their solubility[130] , leading to different device architectures as depicted in Figure 2.18.

Type I EC materials remain soluble in both their reduced and oxidized states. Examples include viologen and heptyl. In device architectures, these materials often have their electrochromic species dissolved directly within an electrolyte, which is sandwiched between two transparent conductive oxide (TCO) substrates. While the fabrication of such devices is relatively straightforward, a critical challenge arises in ensuring the sealing of the devices to avert potential electrolyte leakage. Furthermore, there is an inherent requirement for a continuous supply of current or voltage to uphold their redox states, which could lead to increased energy consumption.

Type II EC materials remain soluble when in their colorless redox state but transition to form a solid film upon the electrode surface when subjected to specific conditions. Devices leveraging Type II materials integrate a redox mediator in the electrolyte, acting as a counterbalance during the redox reactions. This interaction, although promising, does have its challenges. A significant one is the "loss current", a consequence of the direct contact between the redox electrolyte and the EC layer. However, innovations, such as electronic barrier layers[131] or catalytic IrO_x layers[132], provide potential solutions to this challenge.

Type III EC materials stand apart due to their inherent solidity in both redox states. This means they consistently form an insoluble film on the electrode surface. The gamut of Type III materials is extensive, comprising groups IV, and V transition metal oxides, conductive polymers, Prussian blue, and certain metal polymers. In device configurations, these materials typically feature in thin-film "battery-like" setups. Such a device incorporates two substrates coated with transparent conductors, an electrochromic layer, and another layer designated for ion storage or as an additional electrochromic layer. The addition of an ion-storage layer with ample charge capacity ensures a complete and effective color transition, resulting in a device that boasts impressive electrochemical stability.

In practical applications, particularly when considering reflective displays, Type III often emerges as the preferred choice, thanks to its inherent stability and enhanced optical properties.

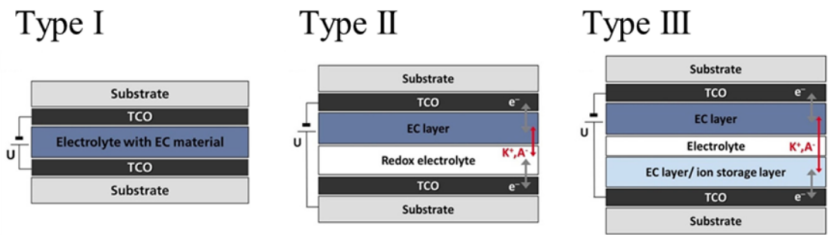

Figure 2.18: Electrochromic display. (a) Schematic diagrams of three types of Electrochromic Devices are shown: A) Type I, which operates in a solution phase; B) Type II, a hybrid system; and C) Type III, also known as the 'battery-like' ECD. K^+ represents cations which could be Li^+ or H^+, and A^- represents anions, for instance, ClO_4^-, Cl^-, BF_4^-, or PF_6^-. Images adapted with permission from Ref. [130] under CC. Copyright (2020) Chemistry Europe.

Electrochromic materials transition from a neutral to an "excited" state during redox reactions, challenging the development of bistable electrochromic devices (ECDs) as they tend to revert to their stable, lower-energy states. This reversion diminishes the longevity of the desired optical state. To counter this, proton-coupled electron transfer [133] and bond-coupled electron transfer [134] have been implemented. These methods avoid the formation of high-energy intermediates. Such intermediates can destabilize the material, reducing its effective life and performance. Electrode materials are fundamental in electron transfer processes. They require meticulously designed energy levels (Fermi levels) that synchronize with those of electrochromic materials. Proper alignment ensures efficient electron transfer and minimizes reverse transfers [135]. Metal dendrites, irregular tree-like structures, can form on electrode surfaces. Their presence disrupts the uniformity of the electron transfer, leading to inconsistent color transitions. To combat this, copper ions have been integrated into bismuth-based systems. The copper ions oxidize bismuth atoms, creating a smoother, spherical morphology. This morphology reduces the chance of dendrite growth, ensuring a consistent electron transfer and uniform color change [136]. For enhanced device responsiveness, multivalent ions, like Al^{3+} are incorporated into tungsten oxide WO_x materials. These ions facilitate rapid and reversible ion insertion/extraction [137]. The increased electrostatic forces between ions lead to an accelerated electron transfer, improving device response time. To diversify the color palette and fasten switching, electrochromic materials are paired with metasurfaces, including Fabry Perot cavities [138], [139] and metallic nanoslits [140]. These metasurfaces induce structural colors and optimize charge-diffusion characteristics. The result is a broader color spectrum and reduced switching times.

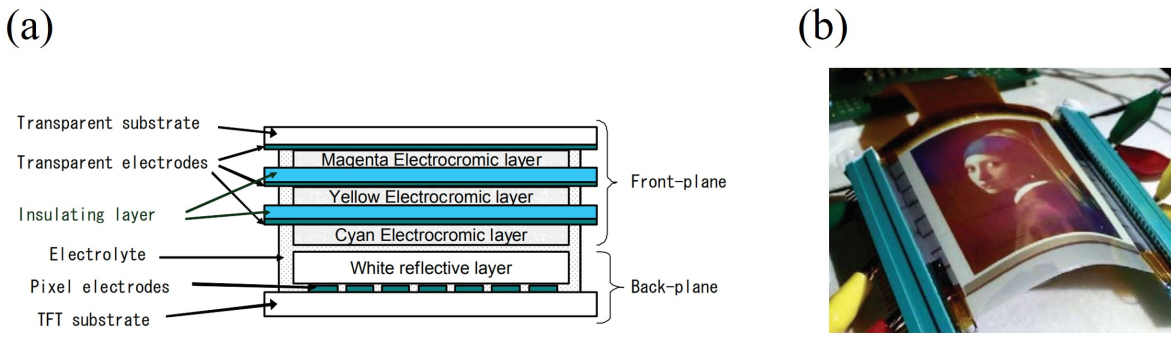

Figure 2.19: Multi-layered, full-color reflective electrochromic pixel. (a) Schematic representation of a unit and (b) a photograph depicting a full-color, flexible, active-matrix-based implementation of the display design. Images from Ref. [141] with permission.

Innovative pixel designs have emerged, utilizing both lateral and vertical configurations[142], [143]. Examples include Urano et al.'s three-layered CMY ECD [144] and RICOH's full-color, flexible matrix display (see Fig. 2.19). These leverage vertically stacked electrochromatic elements. Such stacking allows for brighter color displays, while their flexibility enhances device adaptability[145].

2.7.3. Outlook

EC displays offer numerous benefits: they are inexpensive, low-power, insensitive to viewing angles, and capable of semi-bistability. While electrochromism has already been commercially successful in smart window and glare-reduction applications, commercial displays are still limited to simple monochromatic segmented displays. Continued research and development in electrochromic materials and device architectures are essential to unlock their full potential and drive advancements in particular concerning switching speed, which currently lies around 0.8Hz[91]. Innovations such as the introduction of PEDOT nanotube arrays have shown promise in achieving ultrafast switching speeds compatible with moving-image display technology, suggesting that continued innovation in material science could overcome existing limitations in switching speeds and pave the way for more versatile electrochromic displays[146].

2.8. Phase Change

Phase-change materials exhibit reversible transitions between amorphous and crystalline phases in response to an external stimulus, such as heat, light, or electrical current. Concurrently, variations in physicochemical attributes are observed, encompassing alterations in optical absorbance, and electronic conductance [147]. The phases can be switched very fast, typically 300 ns for GeTe [148], 50 ns for $Ge_2Sb_2Te_5$, 40 ns for $GeSb_2Te_4$, and 30 ns for $GeSb4Te_7$ [149]. Thus, phase-change materials (particularly the germanium antimony tellurium alloy $Ge_2Sb_2Te_5$) have been greatly used in information storage devices since the 1960s [150], for instance in optically re-writable DVDs (DVD-RAMs) [151], or non-volatile resistive based electronic memories[152]. Hosseini et al. [153] pioneered the idea of utilizing nanometer-thin phase-change materials and transparent conductors to generate color-switchable reflective pixels, based on an incident angle-insensitive strong interferometric modulator [154]. Due to their solid-state nature based on phase change materials, this type of display technology has been introduced as Solid-State Reflective Display (SRD). Due to limitations with electrical addressing, discussed in the following section, the previously mentioned switching times can however not be obtained with current display designs. Nevertheless, the fact that this technology does not require any moving parts makes it especially interesting from a manufacturing point of view, as devices could be made using conventional standard vacuum sputtering, bypassing the requirement for sophisticated encapsulation.

2.8.1. Working principle

The material science behind phase change is complex. It has been shown that the switching from crystalline to amorphous state when directly applying current, occurs due to rapid heat-induced dislocation nucleation, electrical wind force transport, and eventual jamming in the crystal, which leads to amorphization [155]. In contrast, the amorphous-to-crystalline transition occurs by heating the material above its crystallization temperature. Upon cooling down, the atoms reorganize into a crystalline lattice, resulting in a lower resistance state. The variations in optical properties arising from these structural modifications can be further understood by examining the corresponding changes in bonding strengths. It is found that the crystalline phase exhibits resonant bonding, whereas the amorphous phase shows covalent bonding [156]. The greater degree of electron delocalization in resonant bonding materials, as opposed to covalent bonding, can have a significant impact on the optical characteristics of the material. The higher level of interaction between delocalized electrons and incident electromagnetic waves produces specific absorption, transmission, and reflection characteristics, resulting in optical performances that differ significantly from materials having localized covalent bonding. On a broader scale, individual phase-change-based pixel designs differ. However, the primary objective is to engineer a wavelength-dependent tunable resonance, that is then tuned by the phase-change material, inherently altering the resonance conditions due to a change of optical properties when switching from an amorphous to a crystalline state.

2.8.2. Implementations

When directly applying current to the switch state, the material undergoes a partial phase change until a low-resistance pathway is established[157]. This pathway subsequently functions as a channel for the residual current, impeding a full-phase transition. This phenomenon is referred to as the "filamentary switching issue" [157]. Utilizing nanoscale pixels can effectively reduce this issue. How-

ever, addressing such a vast number of pixels individually and simultaneously presents a challenge. The computational and energy demands of peripheral driving circuits for pixel addressing increase considerably as the number of pixels increases [158]. Thus, alternative more homogenous switching methods need to be envisioned. To avoid the filamentary switching issue much effort has been devoted to the design of decoupled micro-heaters as a means to uniformly fully switch the phase-change material[158], as shown in Fig. 2.20. A typical phase-change-based pixel structure is depicted in Fig. 2.20a. The SRD pixel consists of three primary layers. Notably an electronic substrate directing drive signals to specific pixels, a microheater that converts electrical signals to uniform thermal pulses, and finally an optical layer reflecting specific colors in stable PCM states via strong interference effects.

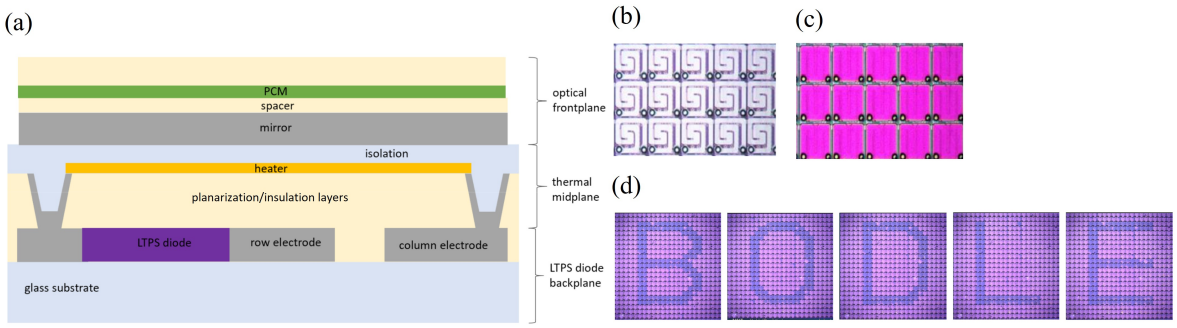

Figure 2.20: Figure 21 Microheater-based phase change display system. (a) Schematic of the SRD pixel structure (b) microheater array, (c) the assembly comprising a mirror and thin-film interference stack, and (d) a microscope photograph demonstrating a 24x24 pixel region being dynamically updated with a sequence of letters. Images with permission from Ref. [158]. Copyright (2019) Society for Information Display

2.8.3. Outlook

Efforts to increase color saturation can be achieved by higher refractive index and lower loss materials than GST or GeTe, such as antimox trisulphide $(Sb_2 S_3)$ or antimony triselenide (Sb_2Se_3) [159]. While noticeable switchable color changes are possible, little has been demonstrated of producing a black state, needed for a fully functional display. When switching phase, the real part of the refractive index GST material usually exhibits a change of roughly 1.5 to 2, while the absorption coefficient can be altered by more than 3 [160]. Essentially, for a given pixel design, the resonance sensitivity to a variation in optical constants needs to be increased for a black state to exist. In such a state the resonance would need to be shifted outside the visible domain. So far this remains a challenge. Furthermore, the use of microheaters severely limits the switching times. Frequencies of mere 2 Hz are reported [158]. With approximately 100 mJ$/$cm^2 [160] microheaters also consume more energy per frame than electrostatic-driven systems.

2.9. Tunable Photonic Crystal

The theoretical work of Yablonovitch [161] and John [162] serves as the foundation for the idea of photonic crystal materials. Materials can be created to alter photon properties in a manner comparable to how conventional semiconductor crystals alter electron properties. The propagation of light waves through the substance can be controlled by periodically structuring the material. This makes it possible to produce photonic band gaps, which are wavelength bands that cannot pass through the substance. Since its early days, photonic crystals have been successfully applied in various examples, such as filters, sensors, solar cells, and recently into smart windows to regulate building energy consumption [163]. Photonic crystals have emerged as an interesting technology for reflective displays due to their continuous color tunability, essentially avoiding the need for sub-pixelation for display colors. This can lead to higher color purity and increased resolution.

2.9.1. Working principle

1D Photonic crystals colorful appearances result from interference and reflection. The wavelength that is coherently scattered is centered on λ, and can be estimated by by the Bragg-Snell equa-

tion[164]:

$$\lambda = 2D\left(n_{eff}^2 - \cos^2(\theta)\right)^{\frac{1}{2}} \tag{2.11}$$

where λ is the wavelength of the reflected light, n_{eff} is the average refractive index of the photonic materials, D is the diffractive plane spacing, and θ is the Bragg angle of incidence.
Based on Eq. 2.11 the different ways to alter the reflected wavelength can be inferred, namely by modifying the three variables which are the diffractive plane spacing, the average refractive index, or the Bragg incidence| angle.

2.9.2. Implementations

Most photonic crystal-based reflective pixels are based on acting on the inter-plane distance to modulate the reflected wavelength. The key challenges are to find fast-switching methods as well as ways to respond to the inherent angle incidence dependence of such photonic crystals, which can be seen in Eq. 2.11.
For the most part, inter-plane distance variations are achieved in electrochemical swelling-driven color change displays [165] or electrokinetic-driven reflective displays [166]. While crystalline structures have shown excellent color tunability, their practical application has been severely impeded by their intrinsic angle dependency. It has been demonstrated [167], [168] that colloidal structures that are made up of particles with sizes similar to optical wavelengths and exhibit short-range order but lack lattice periodicity, exhibit independence of the incident angle. These systems [166], [169] have therefore been seen as promising candidates for color-tunable reflective displays, albeit with lower peak reflectivity values of generally around 25 - 30 % (see Fig. 2.21c).

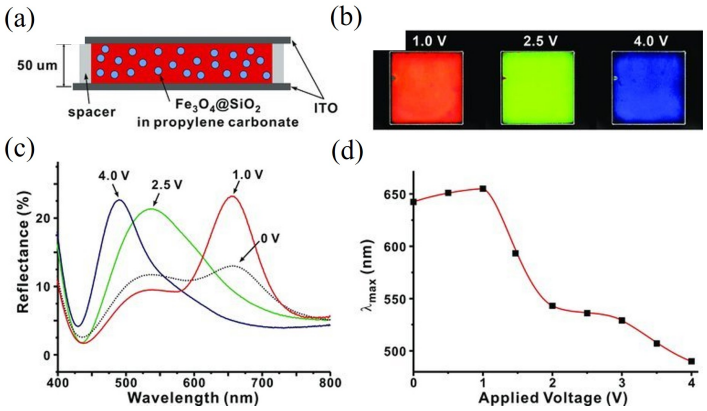

Figure 2.21: Photonic display pixel. (a) Schematic design of the photonic display pixel. (b) Photographs at varying bias voltages: 1.0 V, 2.5 V, and 4.0 V. (c) Reflection spectra recorded at increasing bias voltage levels. (d) Illustrates the 165 nm shift of the photonic band position from 655 nm to 490 nm, governed by the applied voltage. Images from Ref.[166] with permission.

2.9.3. Outlook

Switching times of approximately 50 ms [166] have been documented in tunable photonic crystals, which, although not yet suitable for video applications, demonstrate potential for improvement. One possible approach to enhance the switching speed is through the employment of lower-viscosity liquids, which may facilitate a faster response time. Furthermore, the trade-off between angle-independence and color intensity presents another challenge. While amorphous photonic structures have shown reduced angle independence, they also exhibit reduced peak reflectivity and less vibrant colors. This is due to the incoherent scattering events caused by their disordered arrangement, resulting in weaker constructive interference and diminished color intensity. Hierarchical photonic structures [170], [171] have been proposed to produce both angle-independent and bright colors, but further investigations and optimization are required to address these limitations and fully realize the potential of tunable photonic crystals in display technologies. Finally, it is worth mentioning that while continuous color can be produced, it has yet to be shown how to produce white without

resorting back to an area-sharing subpixel layout such as RGB. Commercially, two companies are pioneering modulation approaches using photonic crystals. Opalux focuses on color-tunable Photonic Ink, while Nanobrick works on full-spectrum tuning using SiO_x-coated nanoparticles.

2.10. Discussion

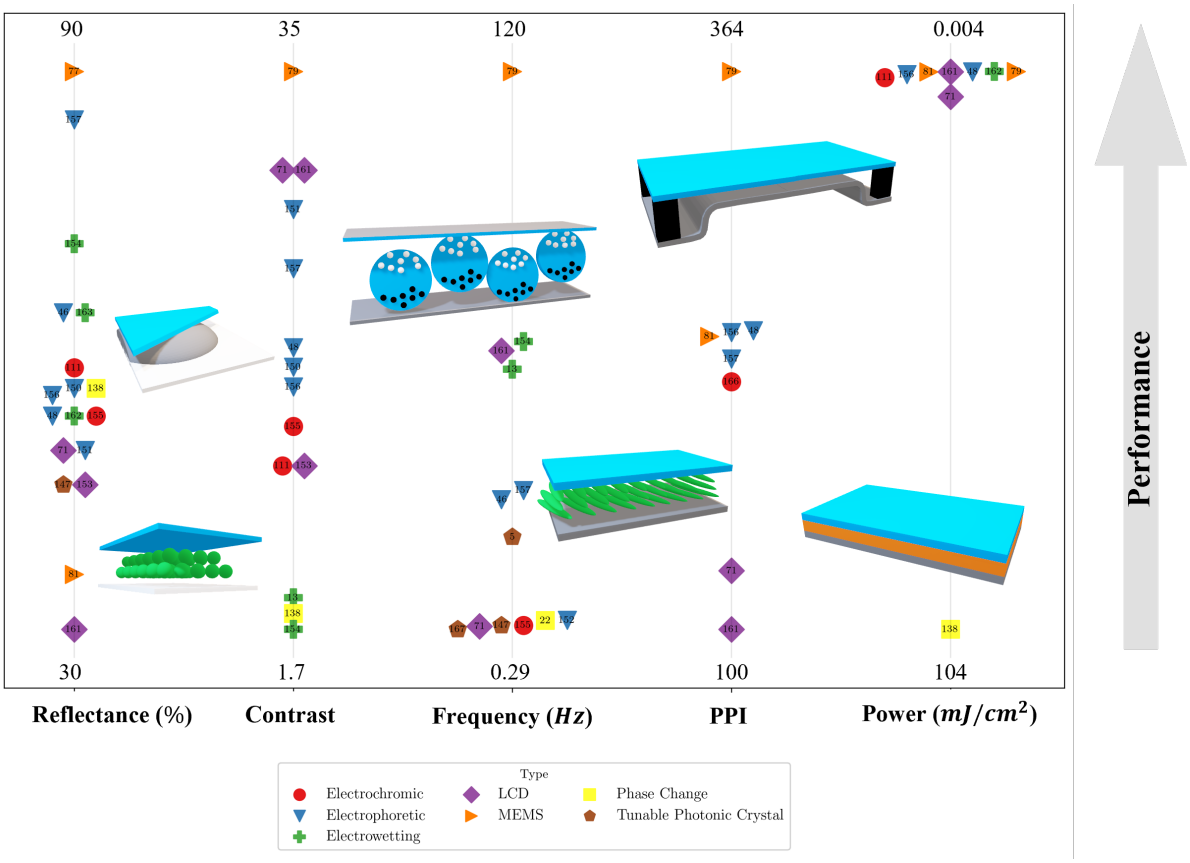

Figure 2.22: Performance map for reflective display technologies: This representation compares diverse reflective display technologies based on their essential performance parameters. Microcapsule Electrophoretic Displays (Reflectance: 44% [172], Contrast: 23 [173] , Frequency: 2.1 Hz [174]) and their ChLCD (Reflectance: 35% [91], Contrast: 10 [175], Frequency: 0.8 Hz [91]) and Electrochromic counterparts (Reflectance: 47% [127], Contrast: 12, Frequency: 1 Hz [176]) find their niche in applications demanding static images given their constrained refresh rates. Conversely, emerging Electrowetting displays, exhibiting up to 65% reflectance and a remarkable 62 Hz frequency [173], signal promise for dynamic video renditions. Phase Change Displays, with a reflectance mirroring that of electrophoretic at 44% [177], are however marked by a considerable refresh energy density of 104 mJ/cm^2 [177]. Albeit discontinued commercially, MEMS-based Qualcomm designs achieve a stellar 90% [95], contrast-ratio of $1:30$ [100], and a swift 120 Hz [100] , all while being impressively efficient at 0.004 mJ/cm^2 [100]. Numeric values can be found in Table A.1.

Microcapsule electrophoretic displays, featuring reflectance up to 44%[172], contrast ratios of 23[173], and a frequency of 2.1 Hz[174], have achieved commercial success. They offer an optimal blend of readability and energy efficiency with a refresh energy density of 0.58 mJ$/$cm^2[178]. The modulation of total internal reflection using electrophoretic mechanisms further enhances these displays, achieving reflectance up to 83%[179], maintaining a contrast of 20[179], and reaching frequencies of around 30 Hz[67], while maintaining an impressively low refresh energy density of 0.029 mJ$/$cm^2[67]. ChLCDs, utilizing cholesteric liquid crystals, present reflectance around 35% [91] and contrast ratios close to 10 [175]. Their limited response time of 0.8 Hz[91], however, restricts their utility in mobile devices, reserving them for specific applications, such as shelf-labels, where high refresh rates aren't essential. Similarly, electrochromic displays, offering reflectance between 40%[177] and 47%[180] and contrasts up to 12[177], operate at a frequency of approximately 1 Hz[177], thus they too face challenges for integration into mainstream mobile devices.

Electrowetting displays, although nascent, exhibit promising metrics with reflectance peaking at 65%[176], though they have a modest contrast of 1.7[176] . Their highlight is a frequency that reaches 62 Hz[176], indicating a potential for fluid video playback.
Phase change displays, characterized by their non-volatile solid-state pixels, present a reflectance of 44%[160], comparable to commercial electrophoretic displays. Despite this notable similarity in reflectance, other metrics such as a contrast of 2.5[160], a frequency of 2 Hz[160], and a high refresh energy density of 104 mJ/cm^2[160] underline areas that need improvement for this technology to achieve a competitive standing. Additionally, it has not yet been demonstrated how to produce a black state by the sole use of SRD pixels.
Tunable photonic crystals stand out for their potential to display continuous colors within individual pixels. Their current implementations, achieving white state reflections between 30% and 60% [169] and reported 20 Hz frequency [30], could be an interesting venue to explore further. Switching speed needs to be improved to yield video playback possibilities, as well as further reduction of angle dependence and the ability to show white.
Concluding, MEMS-based reflective displays, especially the interferometric absorption-based design by Qualcomm, are exemplary. They manifest a 90% reflectance [99], a contrast of 30[100], and an impressive frequency of 120 Hz [99] , complemented by a PPI of 363 [99] and a minimal refresh energy density of 0.004 mJ/cm^2[99].
Beyond core metrics, the mitigation of inadvertent internal reflections is paramount in e-paper technology. Although these displays capitalize on ambient light reflection, undesirable internal reflections - often from thin film interfaces - can compromise performance. Advanced techniques, such as index matching and multilayer destructive interference, have been employed to counteract these challenges. Notably, antireflective coatings inspired by nocturnal moth corneal patterns[181] have achieved reductions in spurious reflectivity to a mere 0.1% within the visible spectrum[182]. Raut et al. provide a thorough discussion on this reflection management [183].

2.11. Conclusion

The state of the art has covered a variety of reflective display technologies. Despite significant research efforts, reflective displays are generally absent in typical mobile devices such as smartphones and smartwatches. This is particularly critical given the inherent benefits of these displays, such as longer battery life and improved visibility in bright outdoor environments. The primary obstacles hindering their widespread integration into mobile devices are the current limitation of refresh speed and the compromised color vibrancy that many of these technologies exhibit. For example, while reflective LCDs are capable of video playback, their white state reflectivity is constrained to approximately 9% [184], thereby affecting the saturation of displayed colors. In contrast, microcapsule electrophoretic displays showcase a considerably higher reflectance, reaching up to 44% [183], but suffer from restricted refresh capabilities. Within the realm of emerging technologies, ClearInk's TIR display technology offers a promising avenue for augmenting the update speed of electrophoretic-based displays. Concurrently, MEMS-based technologies are gaining prominence thanks to their inherent rapid switching times, high contrast ratios, and relative energy efficiency. Furthermore, graphene-based interferometric modulators have demonstrated remarkable capabilities, achieving refresh rates of up to 400 Hz and ultra-high resolution [102]. In summary, the landscape of reflective display technologies is diverse, with each presenting a distinct set of advantages and drawbacks. Whether prioritizing energy efficiency or optical performance, the array of options is broad and expanding. This diversity, underscored by the key performance metrics outlined in this review, suggests a promising future for reflective displays. As research in this field continues to advance, the integration of these low-power, high-performance display systems into mainstream mobile devices becomes an increasingly tangible prospect.

3

Design Methods

This chapter presents a detailed exploration of both optical and mechanical design methodologies, specifically tailored to enhance optical performance metrics and to compute the estimations for pull-in voltage and switching time. The objective in our design framework is to attain a high contrast ratio in the vicinity of 10:1, a benchmark crucial for ensuring optimal readability in outdoor environments (see Table 2.1). Additionally, our design aims to achieve a deep, rich black in the actuated state, and white in the idle state. The optimization routine was written to be general, such that one could also optimize for another color than white.
To calculate the spectral-average reflectivity of a reflection spectrum, we use the following integral formula:

$$\overline{R} = \frac{1}{\lambda_2 - \lambda_1} \int_{\lambda_1}^{\lambda_2} R(\lambda)\, d\lambda \tag{3.1}$$

where $\overline{R}$ is the spectral-average reflectivity, $R(\lambda)$ is the reflectivity as a function of wavelength λ, and λ_1 and λ_2 are the bounds of the visible spectrum, specifically 400 nm and 700 nm. Following this, the spectral-average contrast ratio can be determined using the reflectivity values in both the idle and actuated states:

$$CR = \frac{\overline{R}_{\text{idle}}}{\overline{R}_{\text{actuated}}} \tag{3.2}$$

In Equation 3.2, CR represents the contrast ratio, with $\overline{R}_{\text{idle}}(\lambda)$ and $\overline{R}_{\text{actuated}}(\lambda)$ indicating the reflectivity functions in the idle and actuated states, respectively, across the visible spectrum range.
The simulation of tunable metasurfaces for reflective display applications is conducted under the assumption of normal incidence plane waves. This approach is substantiated by the physical characteristics of sunlight as it reaches the Earth when no clouds are present. Considering the vast distance of approximately 1.5×10^8 km (1 astronomical unit) from the Sun to the Earth, the radius of curvature of the sunlight's wavefronts is substantially large. Mathematically, the curvature C of a spherical wavefront can be expressed as the reciprocal of its radius R, given by $C = \frac{1}{R}$. For sunlight, this curvature is calculated to be approximately 6.67×10^{-9} km^{-1}, indicating an extremely small value. Due to this negligible curvature over the scale of typical observational setups on Earth, it is reasonable to approximate the sunlight wavefronts as plane waves.
This simplification is primarily applicable to clear outdoor conditions. However, its applicability is limited under diffuse lighting scenarios, such as cloudy or indoor environments, where light scattering is more prevalent. A comprehensive analysis, extending beyond the scope of this study, would necessitate the computation of the full bidirectional reflectance distribution function (BRDF), as delineated in the work of Hertel and Penczek [25]. The BRDF is instrumental in understanding the interaction of reflective displays with light incident from various angles, which is vital for predicting display performance across a spectrum of ambient conditions.

The performance of reflective displays is contingent upon the nature of light reflection, which can be classified into three primary types: specular, Lambertian, and haze reflections. Specular reflections, characteristic of glossy surfaces, produce mirror-like images. Lambertian reflections, typical of matte surfaces such as ePaper, scatter light uniformly across all directions. Haze reflections, observed on antiglare surfaces, exhibit properties of both specular and Lambertian reflections.
The interplay of these reflection types with diverse illumination sources – ranging from direct sunlight to diffused skylight and artificial light – markedly influences display visibility and readability. Accurately modeling these interactions poses a significant computational challenge. Due to the complexities involved and the high computational demands, this study has been constrained to normal incidence simulations. Future research endeavors could potentially incorporate BRDF models to more precisely capture the intricate behaviors of reflective displays under varied lighting conditions, thereby augmenting our understanding and predictive capabilities regarding display performance in real-world applications.

3.1. Optimization Pipeline

A Python optimization pipeline is implemented to optimize reflected color from nanostructures. More specifically, a Python-based particle swarm optimization (PSO) routine is utilized to automatically converge towards suitable geometries that would produce a desired reflected color, defined in the sRGB space. Figure 3.1 shows a typical convergence graph of the geometric optimization. It depicts the error function with respect to the set goal. We can see it steadily declining and eventually settling after approximately 3000 iterations. The intermediate peaks represent the algorithm search algorithm, exploring various configurations, occasionally moving away from local minima in an attempt to find a more optimal solution. This behavior is characteristic of PSO, where particles representing potential solutions move through the search space influenced by their own and their neighbors' previous best positions. The diminishing fluctuations in score imply that the potential solutions are converging around a geometry that produces a color close to the target in sRGB space. The graph suggests that the algorithm has effectively navigated the complex search space of nanostructure geometries to arrive at a satisfactory solution.

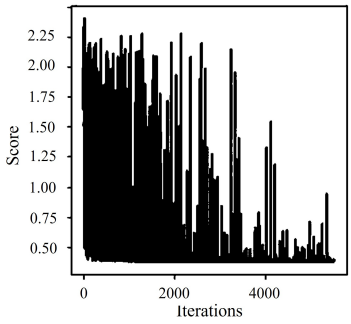

Figure 3.1: Typical convergence plot of the optimization pipeline.

The routine is shown in Figure 3.2. Given an initial (guessed) geometry, electromagnetic simulation software is used to compute the far-field reflection spectrum upon normal incidence. The reflection spectrum is then further converted by the Python package "Colour" into screen color sRGB, based on the CIE (Commission Internationale de l'éclairage) 1931 2° Standard Observer shape. Given the output as well as fabrication constraints the PSO python package "pyswarms" computes the parameters for the next geometry to test. The new geometry suggestion is then forwarded to the electromagnetic (EM) simulation software and the cycle repeats. PSO has the advantage of being a gradient-free optimization method, however, it cannot be guaranteed to find a global minimum. Since each EM simulation is computationally expensive and time-consuming, a machine learning (ML) method, boosted trees, is further implemented that continuously tries to predict the spectra. Once the error between prediction and simulated output falls below a threshold the ML model takes over and is periodically checked by the rigorous EM simulation. This drastically reduces the cycle time. In the following, each part of the optimization pipeline is explained in greater detail.

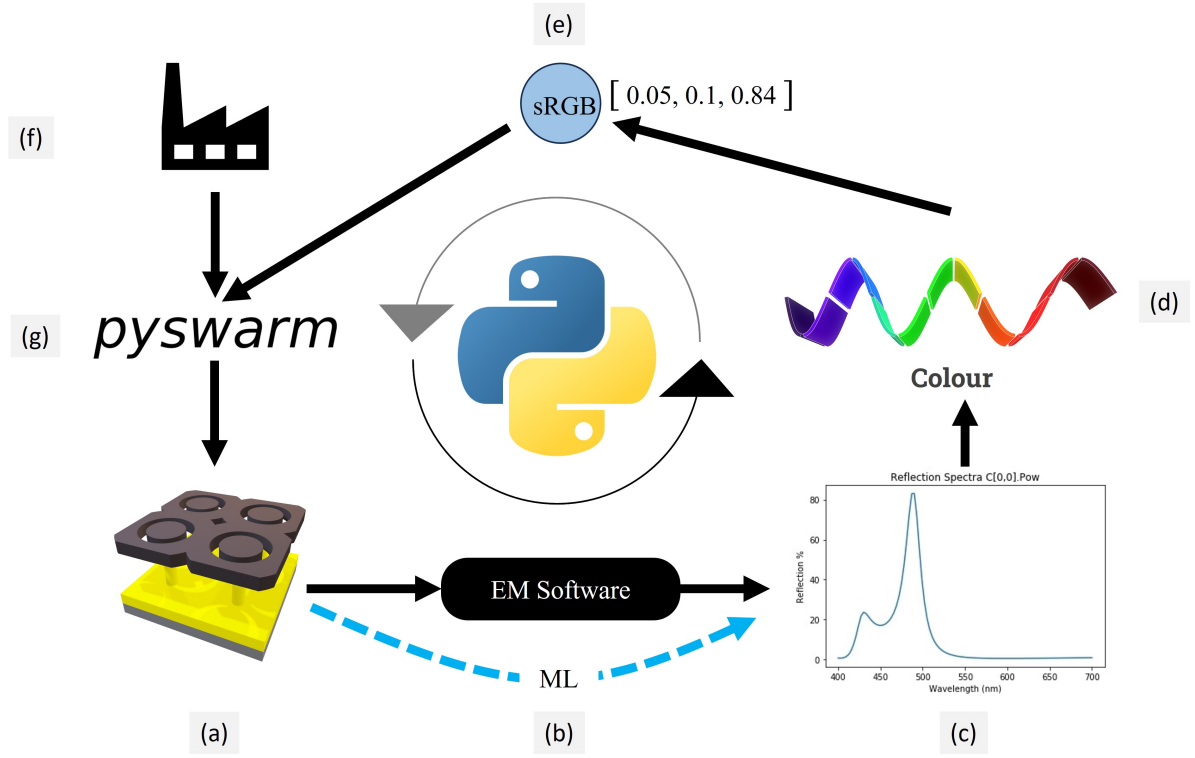

Figure 3.2: Visualization of Optimization Method Python Implementation a) Geometry Script File; b) Electromagnetics wave simulation; c) Result: 0th Order Reflection Spectrum; d) Python Package: Colour; e) Result: Converted sRGB colorspace; f) fabrication Constraints; g) modified Python Package: pyswarm

3.1.1. Python Wrapper for EM Software

The EM Software used is “MC Grating” [185]. It computes the reflection, transmission, and absorption of light due to periodic nanostructures utilizing rigorous coupled wave analysis (RCWA). Briefly, RCWA works by extending the fields with Fourier transforms, discretizing the structure into layers, and solving Maxwell’s equations inside each layer. Its strength resides in its ability to produce a precise answer without oversimplifying assumptions, making it particularly ideal for intricate nanoscale research in photonics, optics, and related domains. MC Grating does not provide Python integration by default, thus a Python wrapper [186] was built to facilitate (1) the creation of geometries including a full 3D rendering for visual validation, (2) to allow Python to control MC grating during the optimization routine, and finally (3) to directly plot and analyze simulation data in python. Figure 3.3 visualizes the different visualization capabilities of the Python wrapper. While in the underlying software, MC Grating, all geometries are hard-coded by inputting the corner points of each geometry in a layer-like fashion, the wrapper allows to use of predefined objects such as cylinders or cuboids. Furthermore, these objects can be attributed to an ”importance factor”. For instance, the holes in the membrane are created by having an air cylinder that crosses a cuboid, where the air cylinder has a higher importance factor than the cuboid. This methodology allows for very fast and organized builds of different geometries. As visualized in Figure 3.3 the wrapper also allows to showcasing of those geometries in various 2D cross-sections as well as full 3D for better feedback, before launching the simulation. Post-simulation, the wrapper allows to handling of all generated data directly in Python. All the most common visualizations are directly implemented as functions, such as visualizing the spectra of reflection, absorption, and transmission, and the different orders (if present). Furthermore, far-field radial plots allow to visualize the angles and intensity of reflection spectra. Then, the code is also capable of showing various near-field cross-sections, such as the amplitude of the magnetic field or electric field, its different components, or the pointing vectors. The wrapper thus clearly extends the capabilities of MC Grating. For this reason, as an appreciation, MC Grating decided to gift the original software license.

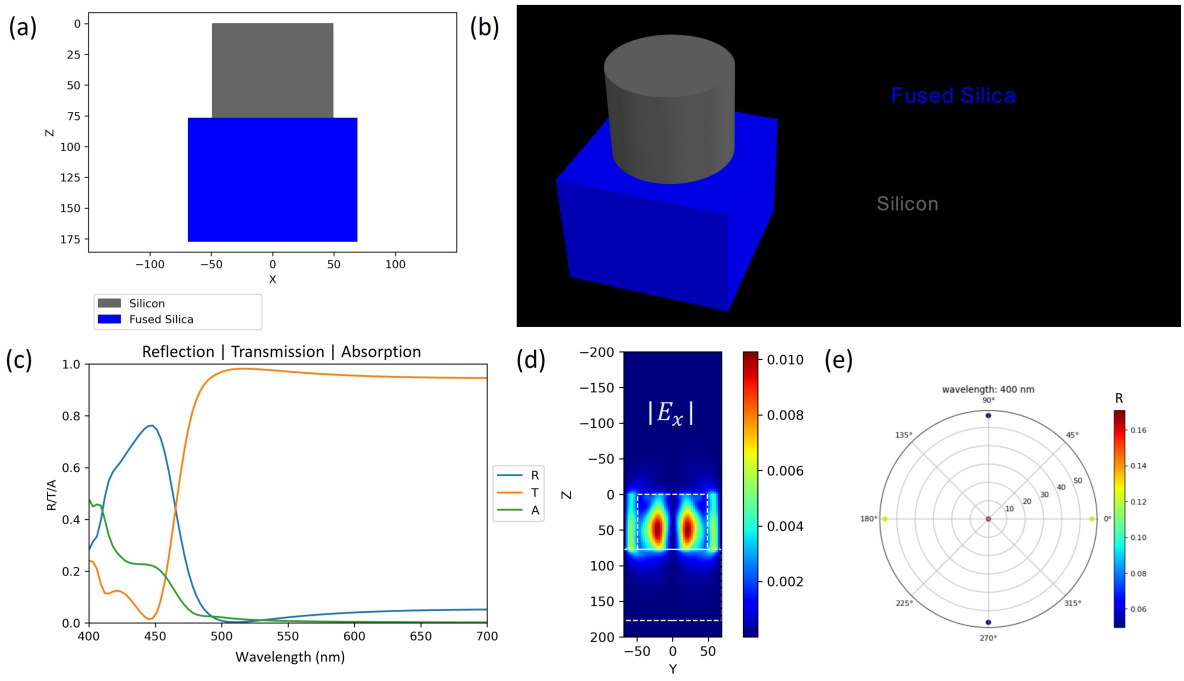

Figure 3.3: Python Wrapper for MC Grating. (a) Cross-sectional and 3D (b) view of generated geometry, (c) reflection-transmission-absorption spectra as well as (d) near-field plots (source-normalized to show field enhancement) or (c) far-field scattering plots.

3.1.2. Constraint Particle Swarm Optimization

Given the complexity of the interaction of light with nanostructures, it is extremely difficult to come up with reliable analytic expressions to link geometric parameters with optical performance metrics. The influence of specific geometric configurations can be computed by numerically solving Maxwell equations, however, the evolution of the optical parameters with respect to the geometric parameters is often unknown. Since the underlying function defies description through derivable equations, conventional gradient-based optimization techniques, such as Newton's method, are not applicable. Hence, the deployment of gradient-free optimization methodologies becomes imperative. These strategies endeavor to pinpoint an optimal resolution, even when the foundational function remains obscure, and are therefore often called "heuristic optimization" as they make no assumption about the underlying problem. Particle Swarm Optimization (PSO) is a heuristic optimization technique inspired by the social behavior of birds and fishes. Each "particle" is a combination of input and associated output. Each particle's movement is influenced by its memory of the best position it has encountered and the global best position found by any particle in the swarm. Starting with a randomly initialized swarm, each particle's position is iteratively updated based on personal and global components. The vector by which the current position of each particle is shifted can be computed as follows:

$$\begin{aligned} s_{\{\mathrm{i,t}\}} &= \omega \cdot s_{\{\mathrm{i,t-1}\}} \\ &+ \phi_{\mathrm{p}} \cdot \mathrm{r}_{\{\mathrm{p,i}\}} \cdot \left(\mathrm{p}_{\{\mathrm{i,t-1}\}} - \mathrm{x}_{\{\mathrm{i,t-1}\}}\right) \\ &+ \phi_{\mathrm{g}} \cdot \mathrm{r}_{\{\mathrm{g,i}\}} \cdot \left(\mathrm{g}_{\{\mathrm{t-1}\}} - \mathrm{x}_{\{\mathrm{i,t-1}\}}\right) \end{aligned} \tag{3.3}$$

where:

- Subscripts g and p -> global, personal
- ω : Particle velocity scaling factor
- ϕ_{p}: Scaling factor to search away from the particle's best-known position.
- ϕ_{g} : Scaling factor to search away from the swarm's best-known position.
- $r_{\{p,i\}}, r_{\{g,i\}}$: Random numbers uniformly distributed between 0 and 1 for particle i

- $p_{\{i,t-1\}}$: Best-known position of particle i at iteration $t-1$
- $g_{\{t-1\}}$: Best-known position of the entire swarm at iteration $t-1$
- $x_{\{i,t-1\}}$: Position of particle i at iteration $t-1$

As can be seen from equation 3.3 the shift vector $s_{\{i,t\}}$ in PSO is essentially a weighted sum of three terms, namely the inertia (the last shift), personal component (individual particle's best-known position), and social component (global or swarm's best-known position).The particle's position is then updated with the following equation:

$$\mathrm{x}_{\{\mathrm{i,t}\}} = \left\lfloor \mathrm{x}_{\{\mathrm{i,t-1}\}} + s_{\{\mathrm{i,t}\}} \right\rfloor \tag{3.4}$$

Once the particle positions are computed, they are constraint-checked, and all feasible positions are evaluated. The result is fed into an error function that computes the distance between the result and the wanted optimized result. The smaller the returned error, the better. Upon each iteration, the error for each particle is compared to the previous personal errors and global errors, and the best personal and global position is recorded. This loop continues to execute for a given number of iterations or until a certain error threshold is met. In our case, each particle position essentially represents a set of geometric parameters.

Feasibility check: Before running a costly EM simulation, the geometric parameters are further checked for feasibility utilizing constraint functions. This allows us to make sure that the tested geometry is physically meaningful, i.e. The period should always be larger than the dimensions of the object inside the unit cell of a periodic grid, as well as the maximum membrane displacement cannot be more than the pillar height.

Constraints: In addition to feasibility checks, fabrication constraints can also be integrated into the PSO algorithm. In the present case, it was decided that the gap could be a minimum of 20 nm, which is close to the limits of given e-beam lithography capabilities at the CMi. As for the pillar height, a maximum aspect ratio of 5:1 was set. In addition, the period was constrained to be at maxima 400 nm, which is the largest period that allows to building of non-diffracting elements in the visible for a periodic array.

If these criteria are not validated, the EM simulation is skipped for these particles and the error for those particles is set to a very high number, essentially discouraging the swarm from continuing further in this direction. By design, PSO does not guarantee a global optimization, but it has shown invaluable in many engineering applications[187]. The particle swarm optimization was implemented using a modified version of the Python package "pyswarm" [188] and can be found in the appendix A.3. Notably, it was ensured that all values remain integer since sub-nanometer optimization of the geometry does not make sense as the tolerances could not be met in the cleanroom.

3.1.3. The Optimization Function

The optimization pipeline was designed to be as versatile as possible for optimizing reflective metasurface in the visible. A common goal of such metasurfaces is to show specific colors, thus it was important to convert the simulated reflection spectrum into human-perceived color and to compute its difference from the color that is aimed.

Spectrum to XYZ

Color-matching functions (CMFs) are used to convert the spectral distribution into human-perceived color. This is done more explicitly through the CIE 1931 2 Degree Standard Observer model. It maps the recorded spectra into the CIE XYZ color space. The 'Y' component corresponds to luminance, describing the brightness or intensity of a color. Chromaticity, represented by the 'X' and 'Z' components, focuses on color quality. This model is intended to characterize the average human's chromatic response within a 2° visual field of the fovea centralis, a region of the eye where color-sensitive cones are densely concentrated. In essence, it links our visual perception to the specific wavelength. Equation 3.5 is the mathematical equation to calculate the CIE XYZ tristimulus values from a given spectral distribution using the provided color-matching functions and illuminant.

$$\begin{bmatrix} X \\ Y \\ Z \end{bmatrix} = k \cdot \sum_{\lambda} P(\lambda) \cdot \begin{bmatrix} x(\lambda) \\ y(\lambda) \\ z(\lambda) \end{bmatrix} \cdot \Delta\lambda$$
$$= k \cdot \sum_{\lambda} R(\lambda) \cdot I(\lambda) \cdot \begin{bmatrix} x(\lambda) \\ y(\lambda) \\ z(\lambda) \end{bmatrix} \cdot \Delta\lambda \tag{3.5}$$

where:

- X, Y, Z are the resulting tristimulus values.
- k is a normalizing constant.
- $P(\lambda)$ represents the emissive spectral power distribution.
- $R(\lambda)$ represents the spectral power distribution of the reflectance, transmittance, or radiance.
- $I(\lambda)$ represents the spectral power distribution of the illuminant.
- $x(\lambda), y(\lambda), z(\lambda)$ are the color matching functions for the X, Y, and Z coordinates.
- $\Delta\lambda$ is the wavelength interval, representing the integration step over the continuous spectrum.

The normalization constant k is chosen such that the intensity (Y) of a 100% reflective object is scaled to 100. This means that when the incoming light is equal to the reference illumination, the attributed value is 100.

$$k = \frac{100}{\sum_{\lambda} Y(\lambda) \cdot I(\lambda) \Delta\lambda} \tag{3.6}$$

XYZ to RGB

In the pursuit of optimizing a metasurface for a specific reflected color, it's essential to maintain consistency from the design phase to the final observation. Converting from XYZ space to RGB space serves this purpose, as the initial color selection is performed on a standard RGB monitor, ensuring that the chosen color remains consistent throughout the entire process. As RGB is a relative color space—where different shades of red, green, or blue could all be considered "primary colors"—the exact specification of one's monitor color definition would need to be measured to achieve the most accurate design-to-fabrication result. At the current stage of the project, however, this level of precision appears unnecessary. Therefore, the XYZ space is converted into standard RGB (sRGB), a common standard that most monitors comply with, to maintain a reasonable level of accuracy and consistency. sRGB was introduced in 1996 [189] in cooperation with Hewlett-Packard and Microsoft, and later standardized by the International Electrotechnical Commission (IEC) as IEC 61966-2-1:1999 [190]. Essentially, suitable red, green, and blue values were identified within the XYZ colorspace that could be represented by monitors and printers. Equation 3.7 describes the transformation:

$$\begin{bmatrix} sR \\ sG \\ sB \end{bmatrix} = \begin{bmatrix} 3.2406 & -1.5372 & -0.4986 \\ -0.9689 & 1.8758 & 0.0415 \\ 0.0557 & -0.2040 & 1.0570 \end{bmatrix} \begin{bmatrix} X \\ Y \\ Z \end{bmatrix} \tag{3.7}$$

The code to convert a spectrum to its sRGB representation is given in appendix A.4.

3.1.4. Machine Learning EM Simulation Speed Up

A critical introduction to speed up the pipeline, is the application of machine learning to predict simulation outcomes, specifically using the Light Gradient Boosting Machine (LightGBM) algorithm [191]. LightGBM is a gradient-boosting framework that generates a prediction model as an ensemble of weak learners, primarily decision trees. On a high level, the model is designed to minimize a loss function $L(y, F(x))$, where y is the actual label (in our case, the reflected power) and $F(x)$ is the predicted label. The objective is to fit the residual errors by adding N weak learners $f_i(x)$ iteratively, mathematically expressed as:

$$F(x) = \sum_{i=1}^{N} f_i(x) \tag{3.8}$$

For each wavelength in the spectrum, given the input geometric parameters, the spectral response is predicted. These predictions serve as rapid, approximate, insights into what the RCWA simulation would yield for a new set of parameters. This reduces the computational load, expediting the optimization process. The loss function is defined as the area difference between predicted reflection spectra and simulated (see Figure 3.4). Initially, MC Grating simulates all optical responses to the provided geometries, and the data is used to train LightGBM. Once the loss function falls below a certain threshold, the ML algorithm takes over and MC grating is only periodically used to verify the predicted results.

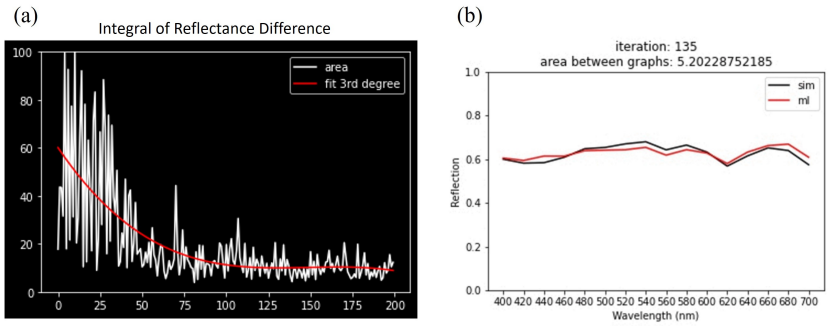

Figure 3.4: Optimization speed improvement through machine learning utilizing LightGBM (a) area difference between (integral of the reflectance difference between the predicted and simulated reflection spectra) (b) exemplary predicted spectra versus simulated spectra after 135 iterations

In a quantitative comparison of computational efficiency, the machine learning model demonstrates a substantial enhancement over RCWA simulations. Specifically, the mean computational time required for each geometry in the RCWA simulation was observed to be 6 seconds. In contrast, the machine learning model necessitates a mere 0.005 seconds for making equivalent predictions. This translates to a computational speed-up factor of approximately 1200 times, thereby representing a significant reduction in computational time and resources.

3.2. Pull-In Voltage computation

The pull-in voltage, a crucial parameter in Micro-Electro-Mechanical Systems (MEMS), dictates the operational limit of such devices. It represents the threshold voltage at which electrostatic forces overcome mechanical restoring forces, causing the device to snap down or "pull-in". Prediction and understanding of this parameter is essential for the design and reliability of MEMS devices. In the following, a basic computational approach is outlined to estimate the pull-in voltage of a general MEMS device consisting of an air-layer for the MEMS displacement, as well as N dielectric layers. For a given layer i in the MEMS device (see Figure 3.5a), the capacitance C_i is defined as:"

$$C_i = \frac{\epsilon_0 \epsilon_i A}{t_i} \tag{3.9}$$

where:

- ϵ_0 is the permittivity of free space,
- ϵ_r is the relative permittivity of the layer,
- A is the area of the capacitor, and
- t_i is the thickness of the i^{th} layer.

The total capacitance, C_{Total}, when considering all N layers and the air gap thus becomes:

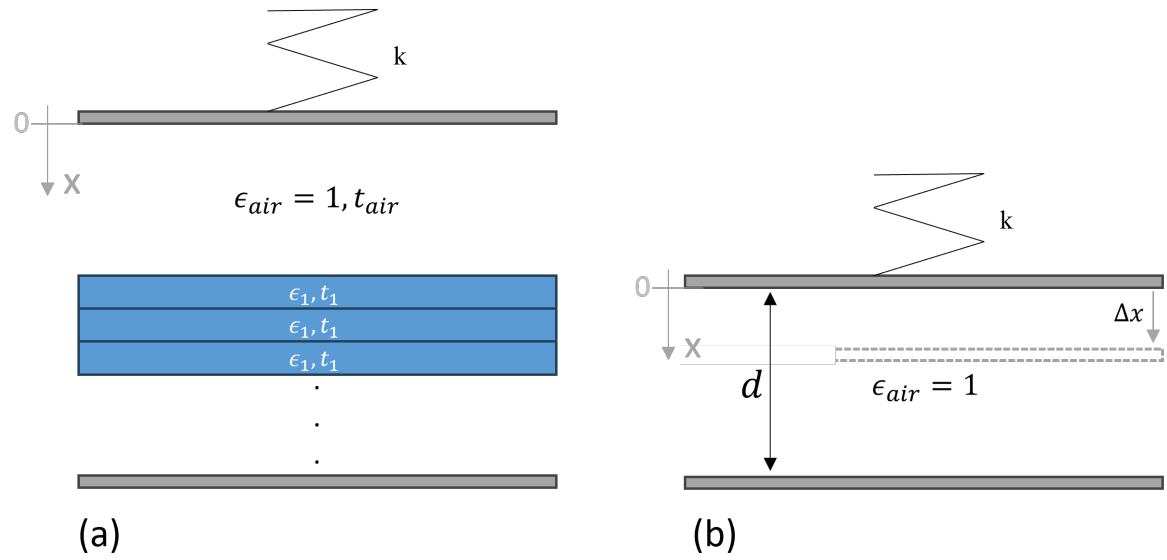

Figure 3.5: Cross section schematics of the analytic model used for pull-in voltage estimation Plate capacitor with a moveable top electrode and (a) multi-layered dielectrics, (b) equivalent device with air distance d. ϵ_i and t_i denote the relative permittivity and dielectric thickness respectively. d is defined in Equation 3.12 the geometric factor of the system, k is the equivalent spring constant of the system.

$$C_{\text{Total}} = \frac{1}{\sum_{i=1}^{N} \frac{1}{C_i} + \frac{1}{C_{\text{air}}}} \tag{3.10}$$

where:

- C_i is the capacitance of the i^{th} layer, and
- C_{air} is the capacitance of the air gap.

The voltage across the system in terms of the charge stored and the total capacitance, can then be computed as follows:

$$V = \frac{Q}{\epsilon_0 A}\left(\sum_{i=1}^{N} \frac{t_i}{\epsilon_i} + \frac{t_a - x}{1}\right) = \frac{Q}{\epsilon_0 A}(d - x) \tag{3.11}$$

where:

- Q is the charge stored,
- x is the displacement of the layers due to applied voltage, and
- d is a geometric factor, defined in 3.12
- t_i is the thickness of the i^{th} layer, and
- t_a is the initial thickness of the air gap.

Introduced by Saucedo-Flores et al. [192] d can be defined as the geometric factor of the system, essentially representing the weighted sum of the thicknesses of all layers and the initial air gap :

$$d = \sum_{i=1}^{N} \frac{t_i}{\epsilon_i} + t_a \tag{3.12}$$

This substitution allows the lumping of the multilayered model into a simpler device (see Figure 3.5b), where the dielectric between the electrodes only consists of air.

The pull-in condition is obtained when both mechanical and electrostatic forces are in equilibrium (Equation 3.13), and when the equivalent stiffness (Equation 3.14) of the complete system becomes zero - any further displacement of the microbridge will not result in a restoring movement.

$$F_{\text{total}} = \frac{\partial E_{\text{el}}}{\partial x} - \frac{\partial E_m}{\partial x} = 0 \tag{3.13}$$

$$\frac{\partial F_{\text{total}}}{\partial x} = \frac{\partial}{\partial x}(F_{el} - F_m) = 0 \tag{3.14}$$

where:

- E_{el} and E_m are the electrostatic and mechanical energy, respectively.

Continuing, the energies are defined as:

$$E_{el} = \frac{1}{2}CV^2 \tag{3.15}$$

$$E_m = \frac{1}{2}kx^2 \tag{3.16}$$

where:

- C is the capacity.
- V is the applied voltage.
- k is the microbridge equivalent spring constant.
- x is the displacement of the microbridge.

Using equation 3.13, we derive:

$$\begin{aligned} F_{\text{total}} &= \frac{\partial E_{el}}{\partial x} - \frac{\partial E_m}{\partial x} \\ &= \frac{\partial}{\partial x}\left(\frac{1}{2}CV^2\right) - \frac{\partial}{\partial x}\left(\frac{1}{2}kx^2\right) \\ &= \frac{\partial}{\partial x}\left(\frac{1}{2}\frac{A\epsilon_0\epsilon_1}{d-x}V^2\right) - kx \\ &= \frac{\epsilon_0\epsilon_1 A}{2(d-x)^2}V^2 - kx = 0 \end{aligned} \tag{3.17}$$

From equation 3.17, the equilibrium voltage for a given spring constant is:

$$V_{eq} = \sqrt{kx\frac{2(d-x)^2}{\epsilon_0\epsilon_1 A}} \tag{3.18}$$

Pull-in is reached when the equivalent stiffness of the complete systems becomes zero. Thus, replacing the voltage with the equilibrium voltage from equation 3.18 and computing the equivalent stiffness, the critical displacement at which pull-in occurs is:

$$\begin{aligned} \frac{\partial F_{\text{total}}}{\partial x} &= \frac{\partial}{\partial x}\left(\frac{\epsilon_0\epsilon_1 A}{2(d-x)^2}V^2 - kx\right) \\ &= -k + \frac{AV^2\epsilon_0\epsilon_1}{(d-x)^3} = 0 \end{aligned} \tag{3.19}$$

Inserting $V = V_{eq}$ into equation 3.19, we get:

$$-k + \frac{2kx}{d-x} = 0 \tag{3.20}$$

Solving for x from equation 3.20, the pull-in displacement is:

$$\boxed{x_{PI} = \frac{d}{3}} \tag{3.21}$$

Finally, the pull-in voltage can be calculated as:

$$\boxed{V_{PI} = \sqrt{\frac{8kd^3}{27\epsilon_0\epsilon_1 A}}} \tag{3.22}$$

As for the equivalent spring constant of the microbridge, a clamped-clamped beam model with a distributed uniform load is used:

$$k_0 = 32EW\left(\frac{T}{L}\right)^3 \tag{3.23}$$

where:

- k_0 is the spring constant for the fundamental mode of vibration.
- E is the modulus of elasticity of the material.
- W is the width of the microbridge.
- T is the thickness of the microbridge.
- L is the length of the microbridge.

The effect of the reduced area due to the holes on the electrostatic energy is said to be negligible when the diameter of the holes is less than 3-4 times the vertical gap between membrane and bottom electrode. This is due to an increased fringing field effect that approximately compensates the loss of area [193]. However, the holes do influence the stiffness of the beam.

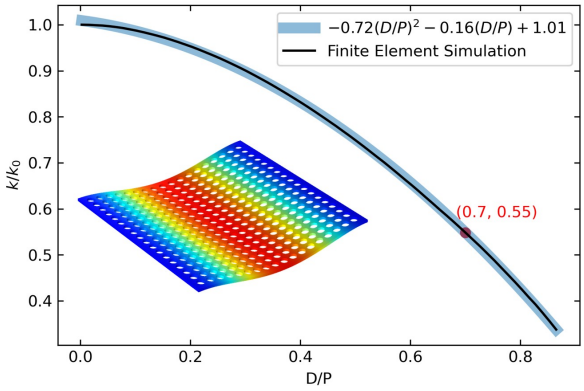

Figure 3.6: Period-normalized hole diameter vs. equivalent spring constant. COMSOL Metaphysics

Finite elements analysis (COMSOL) is used to determine the relation between the reduction of the equivalent spring constant with an increased diameter-to-period ratio. For instance, an amorphous silicon (E = 80 GPA) microbridge with holes of 280 nm diameter and 400 nm period, with a microbridge length of $7\mu m$ leads to a reduction by 45%.

$$k \approx k_0 \times 0.55 \tag{3.24}$$

The period-normalized hole diameter D/P versus the equivalent spring constant k normalized by the one computed without the holes k_0 for a beam of the given geometric and material properties is plotted in Figure 3.6.

3.3. Mechanical Response Time

The mechanical response time can be estimated by modeling the mechanical system as an undamped harmonic oscillator. Equation 3.25 describes the energy conservation, more precisely equating the gained kinetic energy as well as the remaining potential energy with the stored potential spring energy.

$$\frac{1}{2}m\dot{x}^2 + \frac{1}{2}kx^2 = \frac{1}{2}k(\Delta x)^2 \tag{3.25}$$

where:

- m is the mass of the microbridge.
- x is the instantaneous displacement.
- k is the equivalent spring constant.
- Δx is the maximum displacement of the microbridge.

The velocity is given by:

$$\dot{x} = \sqrt{\frac{k((\Delta x)^2 - x^2)}{m}} \tag{3.26}$$

Since: $dx/dt = \dot{x}$ we can rewrite: $dt = dx/\dot{x}$ and hence the total time needed would be:

$$t_{po} = \int_0^{\mathrm{d}} \frac{dx}{\dot{x}} = \int_0^{\mathrm{d}} \frac{dx}{\sqrt{\frac{k((\Delta x)^2 - x^2)}{m}}} = \frac{\pi}{2}\sqrt{\frac{m}{k}} = \frac{1}{4f} \tag{3.27}$$

where:

- f is the eigenfrequency of the MEMS device

The outcome is logical, given that an undamped mass-spring system exhibits sinusoidal velocity, and the solution provided corresponds to one-fourth of a complete cycle (from rest to maximum displacement).

4

Static Prototype

Following the conceptual framework for a MEMS-based tunable metasurface outlined in section 1.1, an initial static prototype is fabricated. This prototype does not fully implement the dynamic tunability envisioned but serves as a preliminary validation of the principles discussed. It is specifically designed to demonstrate the feasibility of altering surface reflectivity through silicon-based structures. The prototype consists of areas with amorphous silicon (aSi) nanopillars situated on top of an approximated 100 nm aSi layer, representing the full actuated state of the membrane, and areas with only said aSi layer, representing the idle state. The geometric dimensions of these nanopillars—specifically, a period of 608 nm, a diameter of 300 nm, and a height of 412 nm—were established through a series of trial-and-error RCWA simulations. While these dimensions are not globally optimized, they were specifically tailored to optimize the 0th order reflection. The device was designed for measurements exclusively at normal incidence; therefore, higher-order effects is deemed irrelevant for this study.

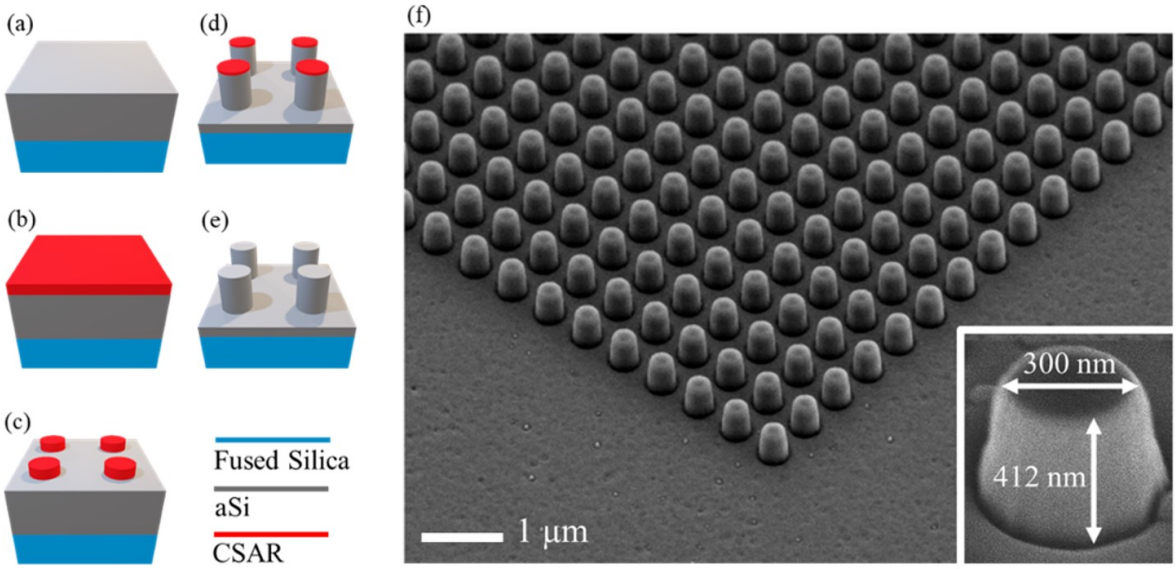

Figure 4.1: Nanofabrication of large-scale aSi nanopillar arrays. (a) - (d): Visualization of nanofabrication process flow showing 4 pillars of the periodic nanopillar array. (a) DC sputtering of 500 nm aSi onto a fused silica substrate, followed by (b) e-beam resist CSAR spin coating of 150 nm, and (c) e-beam exposure and development in amyl acetate. (d) Reactive ion etching of aSi to create the nanopillars, and finally (e) resist removal using oxygen plasma. (f) Tilted (45°) Scanning Electron Microscope (SEM) recording showing a periodic array of nanopillars as well as the remaining surrounding silicon. Inset: close-up SEM recording of a single nanopillar; Geometry: period = 608 nm, diameter = 300 nm, height = 412 nm.

Figure 4.1 details the nanofabrication process employed to create these arrays of aSi nanopillars. Initially, Direct Current (DC) sputtering is used to deposit an aSi layer onto the fused silica substrate

(Figure 4.1a), providing the base for the subsequent nanopillar structures. This is followed by spin coating a 150 nm layer of e-beam resist CSAR (Figure 4.1b), preparing the surface for detailed patterning. Electron beam (e-beam) exposure comes next (Figure 4.1c), where the resist is developed in amyl acetate to delineate the areas for nanopillar etching. Reactive ion etching (Figure 4.1d) is then executed to sculpt the nanopillars from the aSi layer. Finally, any remaining resist is eliminated using oxygen plasma (Figure 4.1e). A 45° tilted Scanning Electron Microscope (SEM) image (Figure 4.1f) confirms the successful fabrication, showcasing the periodic array of nanopillars. A close-up SEM inset provides further detail on the geometric dimensions of a single nanopillar.
To visually assess the absorption characteristics as a decorative element, nanopillar arrays were combined to form a binary image of a zebra, where the dark pixels are created through the absorptive metasurface. Figure 4.2 shows the resulting optical microscope image. This picture clearly qualitatively validates the expected blackness of the nano-structured silicon, but also hints at the possibility that a tunable surface might shows show some very visually appealing characteristics.

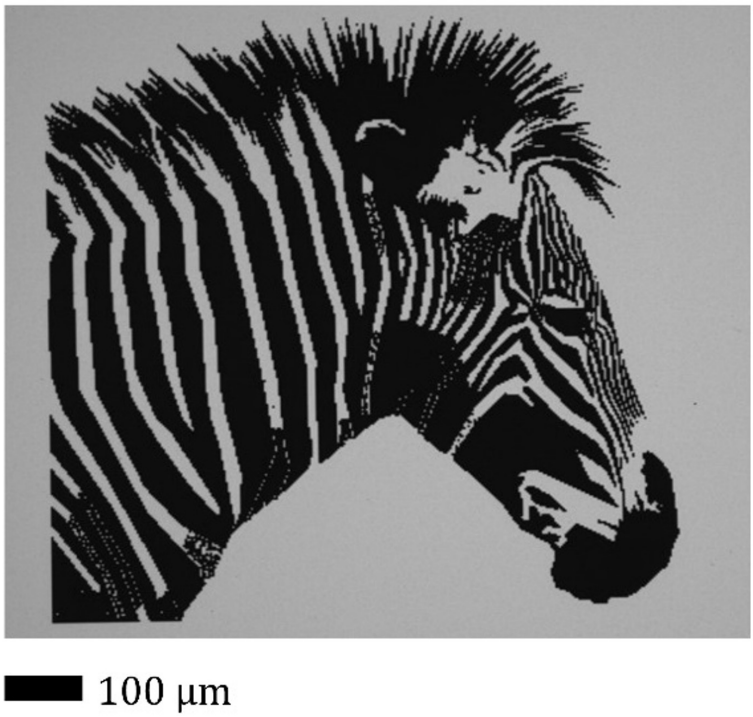

Figure 4.2: Optical microscope image (50x) of the fabricated sample showing a zebra, where the dark regions are due to light absorption by aSi nanopillar arrays, and the bright regions due to the high reflection of the unstructured, flat silicon surface.

To gain more quantitative insight, the reflection spectra from the nanostructured and flat regions are measured using an inverted microscope setup, consisting of a white light source and a spectrometer. The spectra are depicted in Figure 4.3. It validates the qualitative assessment, showcasing a 1:50 contrast ratio between both states, with very low reflection for the structured sample. The experimental measurments show to be in good agreement with the expected simulated outcome, validating the RCWA code used. The slight differences between simulated and measured spectra can arise from many aspects, such as the slight slope of the fabricated pillars, a slight deviation between material properties in the simulation and fabricated device, and lastly some geometric differences. It needs to be noted, though, that the collected light comes from the direct reflection within a limited solid angle as captured by the optical microscope, rather than an integration sphere which would encompass a broader range of scattering angles. This methodological choice, focusing on direct reflection, is particularly relevant for comparing the simulated reflection spectra which only simulates the normal reflection (0th order) and the experimental result.

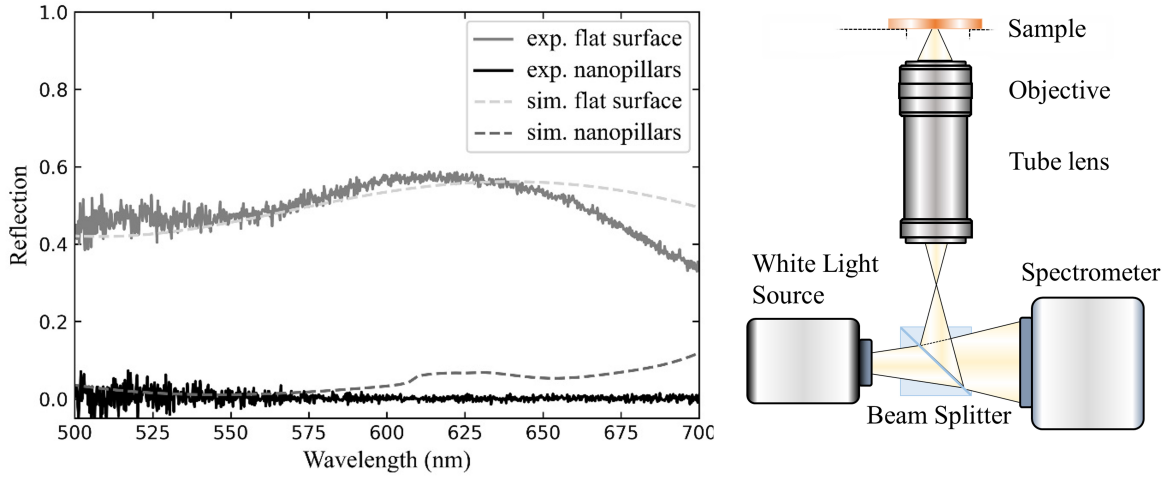

Figure 4.3: Optical microscope image (50x) of the fabricated sample showing a zebra, where the dark regions are due to light absorption by aSi nanopillar arrays, and the bright regions due to the high reflection of the unstructured, flat silicon surface.

In summary, broad spectral absorption range in the visible spectrum is demonstrated through the nanostructuring of amorphous silicon (aSi), resulting in an absorptive metasurface, as well as decent reflection from the flat surfaces. This result validates the core idea of the MEMS tunable metasurface investigated.

5

Proof-of-concept: Tunable Metasurface Reflectivity Modulator in the Visible Spectrum

Disclaimer: Major parts of the following chapter have been adapted from the published paper entitled "Broadband Mechanically Tunable Metasurface Reflectivity Modulator in the Visible Spectrum"[194].

Authors List: Dorian Herle, Olivier J.F. Martin, L. Guillermo Villanueva, Niels Quack

Doctoral candidate's contribution: The doctoral candidate presented the initial idea, performed initial optical simulations, envisioned the hereafter presented process flow, and fabricated the whole device.

Having successfully demonstrated that nanostructuring a surface can result in enhanced light absorption—yielding dark optical states when such absorption is optimized for the visible spectrum—the subsequent chapter delves into the next phase of development. Specifically, it aims to showcase a MEMS-actuated switch capable of dynamically transitioning between a nanostructured state and a flat state. This opens up the use of such elements for dynamic light control as needed on the pixel level of reflective displays.

5.1. Working Principle

The MEMS-based tunable metasurface consists of a silicon membrane featuring a rectangular array of holes. Each hole in the membrane hosts a fixed nano-disk.

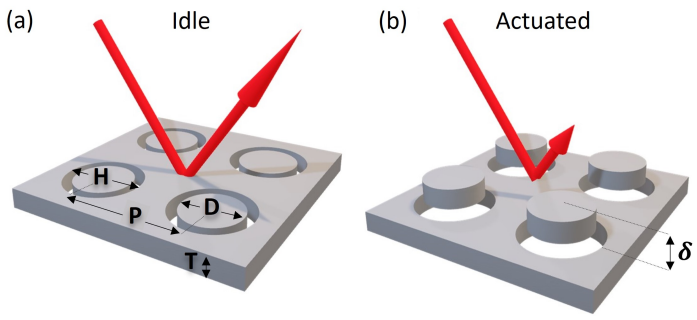

Figure 5.1: Operating principle of the tunable metasurface modulator: (a) Idle state yields high reflectivity; (b) Actuated state, with vertical membrane displacement of δ, results in low reflectivity due to Mie resonance.

While the initial concept showed pillars, the choice of using disks instead of pillars solely resides in facilitating the fabrication but does not underpin the underlying physics. Electrostatic actuation enables the vertical displacement of the membrane, allowing for a transition between two optical states: a reflective state and an absorptive state. When the membrane and the nano-disks are aligned at their top surfaces, a highly reflective state is achieved. On the other hand, when the membrane is displaced vertically by electrostatic forces, the Mie resonance-induced absorption in the nano-disks is tuned, resulting in reduced reflectivity of the surface. This modulation is depicted in Figure 5.1. The exact geometric dimensions are obtained by RCWA optimizations and summarized in table 5.1

Symbol	Description	Value (nm)
D	Disk diameter	300
P	Period of disk array	400
H	Diameter of hole in membrane	300
T	Thickness of membrane and disk	100
δ	Membrane vertical displacement	0 (idle) – 150 (actuated)

Table 5.1: Symbol Descriptions and Values

The design of the MEMS-actuated metasurface consists of a perforated suspended microbridge in which each perforation hosts a nano-pillar. The pillar itself consists of an aSi nano-disk that is supported by a silicon oxide stand. The device is schematically represented in Figure 5.2. When a voltage is applied between the membrane and substrate, the membrane is continuously displaced through electrostatic attraction. For this prototype, the oxide stands are chosen to be 150 nm in height, allowing the membrane to travel this distance. The device is operated in pull-in. The pull-in voltage is analytically approximated to be on the order of 14-16 V. The method by which the pull-in voltage is derived is described in 3.2.

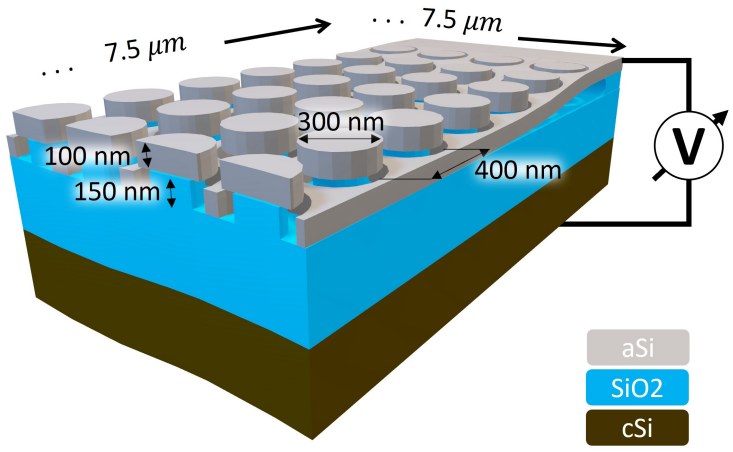

Figure 5.2: MEMS Design. Oxide-supported disks and membrane. Electrostatic actuation of the membrane by the application of a potential difference between the membrane and the supporting silicon, whereas oxide acts as a dielectric spacer. Disk height as well as membrane thickness is chosen to be 100 nm, with an oxide stand of 150 nm and a dielectric oxide spacer of 350 nm.

5.2. Optics

In Figure 5.3a, the simulated wavelength-dependent reflection, transmission, and absorption of the system are depicted. The spectral-averaged absorption in the disks and membrane is also calculated separately by integrating and averaging the absorption in each of the system's components from 400 to 650 nm. As the membrane displacement increases, a significant rise in the spectral-averaged absorption in the nanodisks is observed, as shown in Figure 5.3b. This leads to a broadband decrease in reflection from the metasurface.

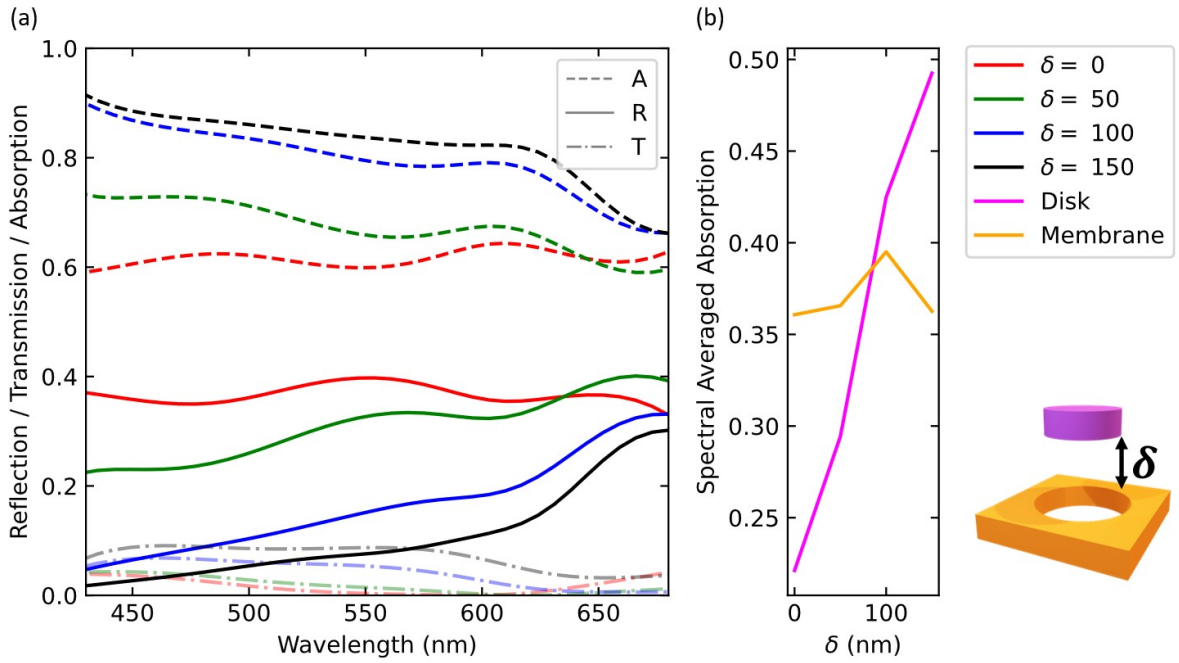

Figure 5.3: Influence of the membrane position on the optical spectral response. (a) 0th-order reflection and overall absorption computed for different membrane positions. A vertical membrane displacement from 0 to 150 nm results in a reflection reduction in the spectral range from 400-650 nm. A: Absorption, R: Reflection, T: Transmission. (b) Spectrally averaged absorption for the disk or the membrane. The disk acts as the active element with a continuous increase in absorption as the membrane is displaced.

To provide additional insights into the origin of the broadband spectral response, the coupling between the membrane and the disks is studied in further detail. Finite element simulations are first performed in Figure 5.4 to extract the absorption inside the disks. Three scenarios are considered: disks in the air without any surrounding membrane, disks surrounded by a well-aligned membrane, and disks placed at a vertical distance δ=150 nm above the membrane. As depicted in Figure 5.4, disks in air and disks offset by a distance of 150 nm above the membrane exhibit similar absorption spectra. The discrepancy between both curves, starting mostly from 500 nm, can be attributed to the coupling between disks and membrane. This coupling is wavelength-dependent, thus explaining the non-constant offset. For disks that are inside the membrane, however, the absorption within the disks decreases. It is hypothesized that upon the insertion of the disks into the membrane, the membrane serves as an effective medium with a high refractive index. This prevents an effective excitation of the Mie resonances in the disks, leading to the absence of resonant absorption when the disks are situated within the membrane.

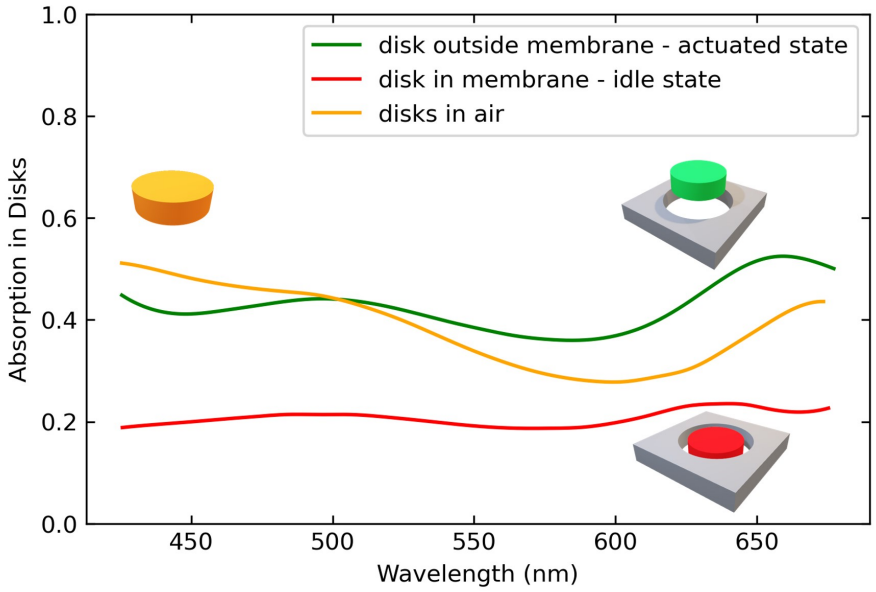

Figure 5.4: Absorption spectra inside the array of disks freestanding in air, placed in the membrane, and out of the membrane with an offset δ = 150 nm. The parameters for the disks and membrane are the same as in Table 5.1.

To study this effect, the field that an individual disk scatters is decomposed into vector spherical harmonics [195]. The underlying principle involves calculating the far-field via the surface integral equation method for isolated structures [196], [197]. This calculation is performed at points on a sphere with a radius of $10\,\mu$m. Subsequently, this field is decomposed into a series of vector spherical harmonic functions. Through the known amplitudes of these functions, the scattering cross section attributed to each multipole is deduced [195], [198]. Data for the refractive index of aSi are sourced from Pierce et al. [199]. In Figure 5.5a, b, the scattering cross-sections and the multipolar components are displayed for an isolated disk of the same size as shown in Figure 5.3. This disk is placed inside a medium with a refractive index of $n = 1$ (Figure 5.5a) and $n = 2$ (Figure 5.5b). The first four multipoles are found to represent the full scattering cross section in the multipolar analysis adequately. Individual resonances are broadened as the refractive index of the host medium increases. For example, the magnetic dipole of the disk in a medium with a refractive index of 2 (Figure 5.5b) is observed to have a wider resonance than the disk in a medium with a refractive index of 1 (Figure 5.5a). A similar behavior is shown by the electric dipole. Broad higher-order multipoles, such as the electric and magnetic quadrupoles, are seen to redshift to the visible spectrum. This resonance broadening leads to a decrease in field enhancement inside the structure [200].In Figure 5.5c, the absorption cross-section of an isolated disk is studied. The refractive index of the surrounding medium is varied over a broad range to mimic the gradual change of the effective refractive index of the surrounding medium as disks enter the membrane. A decline in absorption cross-section is observed (Figure 5.5c). However, the absorption barely changes for the short wavelength part of the spectrum, specifically around $400\,$nm as shown in Figure 5.5c. This minimal change is believed to arise from the fact that the air gap between the membrane and the disks is not considered. To account for such gap, the absorption cross section for an isolated disk in an air void, submerged in a medium with different refractive indices, is presented in Figure 5.5d. In this figure, the air spacing thickness corresponds to the disk-membrane distance of the fabricated device ($\sim 50\,$nm). It is evident from Figure 5.5d that absorption across the entire range of interest $(400 - 700\,\text{nm})$ decreases as the refractive index of the surrounding medium increases. Conversely, one can summarize that in the idle state, the membrane is perceived to act as a high refractive index host medium, causing a reduction in disk absorption. By actuating the membrane position, the host medium of the disk is modified, affecting the light absorption within the disks.

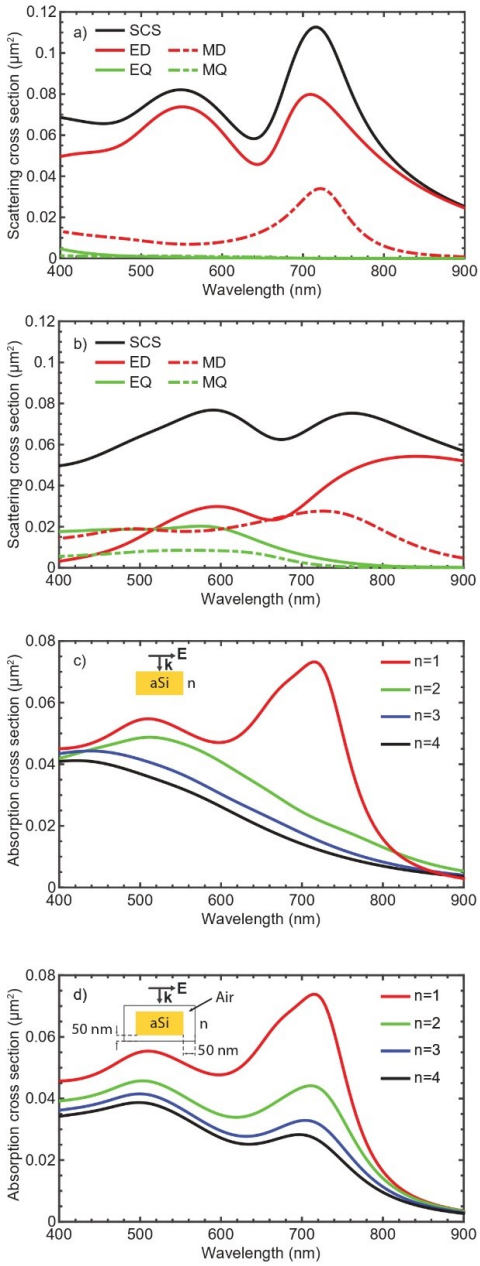

Figure 5.5: Spectral response of an isolated nano-disk surrounded by a medium with different refractive indices. Scattering cross-section and its multipolar decomposition for an isolated disk in backgrounds (a) $n = 1$ (a) and (b) $n = 2$. (c) Absorption for the isolated disks in different background media from $n = 1$ to $n = 4$. (d) Absorption for an isolated disk placed in an air shell, which is further placed in a medium with the refractive index $n = 1$ to $n = 4$. A resonant behavior is observed for a disk in air $(n = 1)$, while the resonances broaden for surrounding media with increased refractive indices. Abbreviations: SCS = Scattering Cross Section, ED = Electric Dipole, EQ = Electric Quadrupole, MD = Magnetic Dipole, MQ = Magnetic Quadrupole .

5.3. Fabrication

A surface micromachining process is employed for the fabrication of the MEMS tunable metasurface. A layer of 100 nm of aSi is sputtered onto a wet-oxidized crystalline silicon wafer with 500 nm SiO_2 on its surface using a Pfeiffer SPIDER 600, 800 W, 29 sccm O_2, DC source at room temperature. Surface activation is performed in Plasma Oxygen (500 W, Tepla GiGAbatch) for 5 minutes, followed by a 5-minute dehydration bake at 180° C. A thin layer (150 nm) of AR-P 6200 (CSAR 62) e-beam resist is spin-coated. This specific e-beam resist is chosen for its high contrast and etch

selectivity.

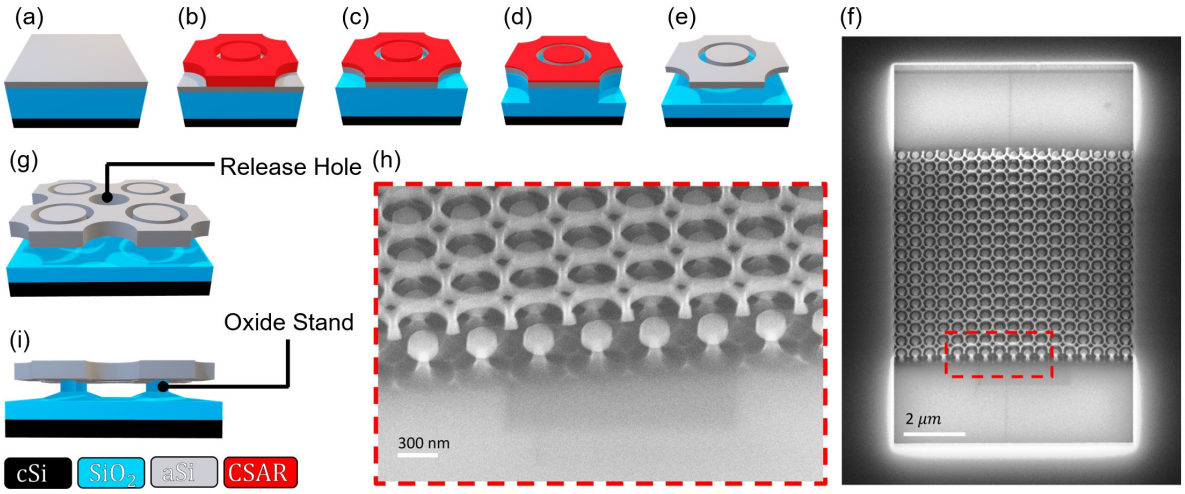

Figure 5.6: Fabrication of a tunable metasurface. (a-e) Outline of the process flow showing the unit cell of the periodic pattern: (a) deposition of 500 nm of SiO_2 and 80 nm of amorphous silicon (aSi) onto crystalline silicon (cSi) wafer, (b) electron-beam lithography using positive resist CSAR 64 of 150 nm thickness, (c) reactive ion etching of the aSi layer, (d) followed by approximately 100 nm reactive ion etching into the SiO_2, (e) and carefully timed hydrofluoric (HF) vapor phase isotropic SiO_2 etching to release the membrane. (g) Visualization of the release holes in the membrane, which enable increased access points for the HF vapor to etch the sacrificial SiO_2 layer, thus releasing the membrane faster than a complete under-etch of the disk. (i) Visualization of the remaining oxide stand after the release step, which keeps the disks in place. (h) and (i) SEM images of the fabricated sample, showcasing (i) a single pixel consisting of a clamped-clamped membrane as well as (h) a close-up showing the individual aSi disks supported by the remaining oxide posts, and the membrane with its holes, slightly buckled upwards (80 nm max) due to residual stress (thermal mismatch during deposition).

A pre-exposure bake at 180°C for 5 minutes is conducted. Electron-beam lithography is then utilized with a Raith EBPG5000 to define the structure. A dose of 270 µC/cm^2 (100 keV) is applied, and proximity-effect correction is engaged to optimize uniformity across the wafer. A 1-minute development in amyl-acetate is followed by a 1-minute rinse in a 90:10 MiBK: IPA solution and drying is performed with nitrogen. Pattern definition of the aSi layer is accomplished using inductively coupled plasma (ICP) with an Alcatel AMS 200 SE. A laser-based (=690 nm) end-point detection system is used for precise etch termination upon reaching the underlying SiO_2. A vertical SiO_2 ICP etch is subsequently conducted using a mixture of C_4F_8/H_2/He gases. Release holes with diameters of 100 nm are chosen to be below the cut-off hole diameter for the smallest wavelength in the spectrum of interest. Isotropic etching of the oxide is performed using HF vapor (SPTS uEtch), comprising an anhydrous HF and ethanol (C_2H_5OH) gas phase at reduced pressure. This allows for stiction-free release of MEMS without pollutant generation. An etch rate of 0.12 nm/s is consistently observed, making the release a time-controlled process once calibrated. High voltage (10 kV) SEM images are captured at specific etching times to measure the etch-front accurately, enabling precise oxide etch-rate measurements. The entire fabrication process is illustrated schematically in Figure 5.6a-e. The release holes diameters of 100 nm are chosen to be below the cut-off hole diameter for the smallest wavelength in the spectrum of interest, thus they do not noticeably affect the optical performance, as can be observed in Figure 5.7.

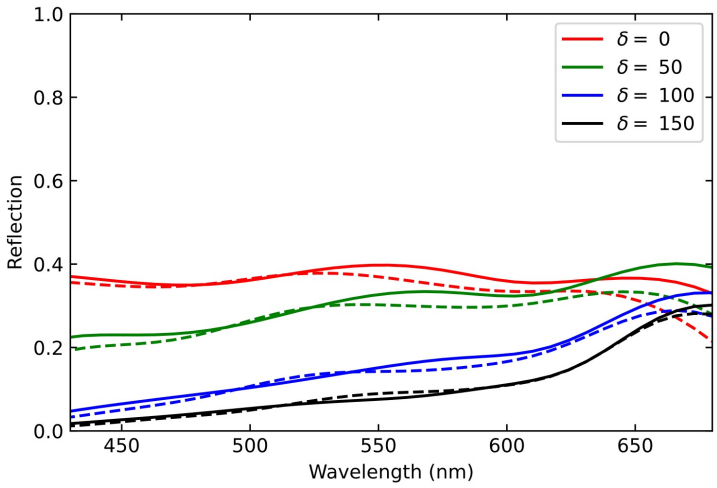

Figure 5.7: Influence of the release holes on the device reflection. Reflection spectra $(400 - 700\,\text{nm})$ are simulated for a membrane without release holes (solid lines) and with 100 nm diameter release holes (dashed lines), showing very little influence on the spectral response.

Initial devices were designed by essentially etching away rings to form the disk and release holes to expedite the membrane release over the disk under-etch. However, this approach leads to an uneven material distribution of the membrane, with potentially very thin sections along the diagonal as displayed in Figure 5.8. Such distribution can lead to enhanced localized stress concentrations in these areas, leading to potential ripping of the membrane, and can make those areas more susceptible to over-development. To even out the stress distribution, the release hole is reshaped such that the membrane essentially consists of intertwined rings as displayed with the orange-dotted line in Figure 5.8. This allows for equal material distribution in all directions, leading to a very uniform membrane mesh.

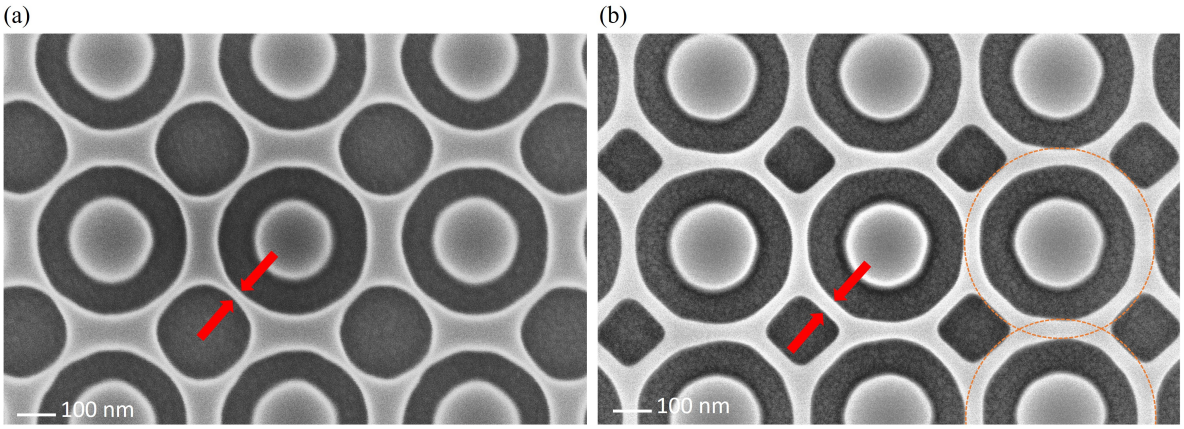

Figure 5.8: Influence of release hole shape on membrane mesh uniformity. (a) A circular release hole leads to very thin sections along a diagonal (red arrows) versus thicker sections along the horizon. (b) Membrane mesh created by intertwined rings (visualized by an orange dotted line) offers a way to create a uniform mesh and thus reduce localized stress peaks.

Figure 5.9 shows in Figure 5.9a the discussed failure mode where an over-development of the thin structures of the membrane leads to an unconnected membrane mesh. Figure 5.9b shows an over-etch during the HV vapor MEMS release step. This step needs to be calibrated to a few tens of nanometer precision. High-voltage SEM images are very good for the calibration process as it's possible to see through the membrane at this sample.

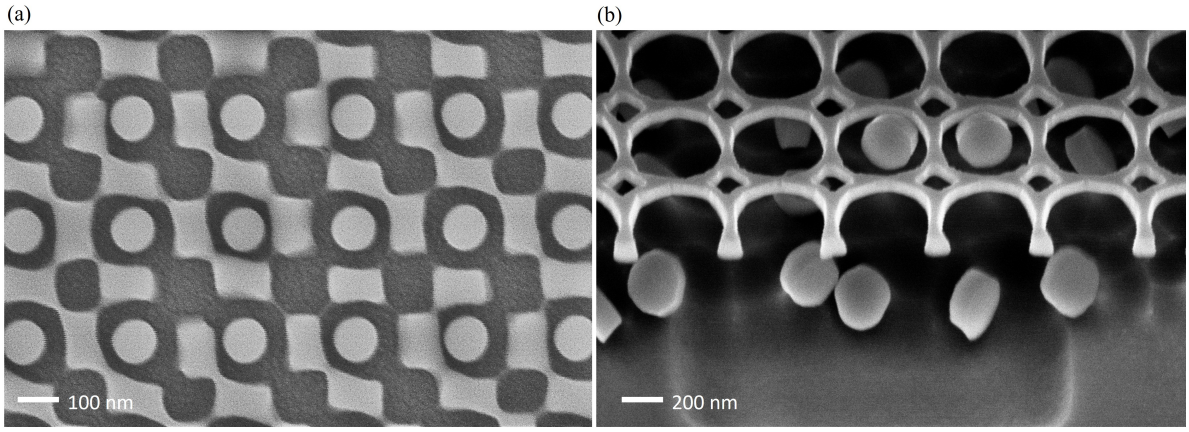

Figure 5.9: Exemplary fabrication failures. (a) Over-developed thin structures of membrane. (b) Over-etched during HF Vapor MEMS release

5.4. Characterization

To demonstrate the suitability of the tunable metasurface for display applications, a segmented display composed of 42×9 individual metasurface pixels is constructed. The 42×9 metasurface pixels are released and fabricated as described previously. Electrical connection to the device layer surface is established for only a subset of pixels, while the remaining pixels are insulated from the device layer surface by electrical insulation trenches. The subset of electrically connected pixels is selected to display the EPFL logo upon actuation, as evidenced in the microscope recording of Figure 5.10a. The array is shown in the idle state and in the actuated state, where the pixels are actuated by applying an actuation voltage between the device layer surface and the substrate layer. Upon actuation, the segmented pixels of the EPFL logo switch to a darker absorptive state.

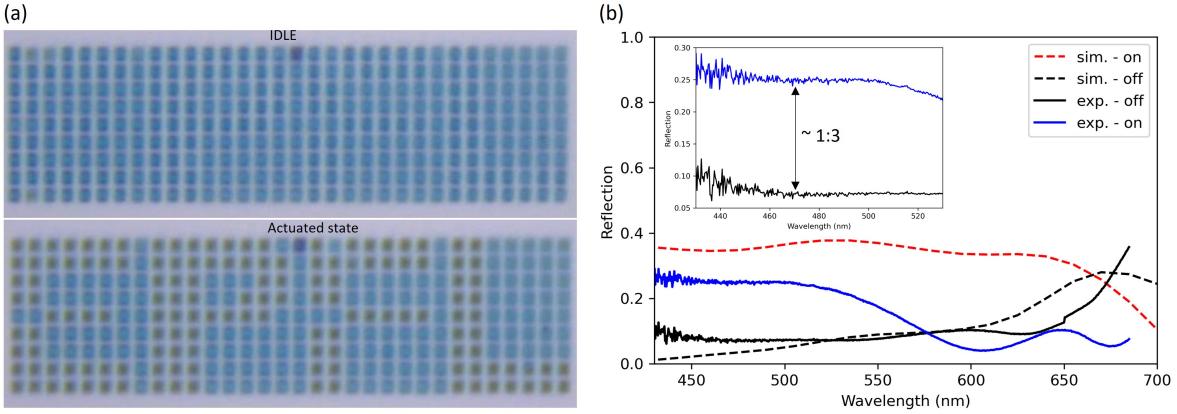

Figure 5.10: Demonstration of the modulation capability showcasing the EPFL logo when in an actuated state. (a) Optical microscope image showing a segmented display forming the EPFL logo when switched from the idle to the actuated states. The pixels outside the EPFL logo are electrically disconnected. (b) Measured reflection spectra in the optically idle and actuated states corresponding to applied 0 and 70 V, respectively. The average CR in the spectral range from 400 to 530 nm is $1:3$.

Stiction is not observed, attributed to reduced contact area resulting from spikes of sacrificial SiO_2, as seen in Figure 5.6h. The spectral response and CR are experimentally determined through a spectrometer setup, using a silver mirror with almost perfect reflectance as reference [201]. The measured reflection spectra are displayed in Figure 5.10b. An average CR of 1:3 in the range of 400 to 530 nmis measured. Discrepancies between the measured and simulated spectra in the idle state are attributed to geometric differences induced by the manufacturing process. Notably,

the membrane is buckled upwards by residual stresses in the idle state. As discussed in further detail in Appendix A.5, this geometry leads to destructive interference in the visible, resulting in a reflection dip between 550 and 700 nm. The membrane can be approximated as an infinite slab of an equivalent refractive index (air holes and aSi). Using this simplified model, it can be seen that for the given membrane thickness destructive interference occurs within the wavelength range of approximately 500 to 700 nm, agreeing with the measured spectra. The switching time is measured to be on the order of 20 ms (see Figure 5.11), by using laser Doppler velocimetry (LDV) and integrating the result to obtain the membrane displacement versus time. An actuation voltage of 33 V is applied, and a displacement of approximately 140 nm is measured. The actuation voltage is purposefully placed beyond the pull-in (16V) to ensure a complete movement of the membrane.

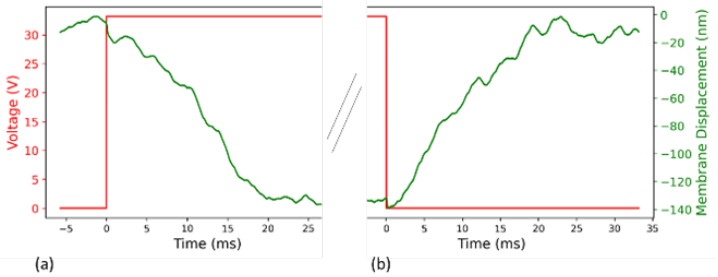

Figure 5.11: LDV switching time measurement. A step input of 33 Volts induces an averaged membrane displacement of approx. 100 nm. Switching time for both on (a) and off (b) switching 20 ms. This slow switching time is due to the high viscosity of the air trapped beneath the membrane as well as the high electrical resistivity of aSi, as discussed in the manuscript.

In terms of mechanical aspects, the viscosity of the air trapped beneath the membrane significantly influences the device's performance. The relatively low viscosity of air plays a crucial role in the device's dynamics, particularly in the damping of the membrane's movement. This effect is a factor in the observed switching. In terms of electric behavior, the device can be regarded as analogous to an RC circuit, wherein the resistance is proportional to the material's resistivity and the distance between the probe and the pixel. MEMS devices capable of high-frequency modulation typically employ highly doped Si, which can exhibit resistivity as low as 0.001 Ohm · cm. In contrast, the prototype utilizes aSi with an approximate resistivity of 10 k Ohm · cm [202]. The experimental probe distance is also noted to be approximately 1 mm, a value expected to be significantly reduced in a wire-bonded device. The capacity can be approximated as a plate capacitor with a SiO_2 dielectric spacer of 500 nm and an area of about 1 mm^2. These values yield an RC time constant of a few tens of microseconds, which concurs well with the measured modulation frequency and switching time. Better optical performances and faster switching can be expected by changing the membrane material to more reflective and more conductive materials, such as aluminum. The switch-off time follows the same speed primarily due to the necessity for the MEMS capacitor to undergo discharge. Consequently, this temporal aspect will also exhibit a strong reliance on the inherent resistances imparted by the membrane material.

5.5. Conclusion

A MEMS-based tunable metasurface has been successfully developed, in which reflectance modulation is achieved through the relative displacement of a hole-patterned membrane and a stationary nano-disk array. The fabrication process incorporates surface micromachining with a single e-beam exposure, obviating the need for lithographic alignment through the selective removal of a sacrificial oxide layer. A maximum contrast ratio of 1:3 has been observed within the visible spectrum range of 400 to 530 nm, and a switching time of 20 ms has been measured. These results provide compelling evidence for the successful implementation of the initial concept as an actuatable MEMS tunable metasurface reflectance modulator.

6

Scale-up

This chapter aims to highlight and discuss the efforts made to find a scalable process flow. The process flow utilized in chapter 5 and outlined in Figure 5.6 is beneficial for an initial proof-of-concept due to its relative simplicity. However, there are a few drawbacks that make it less suitable for potential scaled-up production, needed to fabricate thousands of pixels for real-world monitors.

- The gap between the disk and membrane is defined by lithography. As discussed initially in section 1.1, a small gap is preferred to achieve both a high contrast ratio between the idle and actuated state and good idle state reflectivity. In the previous fabrication outlined in 5.3, e-beam lithography was used to achieve a gap of 50 nm. However, e-beam lithography is a sequential process and thus non-compatible with high-throughput, large-area patterning. Deep Ultra-Violet (DUV) lithography may be able to achieve openings of roughly 40 nm [203], but that is pushing the systems to the limit, using water-immersed objectives to maximize numerical aperture.
- The fabrication method restricts the flexibility of geometric parameters. This limitation exists both in the fact that the disk and membrane cannot have different thicknesses and in the fact that the membrane needs to be completely undercut faster than the disks to avoid their collapse. This puts certain geometric limitations in terms of the maximum mesh width of the membrane with respect to disk diameter. It prohibits the fabrication of smaller diameter-to-period ratios, which can yield structurally more durable membranes and altered optical responses.
- The current MEMS release step needs to be very carefully timed to avoid an over-etch of the supporting oxide stands below the disks. This makes the process more susceptible to process instabilities.

To achieve a truly scalable process-flow it is clear that self-alignment between pillars and membrane is needed due to the small gap sizes aimed for. As depicted in Figure 6.1 two suggestions are investigated: pillar and membrane-first process flows. Both venues share similar high-level process characteristics. Notably, a conformal sacrificial layer is utilized to define the gap between the membrane and the pillars. Delving into the specifics, the primary distinction between the two approaches centers on the initiation phase. The pillar-first method commences with the pillars, whereas the membrane-first approach initiates with a sacrificial layer-supported membrane (Figure 6.1a). Both process flows progress to the conformal sacrificial layer deposition (Figure 6.1b), which sets the gap's parameters. The subsequent steps in both methods, encompassing material depositions (Figure 6.1c), etch-back (Figure 6.1d) and sacrificial material release (Figure 6.1e), are relatively analogous but tailored to their respective starting points.

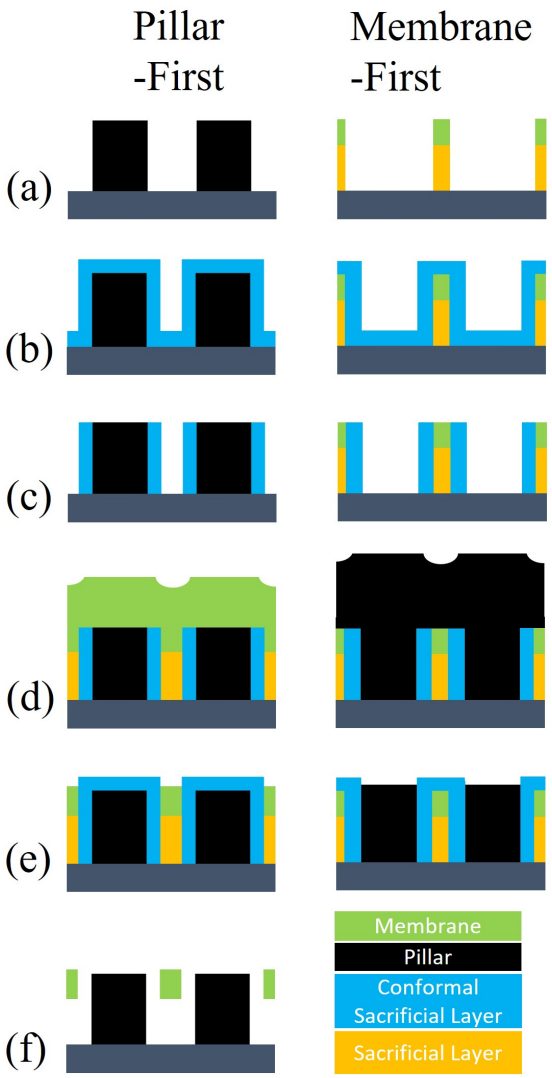

Figure 6.1: High-level process flow comparison between pillar- and membrane-first self-aligned process flow. (a) starting with pillars or sacrificial-layer supported membrane, (b) sacrificial layer deposition that defines the final gap between membrane and pillar, (c) directional etch of the sacrificial layer to remove bottom deposition and only keep on sidewalls, membrane/pillar material deposition, (d) etch-back (e) sacrificial material release

Both the membrane-first and pillar-first fabrication techniques hinge on a critical filling step for structural integrity and functional performance. In the membrane-first technique, pillar material is infused into the etched holes, while the pillar-first technique involves a two-step process. Firstly, a sacrificial material fills the spaces between the pillars, followed by the membrane material. To assess the quality and completeness of the fill, various deposition techniques were systematically evaluated using nanoscale trenches designed with a high aspect ratio of 2.5. This aspect ratio was chosen for its potential to represent a wide range of manufacturable geometries.
Figure 6.2 provides a graphical representation to supplement this evaluation. The figure delineates the distinct filling outcomes when using various deposition methods such as Plasma Enhanced Chemical Vapor Deposition (PECVD), Low-Pressure Chemical Vapor Deposition (LPCVD), sputtering, evaporation, and spin-coating. In particular, LPCVD aSi achieves high conformality, making it an ideal choice for achieving a seamless fill (See Fig. 6.2a). On the contrary, methods like Sputtered aSi (See Fig. 6.2b) and PECVD SiO_2 (See Fig. 6.2c) struggle with overhang buildup, limiting their filling capability. Spin-coated HSQ initially shows promise but ultimately falls short due to thermal stress-induced cracking during the baking process (See Fig. 6.2d). Meanwhile, Spin-coated PR succeeds in filling the trenches effectively without such issues (See Fig. 6.2e). Az 10 XT, AZ 1512,

and AZ ECI were tested, and all resulted in identical filling and planarization properties. Thermo-evaporated Perylene and Evaporated SiO_2 fall short in various aspects; the former fails to fill the trenches entirely (See Fig. 6.2f), and the latter encounters issues with overhangs that hinder further filling after an initial fill (See Fig. 6.2g).

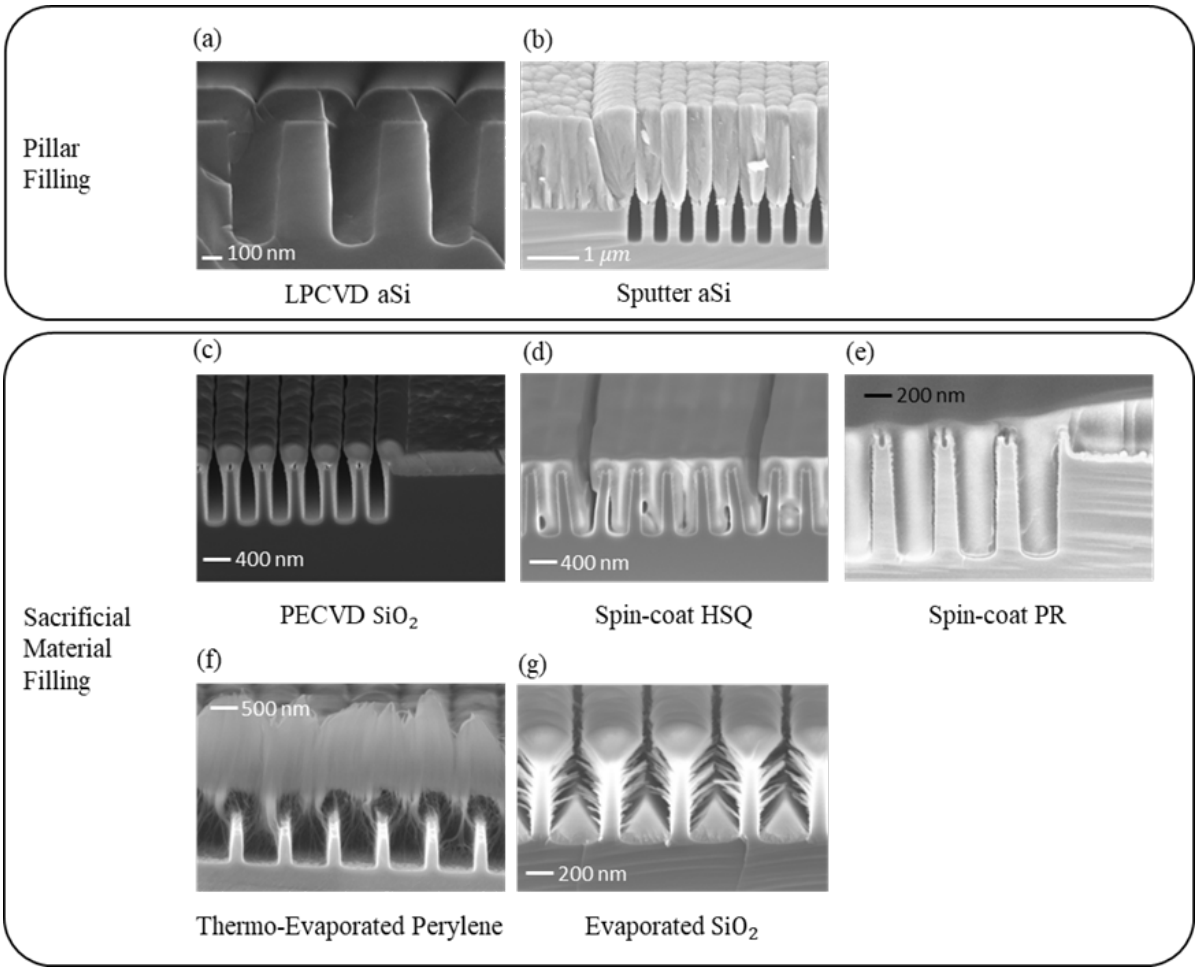

Figure 6.2: Deposition Method Comparison for Trench Filling: (a) LPCVD aSi, 500°C; (b) Sputtered aSi (Pfeiffer SPIDER 600, 800W, DC) ; (c) PECVD SiO_2 (PECVD OPT 100, 300C, 2% SiH_4/N_2, 1000 mTor); (d) Spin-coated HSQ (XR1541 006, 2000 rpm); (e) Spin-coated PR (AC ECI); (f) Thermo-evaporated Perylene; (g) Evaporated SiO_2.

While spin-coated PR could be used as a sacrificial structural material to be filled between the pillars, the membrane-first approach is chosen since it only requires 1 material filling step (the pillars) over at least two (structural sacrificial layer and membrane material) for the pillar-first method. In addition, the membrane-first approach allows for easier control of the membrane flatness. In the following another method to fill the holes of the membrane with aSi is presented.

6.1. Collimator Sputtering

Magnetron sputtering has emerged as the predominant method for thin film deposition [204]. Its significance is evident across industries that require superior coatings, either to introduce novel products or to enhance the quality of current ones. However, as depicted in Figure 6.3 when using sputtering to fill holes or trenches, overhang buildup at the entry points can lead to subsequent shadowing effects up to complete closure, essentially blocking further depositions at the bottom. A method to partially reduce these overhangs involves a physical filtration mechanism, a sieve-like construction, to selectively screen off-axis particles prior to impingement on the substrate. The goal is to reduce the angular dispersion of incoming sputtered particles, thus termed “collimator”[205]. The improvement in deposition directionality comes at the expense of lower sputtering rates since

the filtration process acts as a barrier to particle throughput.

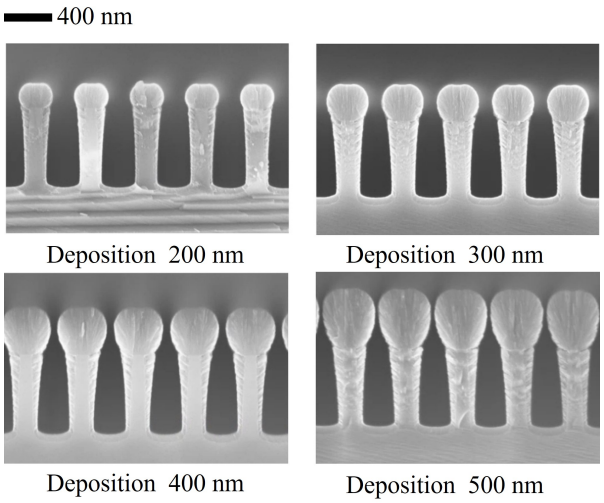

Figure 6.3: Cross-sections SEM images of silicon nano-trenches after amorphous silicon sputtering. Deposition thicknesses shown are 200 nm, 300 nm, 400 nm, and 500 nm. Overhang build-up due to the angular distribution of incoming particles creates a shadowing effect, essentially blocking further deposition into the trenches. DC Magnetron Sputtering, Pfeiffer SPIDER 600, 800 W, 29 sccm O2, DC source, room temperature

6.1.1. Analytic Model

An analytical model is introduced to assess the impact of collimator design on the sputtering process, slightly extending the foundational work by Jeffrey Cook[206]. Unlike Cook's model, the hereafter presented approach accounts for the spherical dispersion of material as it is ejected from the target. This additional consideration allows for a more accurate understanding of how the concentration of sputtered material per unit area on the wafer diminishes as it disperses. It's important to note, however, that the model is still a significant simplification of the actual process. It assumes that every point on the wafer will exhibit the same flux, and does not account for corner effects, non-uniform target erosion, re-sputtering or secondary sputtering due to energetic ions hitting the wafer, gas dynamics and mean-free paths, substrate temperature or rotating and moving substrates. Despite these simplifications, the model allows a first intuitive understanding of the main variable involved in collimator sputtering.

To compute the flux $F(r, z)$ of sputtered material impinging on the wafer center, the target surface is visualized as a collection of infinitesimal rings. It is stipulated, that for every minuscule point on these rings, material disperses following a cosine distribution, signifying maximum deposition directly below the sputtering point with decreasing intensity off-axis based on the cosine law. As this material travels, it spreads hemispherically, causing the density of arriving material at any point on the wafer to decrease, being inversely proportional to the square of its distance from the emission source. The total amount of particles reaching the center of the wafer after being emitted is computed by integrating all these concentric rings. The integration accounts for the cosine distribution and the geometric hemispherical dispersion, as detailed in Figure 6.4.

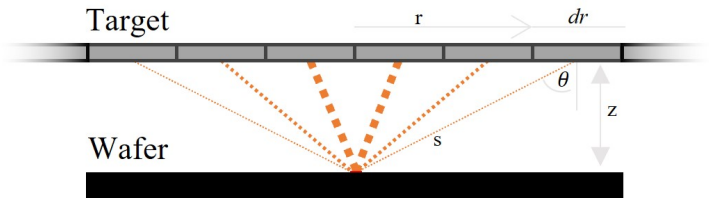

Figure 6.4: Schematic Drawing to visualize variables employed to model the particle flux.

$$\mathsf{F} = \int 2\pi r \cos(\theta) \frac{1}{2\pi \left(r^2 + z^2\right)} dr \tag{6.1}$$

where:

- $2\pi r dr$ is the infinitesimal area of each ring,
- $\cos(\theta)$ represents the distribution of the material as it departs from the target, with θ being the angle between the ejection point and the wafer's center,
- $\frac{1}{2\pi(r^2+z^2)}$ indicates the decrease in material density as it moves away from the target, which is essentially the inverse of the area of a half-sphere.

$F(r, z)$ represents the total number (or amount) of particles that have been emitted from a circular area of radius r on the target and that end up hitting the center of the substrate located at a height z from the target. Further $\cos(\theta) = \frac{z}{\sqrt{r^2+z^2}}$ thus equation (4) can be written as:

$$\begin{aligned} \mathsf{F}(r, z) &= \int 2\pi r \frac{z}{\sqrt{r^2 + z^2}} \frac{1}{2\pi \left(r^2 + z^2\right)} dr \\ &= z \int_0^r \frac{r}{\left(r^2 + z^2\right)^{3/2}} dr \\ &= - \frac{z}{\sqrt{r^2 + z^2}} \Bigg|_0^r = 1 - \frac{z}{\sqrt{r^2 + z^2}} \end{aligned} \tag{6.2}$$

In the context of nano-trench filling via sputtering, a critical parameter is the accessibility of sputtered material to the trench bottom. The geometric constraints dictate that only material with an angular deviation less than or equal to $\theta_{\mathsf{Trench}} = \mathsf{arcTan}(1/AR)$, can effectively reach the trench bottom, where AR denotes the aspect ratio of the trench. Consequently, using basic trigonometry, this condition is fulfilled when:

$$r = \frac{z}{AR} \tag{6.3}$$

Thus, the fraction of material making it to the bottom can be computed as follows:

$$f = \frac{\mathsf{F}\left(\frac{z}{AZ}, z\right)}{\mathsf{F}(R, z)} = \frac{1 - \frac{z}{\sqrt{\left(\frac{z}{AZ}\right)^2 + z^2}}}{1 - \frac{z}{\sqrt{R^2+z^2}}} \tag{6.4}$$

where:

- R is the radius of the target itself,

For example, a fraction of 17.16% is obtained when the target has a diameter of 200 mm (R = 100 mm), the wafer spacing is 50 mm (z), and the trench has a 2:1 aspect ratio. Visualizing the fraction in Figure 6.5, one can perceive that the equation mimics the intuition that larger aspect ratios will yield a smaller fraction, and distancing the sample from the target improves the fraction.

The fraction of material calculated to reach the feature bottoms, as determined by equation 6.4, signifies the most favorable situation one can expect. However, this percentage is often overestimated due to the tendency of sputtered atoms to cluster predominantly at the edges of features, thereby constricting the openings as the deposition process progresses. As a result, with the film's increasing thickness, the actual probability of atoms making it to the bottom of the features diminishes steadily.

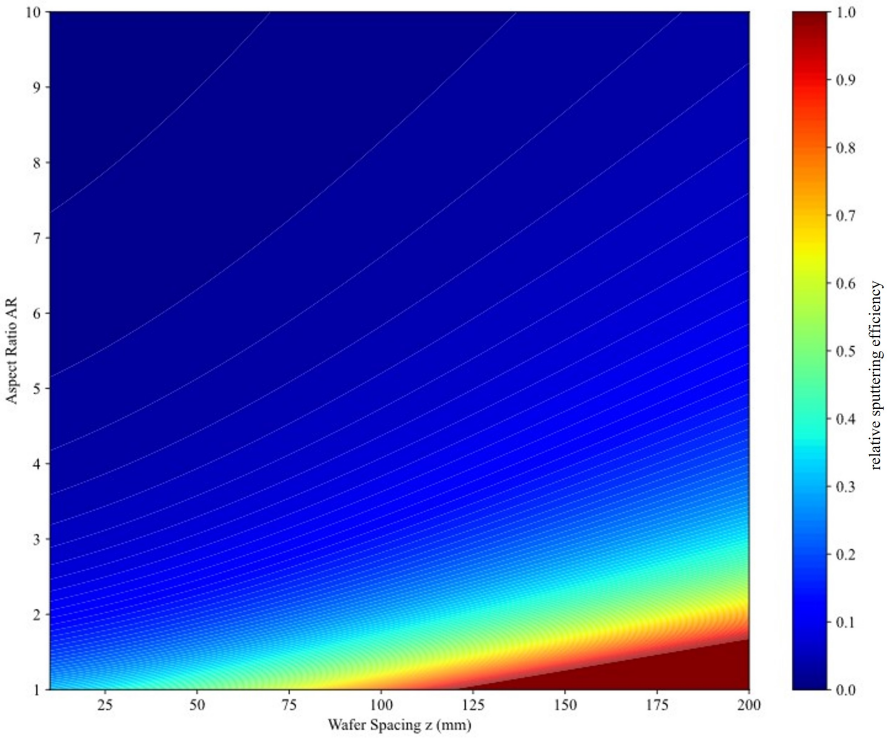

Figure 6.5: Fraction of sputtered material reaching trench bottom. The color scale represents the relative sputtering efficiency between 0 and 1. The plot assumes a cosine sputtering distribution, with z ranging from 10 mm to 200 mm and AR ranging from 1 to 10. The 'jet' color map is used to better visualize the variations, where darker colors indicate lower efficiency and brighter colors indicate higher efficiency. R = 100mm.

Utilizing a collimator, trench-filling can be improved by selectively permitting the passage of atoms that have incident angles below a certain threshold. If said collimator is used, a correction factor needs to be added to the calculation of the flux. Not only does the collimator limit the angular spread but also the quantity. As visualized in Figure 6.6 the material beam cross-section that can pass through effectively depends on the angle of incidence. The largest effective opening can be computed as such[206]:

$$d' = (d - h\,\mathsf{tan}(\theta)) \tag{6.5}$$

$$d' = d - dAR_c\frac{r}{z} \tag{6.6}$$

The fraction of atoms T passing through the collimator at an angle with respect to normal incidence can thus be given as:

$$T = \frac{d'}{d} = \frac{d - dAR_c\frac{r}{z}}{d} = 1 - AR_c\frac{r}{z} \tag{6.7}$$

In analogy to equation (4), the flux of atoms can thus be written as:

$$\begin{aligned}\mathsf{F} &= z\int_0^r \frac{r}{(r^2+z^2)^{3/2}}T\,dr \\ &= z\int_0^r r\frac{1 - AR_c\frac{r}{z}}{(r^2+z^2)^{3/2}}\,dr \\ &= z\left(\int_0^r \frac{r}{(r^2+z^2)^{3/2}}\,dr - \frac{AR_c}{z}\int_0^r \frac{r}{(r^2+z^2)^{3/2}}\,dr\right)\end{aligned} \tag{6.8}$$

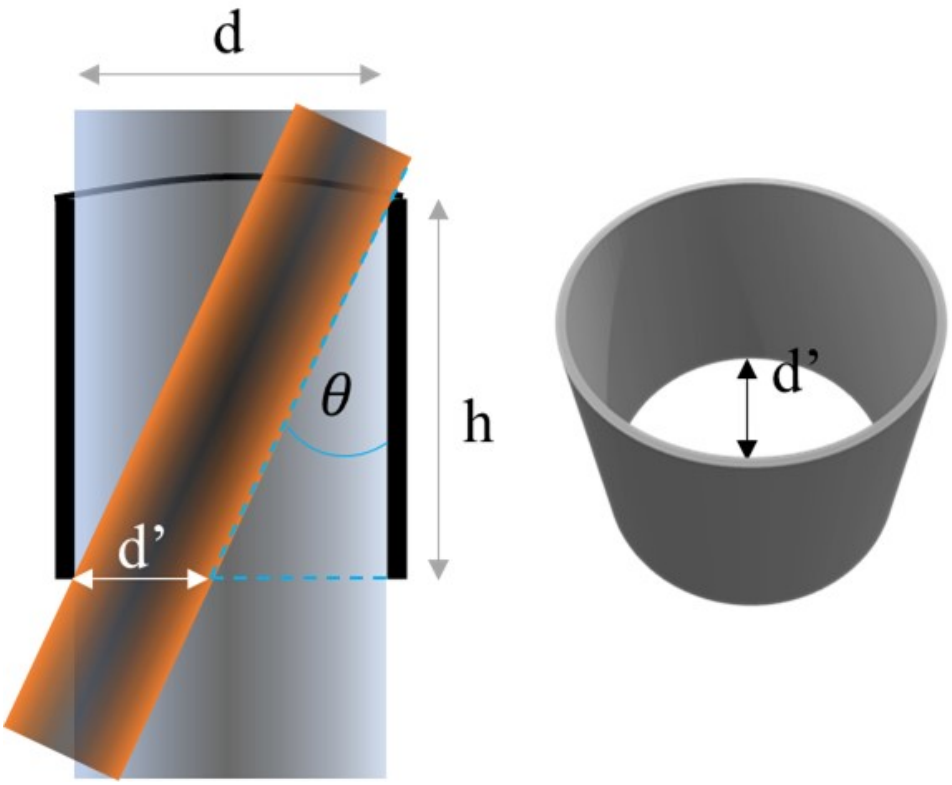

Figure 6.6: Schematic visualization of variation of the pass-through beam of material at an incline. Left: Cross-sectional view, Right: three-dimensional top-down view at an incline; d is the original collimator diameter, d' is the largest opening distance, when reaching the collimator hole at an incline θ

Computing the integration, the general flux amounts to:

$$\mathsf{F}(r, z, AR_c) = 1 - \frac{z}{\sqrt{r^2 + z^2}} - \frac{AR_c}{z}\left(1 - \frac{z}{\sqrt{r^2 + z^2}}\right) \tag{6.9}$$

It can easily be verified that "removing" the collimator by having $AR_c = 0$ equation 6.4 is retrieved. In the analysis of collimated sputter deposition, it's crucial to consider the maximum flux of atoms that can pass through the collimator, which acts as a limiting factor. This upper limit is defined by:

$$F'_{\text{collimator}} = F\left(\frac{Z}{AR_c}, Z, AR_C\right) \tag{6.10}$$

Further, the flux that reaches the bottom of the trenches on the wafer is given by:

$$F'_{\text{wafer}} = F\left(\frac{Z}{AR}, Z, AR_C\right) \tag{6.11}$$

And the total flux reaching the collimator from the target:

$$F_{\text{Total}} = F(R, z, 0) \tag{6.12}$$

To construct a rigorous mathematical model for flux behavior, it is imperative to enforce constraints that are aligned with the underlying physics. Specifically, the flux values defined by equations (6.10) and (6.11) must be restricted to non-negative numbers. The constraints are:

$$F_{\text{collimator}} = \max\left(0, \min\left(F'_{\text{collimator}}, F_{\text{Total}}\right)\right) \tag{6.13}$$

$$F_{\text{wafer}} = \max\left(0, \min\left(F'_{\text{wafer}}, F_{\text{collimator}}\right)\right) \tag{6.14}$$

The total material fraction reaching the wafer can be computed as:

$$f_{\text{total}} = \frac{F_{\text{collimator}}}{F_{\text{total}}} \tag{6.15}$$

Further, an effectiveness ratio η has been introduced to evaluate the flux reaching the bottom of a feature relative to the maximum possible flux deliverable by the collimator. This ratio is formulated as:

$$\eta = \frac{F_{\text{wafer}}}{F_{\text{collimator}}} \tag{6.16}$$

The effectiveness ratio η quantifies the efficiency with which the collimator-assisted sputter deposition process fills a given feature, accounting for both the geometrical constraints of the feature itself and the limitations imposed by the collimator. A value of η approaching 1 indicates that all atoms passing through the collimator can reach the bottom of the trench, possibly allowing for an enhanced trench filling. a critical modification is implemented in the computational model to address certain non-physical scenarios. Specifically, the effectiveness ratio with a collimator ($\eta_{\text{collimator}}$) is compared against that without a collimator ($\eta_{\text{no collimator}}$). In instances where $\eta_{\text{collimator}}$ falls below $\eta_{\text{no collimator}}$, the latter is returned instead, adhering to the physical principle that the introduction of a collimator cannot degrade the filling efficiency below what could be achieved without one.

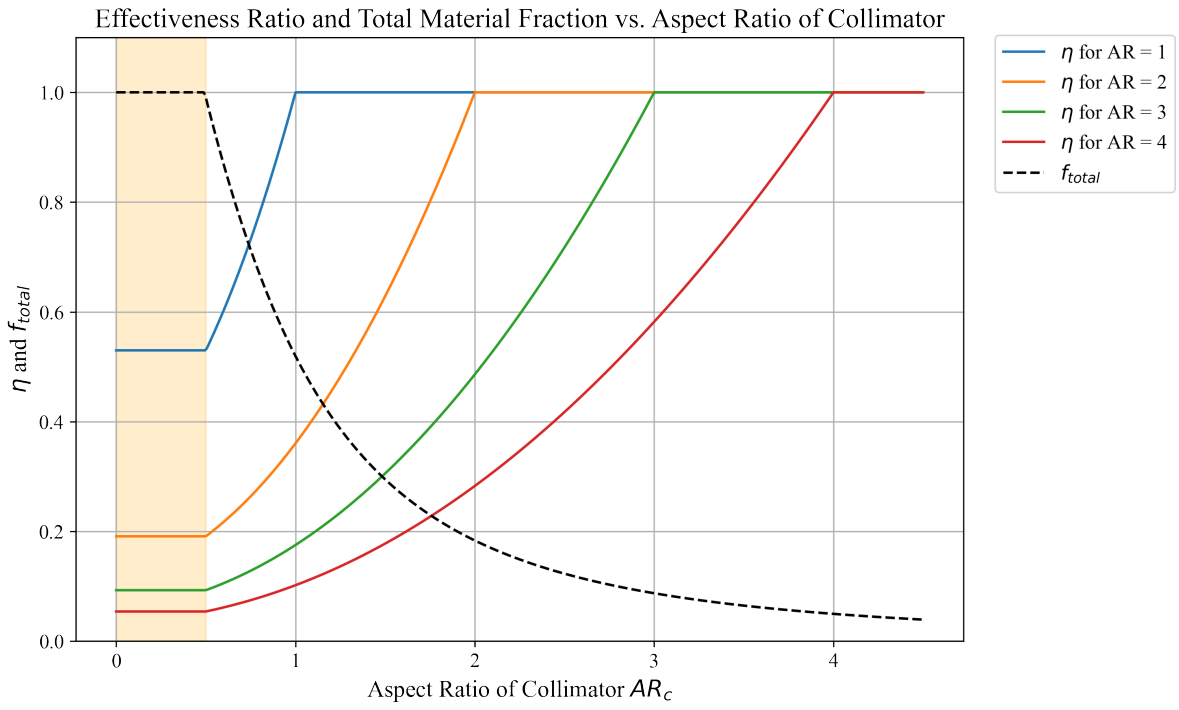

Figure 6.7: Effectiveness Ratio (η) and Total Material Fraction (f_{total}) as Functions of Collimator Aspect Ratio (AR_c). A target radius of R = 120 mm, and height of z = 50 mm is used for visualization purposes, with trenches having aspect ratios of 1 and 2 respectively. The orange-shaded region indicates the range of AR_c values where the collimator has negligible influence on the flux. The dashed black line represents f_{total}, and provides a reference for the maximum possible material that could pass through the collimator.

In Figure 6.7, it is observed that optimal trench filling is achieved when the aspect ratio of the collimator is meticulously matched with the intrinsic aspect ratio of the trench. Additionally, the descending trajectory of the dotted line, which signifies the fraction of material reaching the bottom of the trench, transitions from unity to zero as the aspect ratio of the collimator (AR_c) is increased. This trend highlights a notable limitation of collimators, particularly their considerable reduction in deposition rate. The model allows for a first intuitive understanding of the main collimator design variable which is its aspect ratio. It needs to be noted that the model assumes collision-free particle trajectory, no temperature dependence and that particles stick directly upon impact. To improve the models used for real-world applications, it can be further enhanced by adding collimator passes through probability p_{pass} which in a first simple form can be defined by the effective area ratio of the top circles created by the holes versus the full top surface[207]. Equation 6.17 computes the value for a hexagonal array of holes (see Figure 6.8):

$$p_{pass} = \frac{A_{holes}}{A_{top}} = \frac{\frac{1}{2}\pi\left(\frac{d}{2}\right)^2}{\frac{\sqrt{3}}{4}P^2} = \frac{\pi}{2\sqrt{3}}\left(\frac{d}{P}\right)^2 \tag{6.17}$$

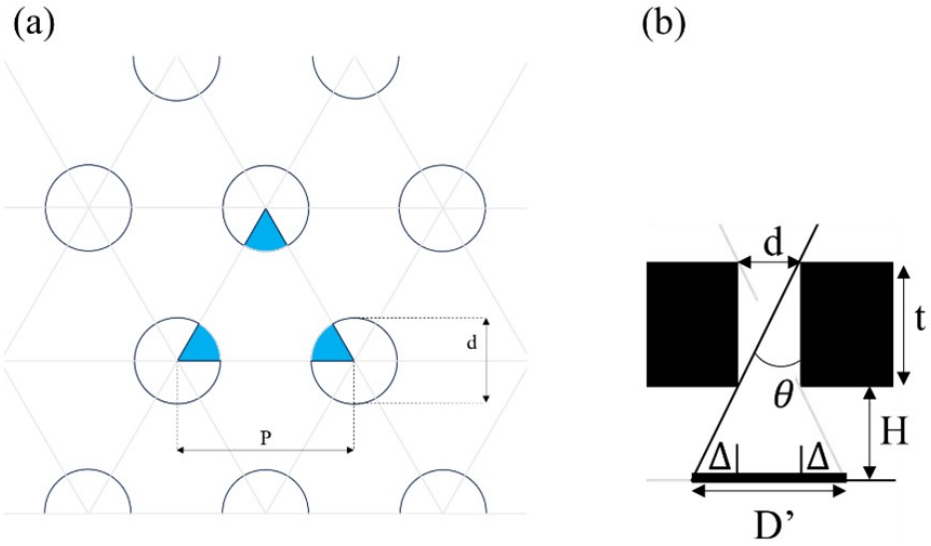

Figure 6.8: Analysis of the Collimator Support Structure: (a) A depiction of the hexagonal pattern. The blue-shaded regions represent pass-through areas, with their ratio to the entire matrix area defining the pass-through probability. (b) Lateral perspective showcasing the impact of the distance between the collimator and the wafer. Here, d denotes the diameter of the collimator hole opening, while D' symbolizes the expanded deposition diameter due to dispersion at a maximum angle of θ. This results in an effective deposition width increase of 2Δ.

Further, the distance of the collimator from the wafer also plays a role. The solid, non-perforated sections of the collimator obstruct the passage of incoming particles. In that sense, the operation of collimators parallels the principles of stencil lithography. Particles arriving at more oblique angles effectively expand or "blur" the deposition circle. While blurring is a limitation of stencil lithography diminishing the resolution, in the context of collimators, such blurring is a sought-after effect to obtain a uniform surface profile. For a single hole, the deposition diameter is given by:

$$\begin{aligned} D' &= d + 2\Delta \\ &= d + 2((H+t)\tan(\theta) - d) \\ &= 2(H+t)\tan(\theta) - d \\ &= 2(H+t)\frac{1}{AR_c} - d \\ &= \frac{2H}{AR_c} \end{aligned} \tag{6.18}$$

From equations 6.17 and 6.18 it becomes clear that to enhance deposition uniformity for a specified AR_c, there's a need to minimize the pitch P between the holes and position the collimator at a maximal distance H above the wafer. However, it's crucial to maintain a balance, as bringing the collimator closer to the target leads to a decline in the total material fraction f_{total} reaching the wafer. The reason is that as we approach the dispersion of atoms hitting the collimator at larger angles from the normal increases, in comparison, relative to that, the total material that passes through η declines.

6.1.2. Experimental Implementation

An aluminum- and teflon-based collimator are fabricated, displayed in Figure 6.9a, b. The collimators consist of two parts, a base structure, and a collimator grid. This design allows to precisely position the collimator over chips, and then close the system with the top grid (see Figure 6.9c). For both types of materials used, the collimator grid is designed with holes that have a diameter of 1 mm, a period of 1.2 mm, and a height of 3 mm. This design results in an aspect ratio of 3 for the collimator. Several stereolithographic 3D printed collimators were fabricated using RC70, a ceramic-particle-infused photoresist resin that can tolerate temperatures up to 100°C. These devices were utilized for preliminary evaluations, particularly to assess the clearance of the deposition chamber entry slot (see Figure 6.9d) constraining the maximum height of the collimator to 8 mm taking the base thickness of the carrier wafer into account. For ease of reusability, the collimators were simply taped to the carrier wafer (see Figure 6.9e).

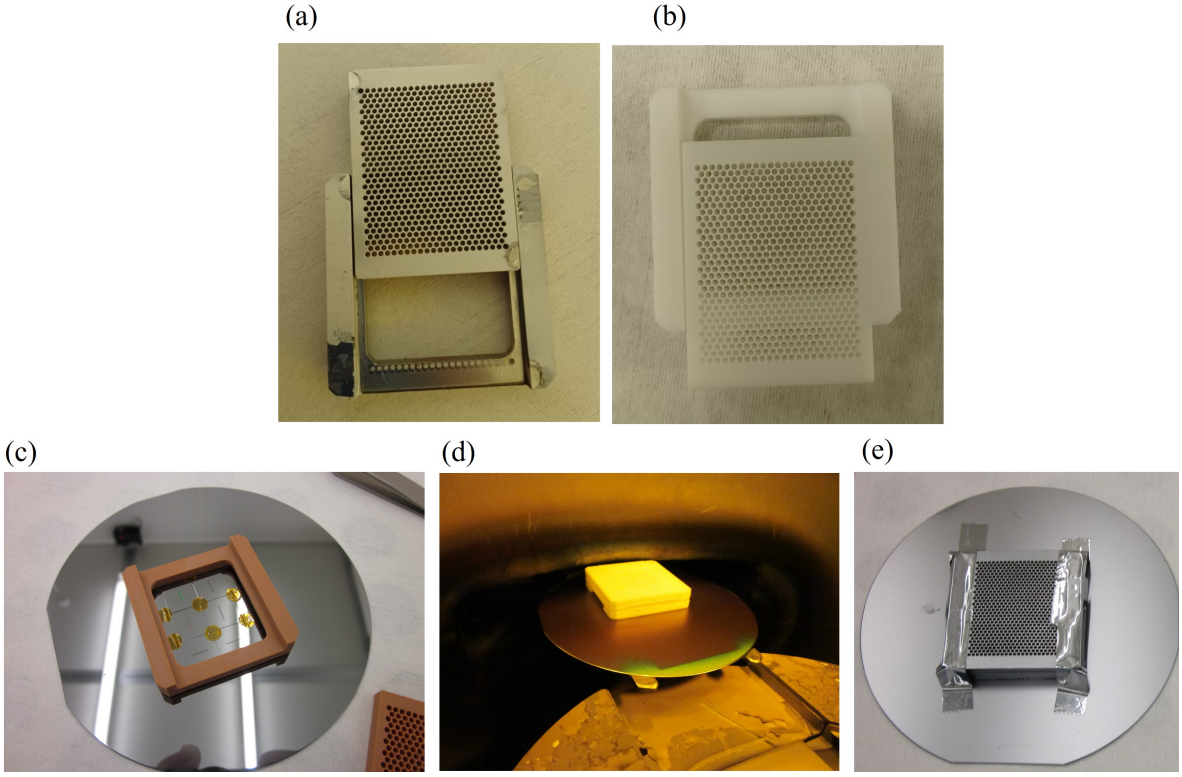

Figure 6.9: Implantation of Collimator: (a) Aluminum-based collimator, (b) Teflon-based collimator, both with an aspect ratio of 3. (c) The collimator design consisting of a base structure and a top grid, allowing precise positioning over chips. (d) Stereolithographic 3D printed collimators using RC70, showing the deposition chamber entry slot. (e) Collimators taped to the carrier wafer for ease of reusability.

To test the deposition efficiency silicon chips with an array of trenches having varying aspect ratios were fabricated (see Table 6.1) using e-beam lithography and subsequent DRIE etching. Two trench arrays are fabricated with smaller and larger pitches to test for local effect.

Table 6.1: SEM-based measured trenches geometry. All trenches consistently exhibit a depth of approximately 540 nm. Derived measurements may bear slight variations due to factors such as calibration, imaging conditions, and operator interpretation.

No°	Width (nm)	Pitch (nm)	AR	No°	Width (nm)	Pitch (nm)	AR
1	900	300	0.6	5	230	300	2.34
2	593	300	0.91	6	226	100	2.38
3	457	300	1.18	7	216	500	2.5
4	319	300	1.69				

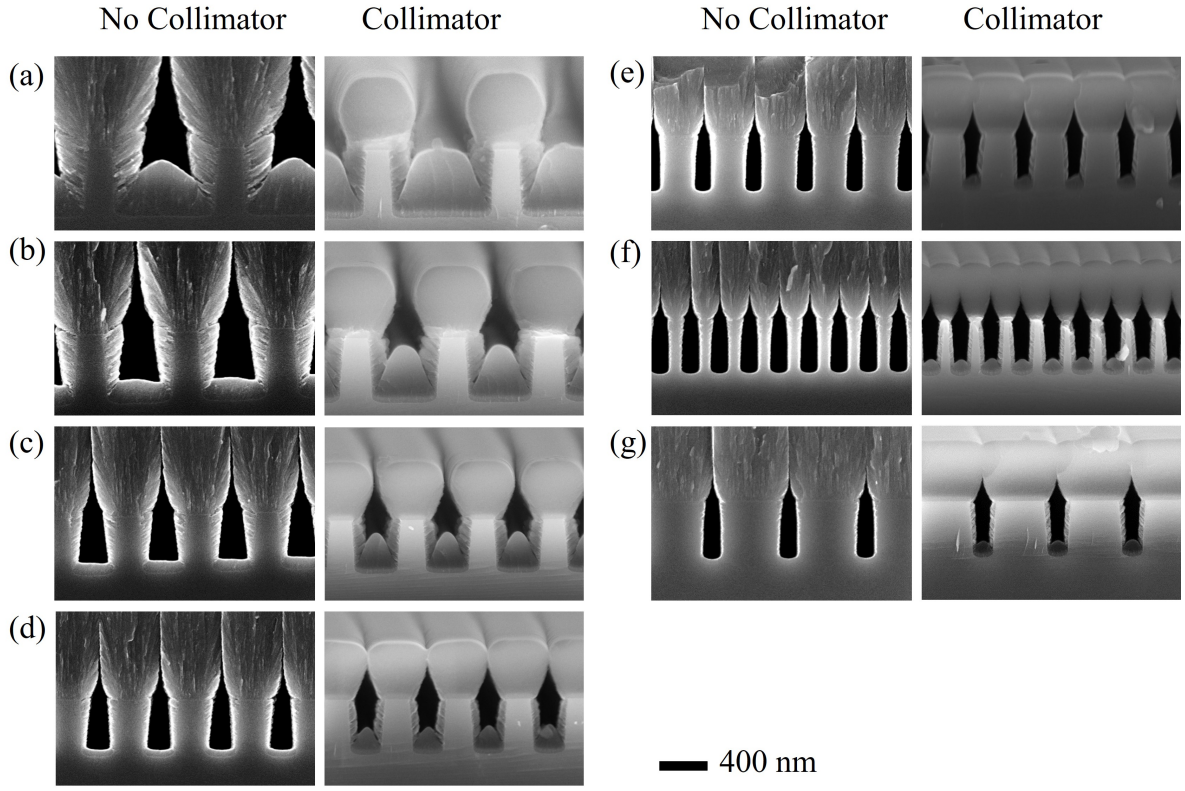

Figure 6.10: Cross-sectional SEM images displaying aSi deposition into trenches of varying aspect ratio (AR) with and without collimator. Deposition duration 4 min (no collimator) and 59 min (with collimator). The AR are: (a) 0.6, (b) 0.91, (c) 1.18, (d) 1.69, (e) 2.34, (f) 2.38, (g) 2.5. The pitch for trenches (a) – (e) is 300 nm, for trenches (f) 100 nm and for trenches (g) 500 nm. The deposition rate without a collimator is approx. 110 nm/min, with collimator the deposition rate is slowed to approx. 10 nm/min. Machine: DC Sputtering at 800W with a flowrate of 29 sccm of Argon, 5.10-7 mbar, planar 200 mm target.

As can be seen in Figure 6.10 the produced collimators do improve the trench filling. Considering that the fabricated collimators have a pass-through probability of 63%, and a total material fraction f_{total} of $0.09\,(AR_c = 3, z = 42$ mm$, R = 100$ mm$)$, a deposition rate of $0.63 * 0.09 * 110$ nm$/$min $=$ 6.2 nm$/$min is computed, which is well within the order of magnitude of the measured 10 nm$/$min. Figure 6.11 shows the increase in trench filling ratio by utilizing the collimator ($AR = 3$) compared to no collimator. For higher trench aspect ratios the increase is less pronounced, however for aspect ratios close to unity, the filling ratio is improved by approximately 3 times.

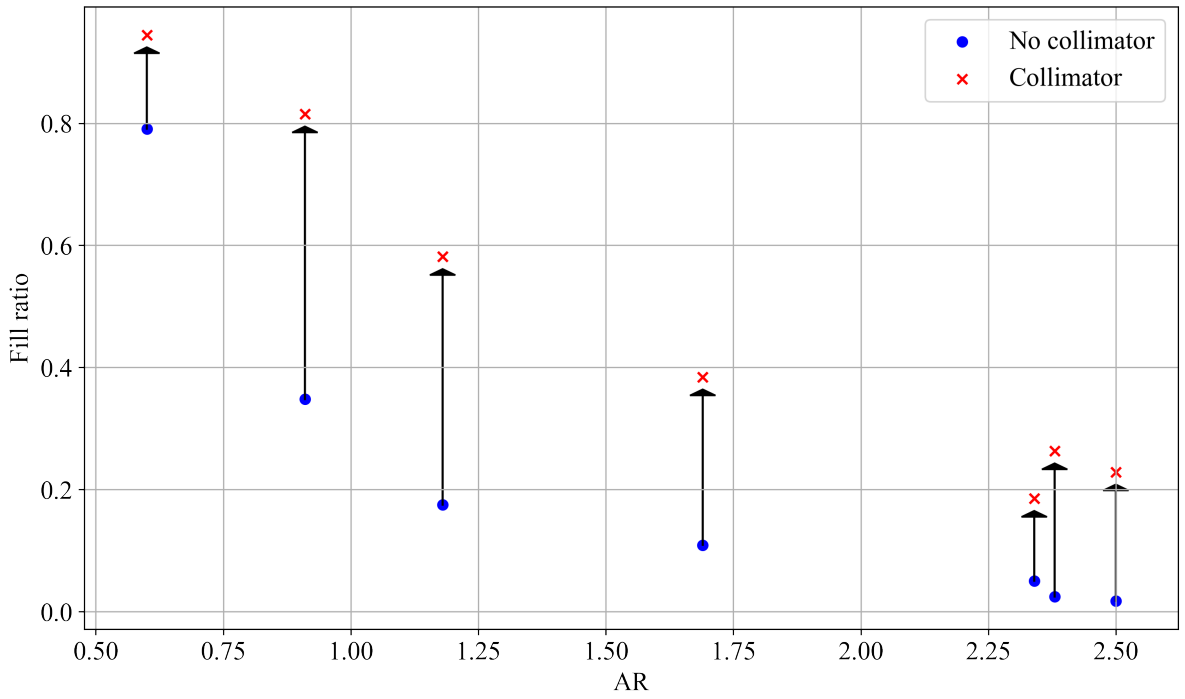

Figure 6.11: SEM measured trench filling percentage of the tested nano-trenches for both open sputtering and with collimator.

While the results do show improvement in filling compared to pure DC sputtering, the outcome is not yet the clean void-free filling that would compensate for the much reduced deposition rates and added fabrication complexity. Thus it is decided to fabricate the scaling-up proof-of-concept prototype using LPCVD which has shown excellent conformal void-free filling.

6.2. Proof-of-concept: Scaling

The following section outlines the experimental investigation of a membrane-first approach, a process flow that would allow for a scalable process.

6.2.1. Optics

Again, the geometry for this prototype is found through gradient-free optimization coupled to RCWA simulations. Figure 6.12 shows the simulated reflection spectrum in both idle (membrane at 0 nm displacement) and actuated (membrane at 100 nm displacement) states. Evaporation of a 5nm layer of aluminum not only improves the electrical conductivity of the membrane but also improves the optical performance, essentially going from a contrast ratio of 1:6 to 1:8. This is mainly due to the increased reflectivity in the idle state. The contrast ratio is not yet within the one reported for a newspaper, i.e. 15:1 (see Figure 2.2), however, it should already yield good outdoor visibility (see Table 2.1 for reference).

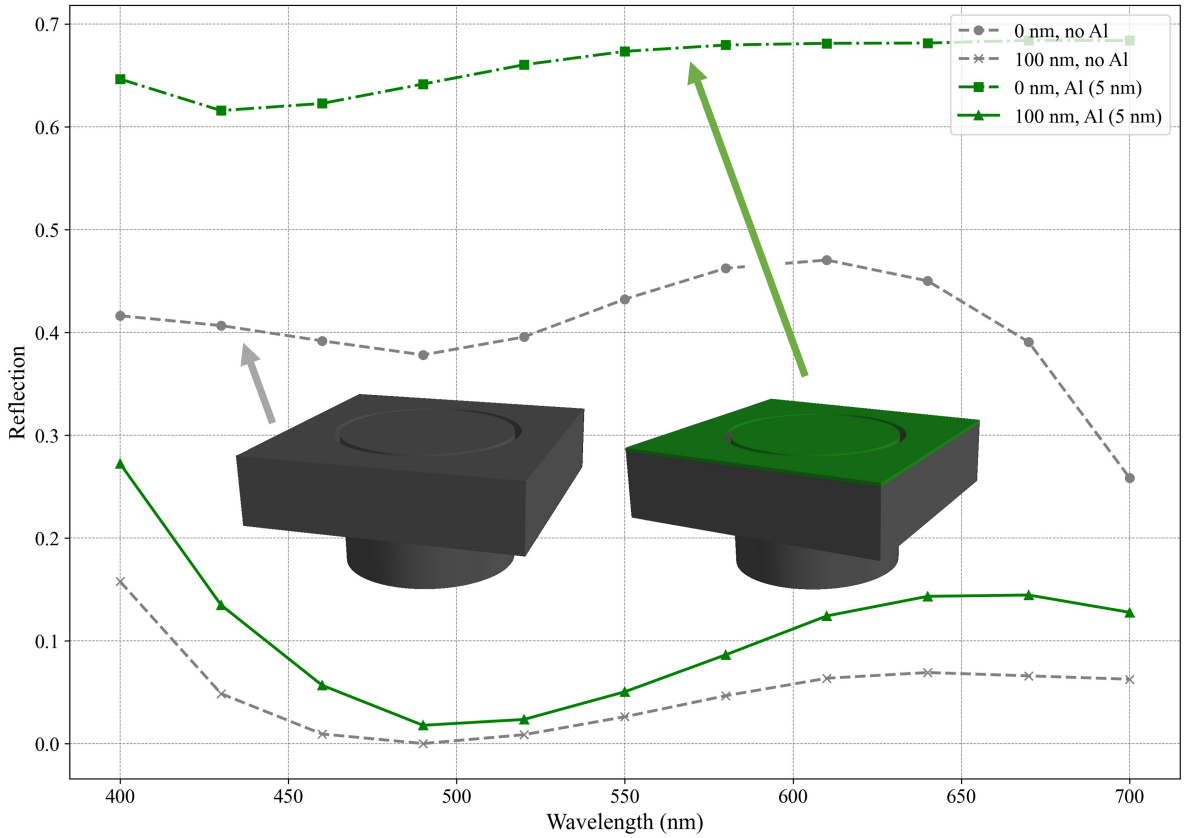

Figure 6.12: Simulated reflection spectra for LPCVD-filling prototype. Idle membrane position with 0 nm, and actuated membrane position of 100 nm is shown, both with and without evaporated 5nm of Al layer.

6.2.2. Process-Flow and initial short loop experiments

The high-level fabrication process is outlined in Figure 6.13 (a detailed runcard is given in the appendix A.6). A low-resistance silicon (Si) wafer substrate is used for optimal grounding during the electrostatic actuation of the membrane. Upon this substrate, a specific sequence of material layers is initially deposited, as shown in Figure 6.13a. The composition of these layers begins with a dielectric oxide layer serving as an electrical isolation layer. This is followed by an amorphous silicon (aSi) layer, designed to protect the dielectric layer from being etched during the final MEMS hydrofluoric (HF)-vapor release step, depicted in Figure 6.13g. Subsequently, a second SiO_2 layer is applied to act as the sacrificial layer, accompanied by an aSi membrane layer and a final thin SiO_2 buffer layer. Following the deposition steps, etching processes are executed to create holes in both the membrane and the sacrificial layer for the pillars, as shown in Figure 6.13b. To define the gap between membrane and pillar, a conformal Atomic Layer Deposition (ALD) of SiO_2 is performed, illustrated in Figure 6.13c. This procedure is critical for achieving potentially narrow gaps. The SiO_2 deposited at the bottom of the holes via ALD is then removed to ensure that the pillars remain anchored to the substrate during the subsequent HF vapor membrane release step, shown in Figure 6.13g. Following this, the LPCVD process is implemented to fill the etched holes with the designated pillar material, as depicted in Figure 6.13e. This is followed by an etch-back procedure, shown in Figure 6.13f. In this step, the LPCVD-deposited material is etched back until only the material within the holes remains. The SiO_2 buffer layer allows for a slight over-etch without damaging the membrane. Finally, the MEMS device is released using HF Vapor, and 5 nm of aluminum is evaporated, as shown in Figure 6.13h.

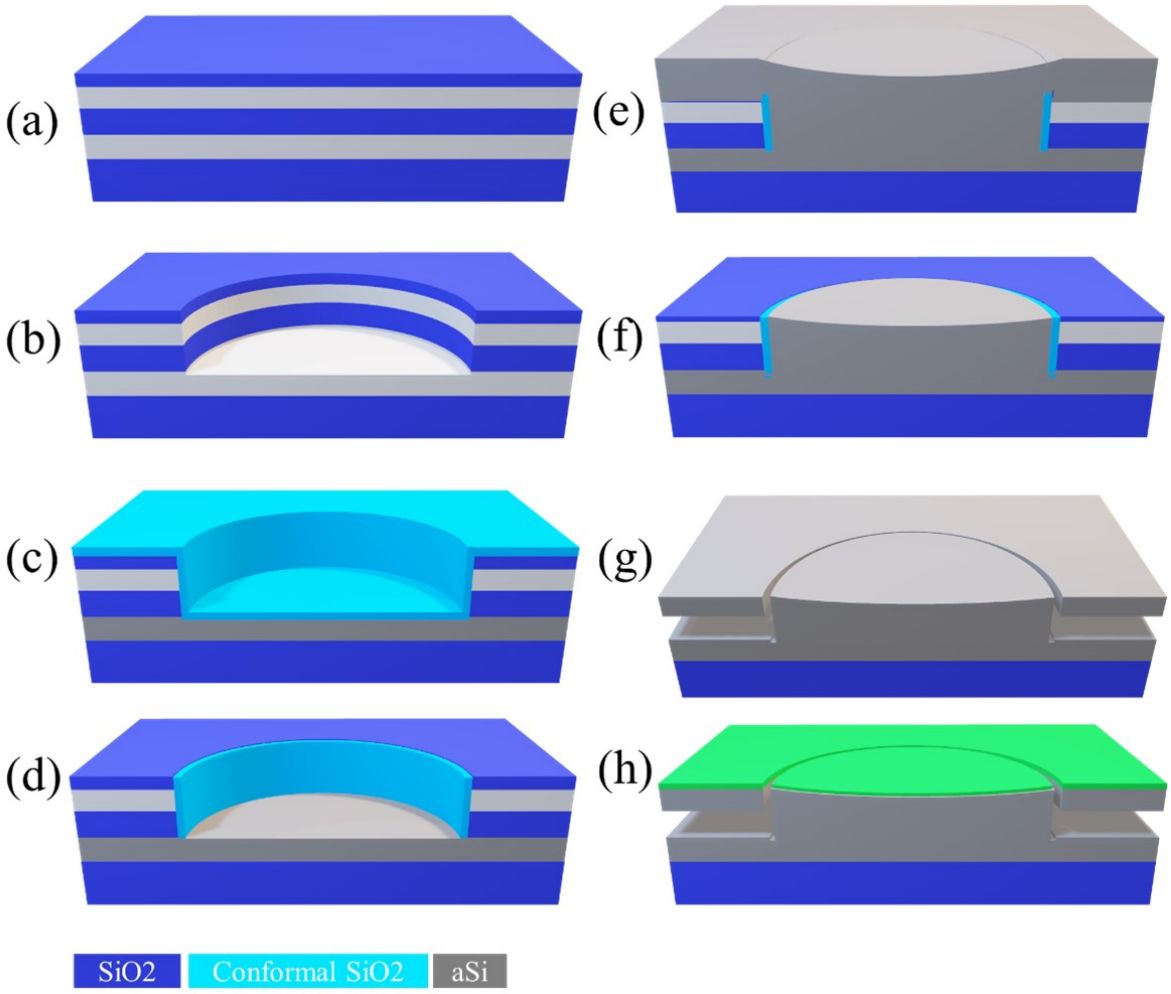

Figure 6.13: LPCVD-filling process flow. (a) Material deposition, (b) hole etch, (c) ALD SiO_2 conformal deposition, (d) ALD SiO_2 etch back for bottom removal, (e) LPCVD filling, (f) etch back and (g) HF vapor etch, (h) Al evaporation.

In an effort to reduce post-release deflection, as observed in the disk-membrane prototype, two distinct membrane thicknesses are investigated, specifically 50 nm and 200 nm. While the initial intention is to deposit all layers at approximately the same temperature using aSi LPCVD for the membrane and LTO for the sacrificial oxide, this procedure is only executed for the 50 nm sample. Owing to constraints in machine availability, a transition from Low-Pressure Chemical Vapor Deposition (LPCVD) to Plasma Enhanced Chemical Vapor Deposition (PECVD) is implemented for fabricating the thicker membrane. In this revised process, PECVD amorphous Silicon (a-Si) is utilized for the membrane material, and PECVD Silicon Dioxide (SiO_2) is employed for the sacrificial layer. This alteration, while expediting the experimental timeline, introduces a variation in deposition conditions. Consequently, alongside the change in thickness, the deposition temperatures and materials have transitioned, making a direct comparison solely based on thickness unfeasible. It is observed that these parameters significantly affect the residual stress profile and, in turn, the post-release behavior of the microbridge. A simplified process flow design is adopted for both membrane configurations to maintain a focused investigation. The fabrication steps are limited to the deposition of the sacrificial oxide and the membrane material. Subsequently, the membranes are patterned using e-beam lithography and are released, without the introduction of pillars, which are considered non-impactful to the post-release bending behavior under investigation. Figure 6.14 illustrates the contrasting post-release deflection behavior between the two membrane configurations across varying microbridge lengths, as captured by Digital Holographic Microscopy (DHM). Panel (a) displays a consistent upward bending for the 50 nm LPCVD a-Si membrane across all

lengths. Conversely, panel (b) reveals a distinct behavior for the 200 nm PECVD a-Si membrane: remaining relatively flat up to a 20 μm length, beyond which a downward bending is observed. The differing post-release behaviors underscore the pivotal role of deposition methods and thicknesses in governing the residual stress distribution in MEMS devices. As a flat membrane post-release is desired, the 200 nm PECVD design is retained.

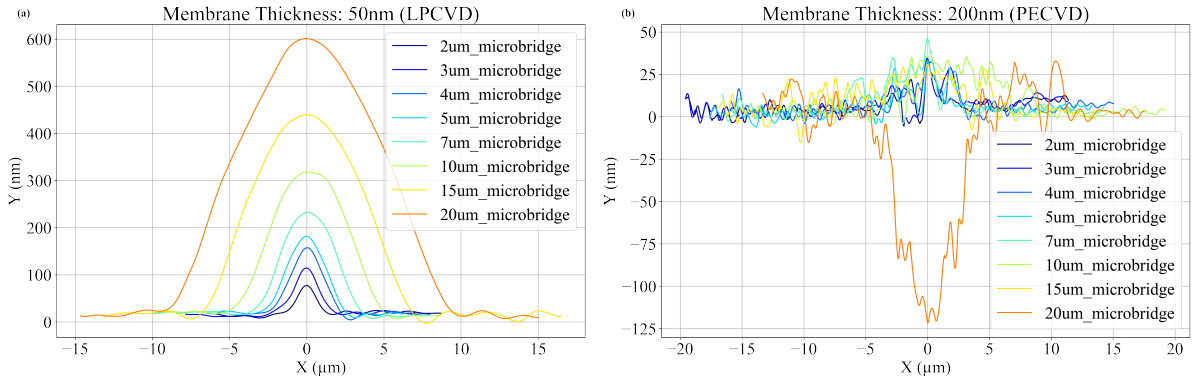

Figure 6.14: DHM measurements of microbridge deflections of different lengths. Residual stress leads to the bending of the membrane post-release. (a) membrane thickness of 50 nm LPCVD aSi membrane on 150 nm LTO, (b) membrane thickness of 200 nm PECVD aSi membrane on 150 nm PECVD SiO_2.

Figure 6.15 presents a series of Scanning Electron Microscopy (SEM) images, illustrating the fabricated membranes designated for post-release bending examination. In Figure 6.15a, a slight upward deflection is discernible on the LPCVD sample with a membrane thickness of 50 nm and a length of 10 µm. Transitioning to panel b, the relatively reduced quality in panel a compared to the other picture is because slower SEM scans result in membrane bending due to charging effects. Nevertheless, the essence of a slight upward bending can be seen. In Figure 6.15b, the PECVD sample, identical in dimensions but with a thicker membrane of 200 nm, exhibits no visible deflection, underscoring the impact of membrane thickness on post-release stability. Lastly, Figure 6.15c presents a distinctive scenario where the 200 nm PECVD sample, extended to a length of 20 µm, demonstrates a downward bending. The bending behavior is further accentuated in the inset images at the edge and in the middle of the microbridge, providing a closer examination of the deflection. The width of all samples is maintained at 7 µm.

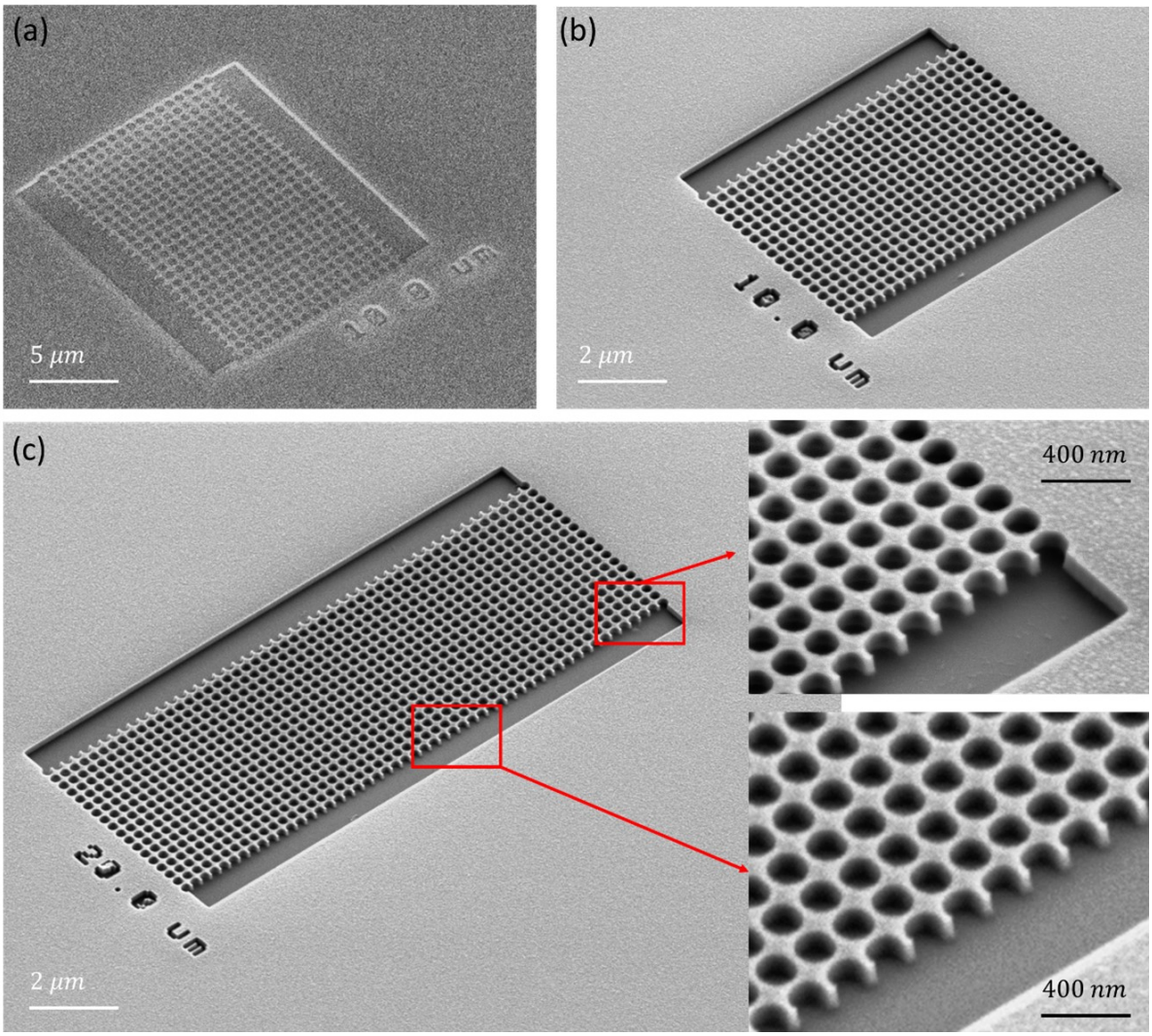

Figure 6.15: SEM images of fabricated membranes for post-release bending test. (a) membrane thickness of 50 nm and a length of 10 µm, LPCVD sample with LTO sacrificial layer. (b) membrane thickness of 200 nm and a length of 10 µm, PECVD sample with PECVD oxide sacrificial layer. (c) membrane thickness of 200 nm and a length of 20 µm, PECVD sample with PECVD oxide sacrificial layer, bends downward as depicted in the inset pictures at the edge and in the middle of the microbridge. All samples have a width of 7 µm.

6.2.3. Fabrication Results

In the following, the fabrication steps are outlined. Figure 6.16 shows a cross-sectional SEM image of all PECVD-deposited layers. The deposition is carried out at 300°C, 1000 mTorr pressure, using SiH_4/N_2 for aSi and SiH_4/N_2 - N_2O for SiO_2. From the bottom to the top, one can distinguish a 185 nm layer of insulating oxide, followed by an 85 nm aSi protection layer, then a 130 nm sacrificial oxide layer, the membrane layer, here 195 nm thick, and an oxide protection layer of 60 nm. The deposition would need to be further calibrated to have values closer to the simulated design, but as this is for a proof of concept of the fabrication, the values are deemed close enough. The last layer on the very top is the e-beam resist CSAR used as a mask during the etching of the holes.

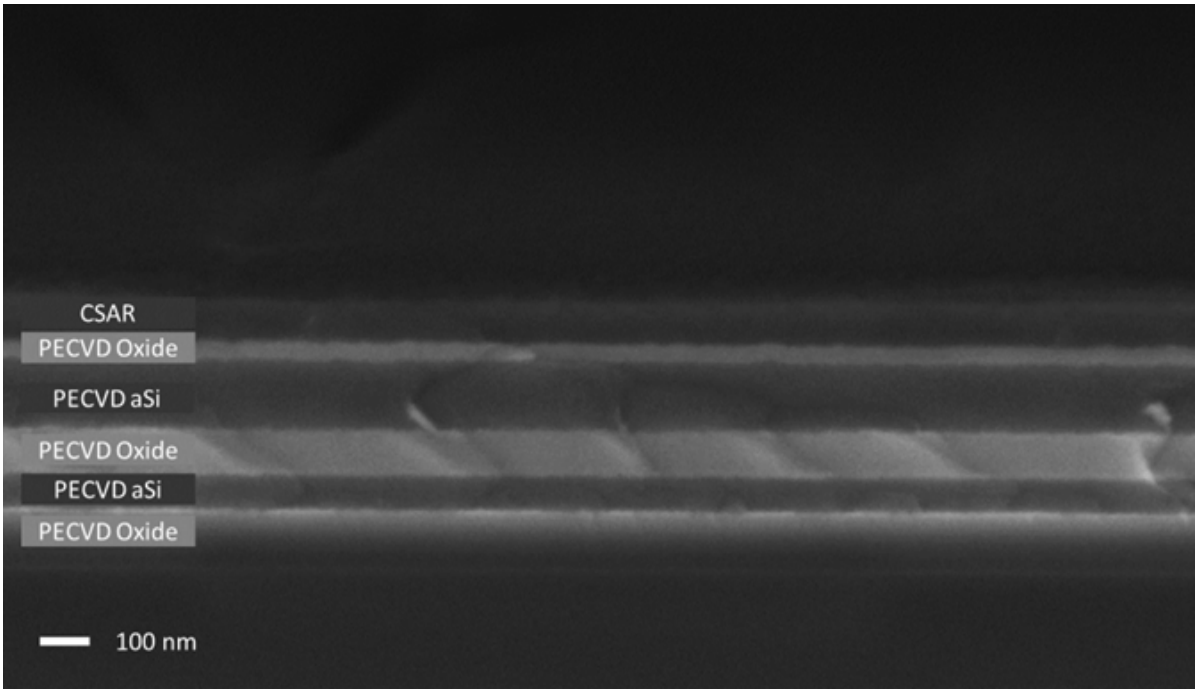

Figure 6.16: Cross-section of SEM image of deposited layers: 185 nm PECVD SiO_2, 85 nm PECVD aSi, 130 nm PECVD aSi, 195 nm PECVD aSi, 60 nm PECVD SiO_2, and e-beam resist CSAR. Deposition Machine: Oxford Instruments PlasmaPro 100 ICPCVD

Next, the holes are etched. Figure 6.17 shows a cross-sectional image after completing the etching process. Sequential etching is employed to etch through the top protective oxide layer, the aSi membrane layer, and the sacrificial oxide layer. The aSi is etched using inductively coupled plasma (ICP). Similarly, the SiO_2 etching is carried out in an ICP-based high-density plasma using a mixture of $C_4F_8/H_2/He$ gases.

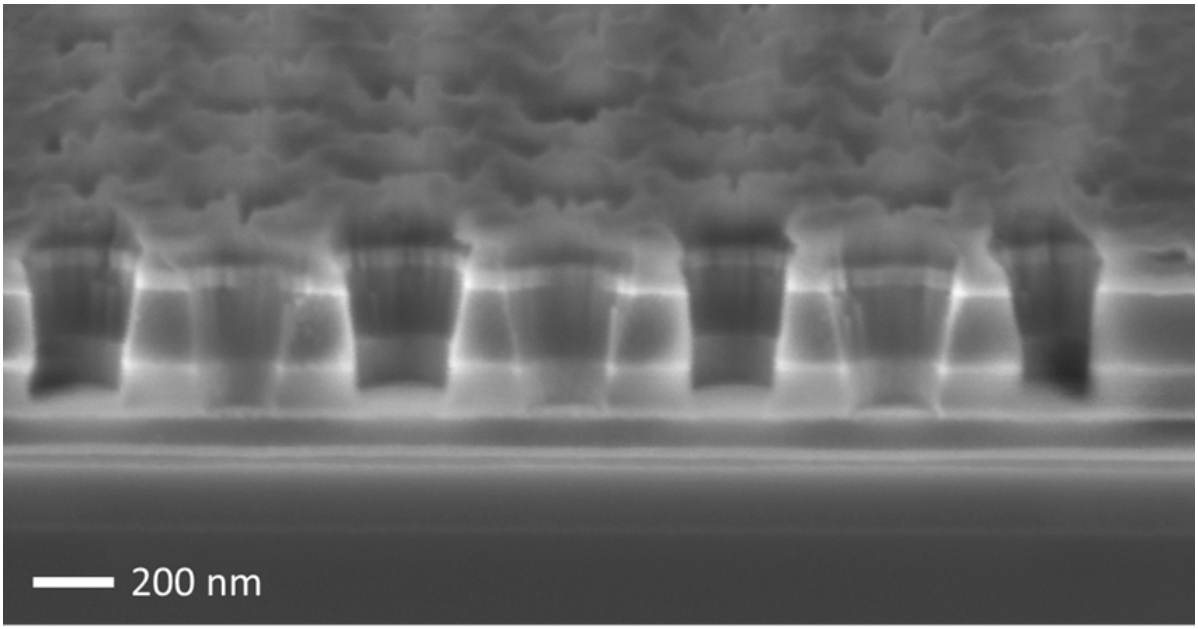

Figure 6.17: Cross-Section SEM image of the membrane after etching steps. Holes dimensions: period: 400 nm, diameter: 240 nm. Machines: aSi etching was carried out using Alcatel AMS 200 SE, oxide etch using the SPTS Advanced Plasma System (APS)

One can observe a slight tilt in the etch profile of the aSi, which can be improved through proper

process parameter tuning. However, for this initial demonstration, further refinement is deemed unnecessary as the incline of the sidewalls does not adversely affect the membrane movement once the holes are filled with the pillars, which will naturally conform to the shape of the holes. Once the etching has been completed, the conformal SiO_2 is applied using atomic layer deposition at 200°C. Figure 6.18 shows a cross-sectional SEM image of cleaved trenches with different aspect ratios that have undergone ALD SiO_2 deposition. For better visibility under the SEM, the ALD layer has a thickness of 40 nm. Thinner layers are easily applicable, but for demonstration purposes, this thickness is chosen.

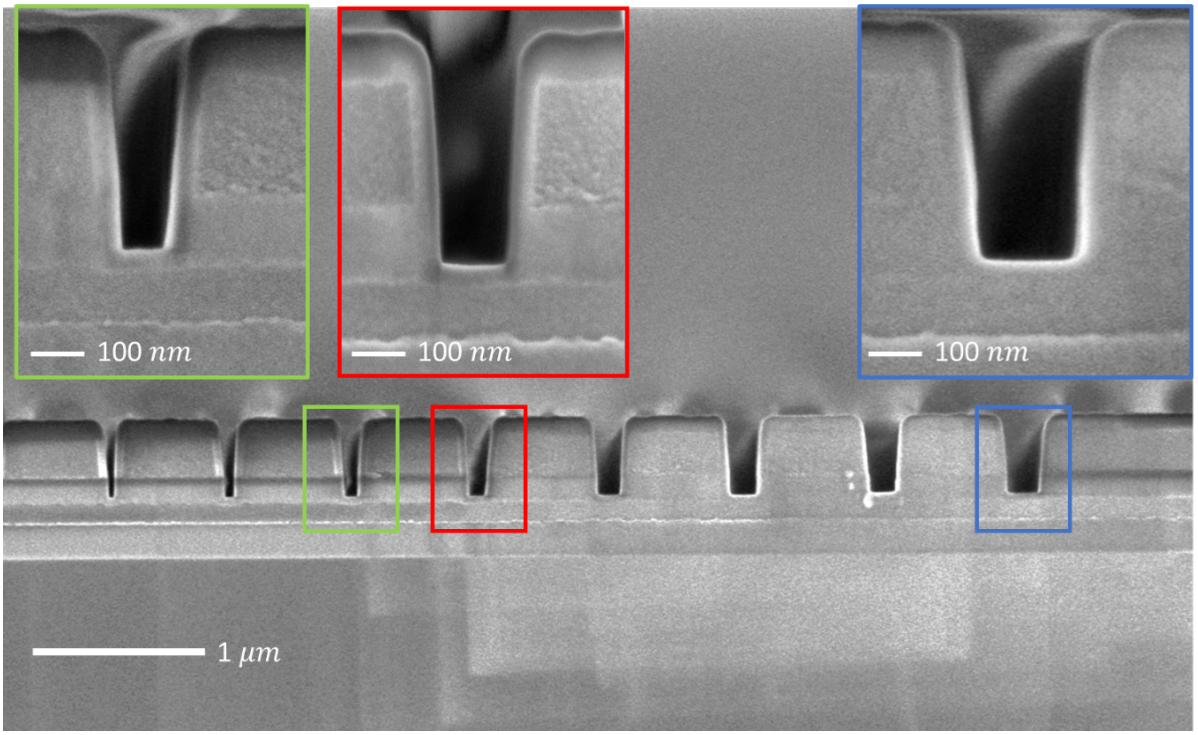

Figure 6.18: Cross-sectional SEM image of cleaved nano trenches after ALD SiO_2 deposition. Deposition thickness 40 nm. ALD machine: BENEQ TFS200

To anchor the pillars to the substrate during the HF vapor release of the membrane, the pillars must not have any oxide underneath them. Thus, directional etching is applied to remove the oxide at the bottom of the holes. A standard fluoride-based etching recipe is used, and the ending time is carefully calibrated to retain the oxide on the sidewalls while removing it at the bottom, as depicted in the inset of the etch rate calibration plot shown in Figure 6.19. For 30 nm of ALD, SiO_2 an etching time of 14 seconds was used.

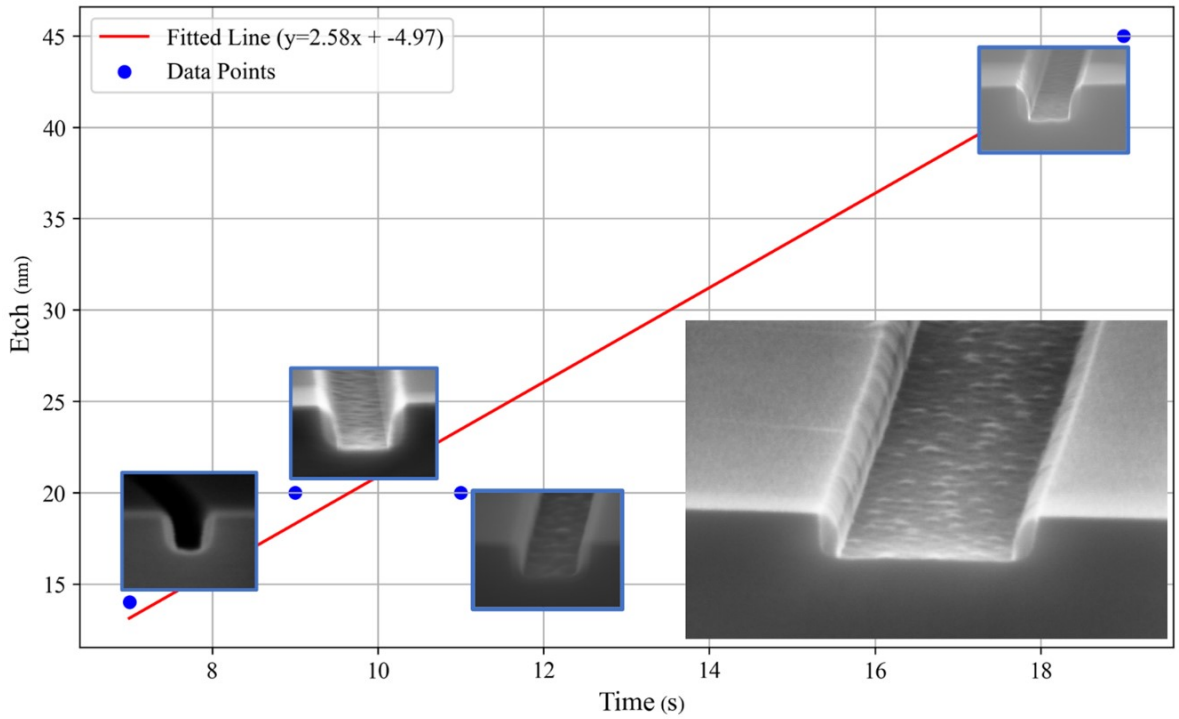

Figure 6.19: Etch rate calibration plot with an inset depicting the directional etching to remove oxide at the bottom of the holes while retaining it on the sidewalls. Machine: SPTS Advanced Plasma System (APS)

Finally, the samples are subjected to LPCVD aSi at 500°C, conformally depositing approximately 350 nm. Figure 6.20 shows a cross-sectional SEM image. One can still clearly see the ALD layer as well as the perfect void-free filling.

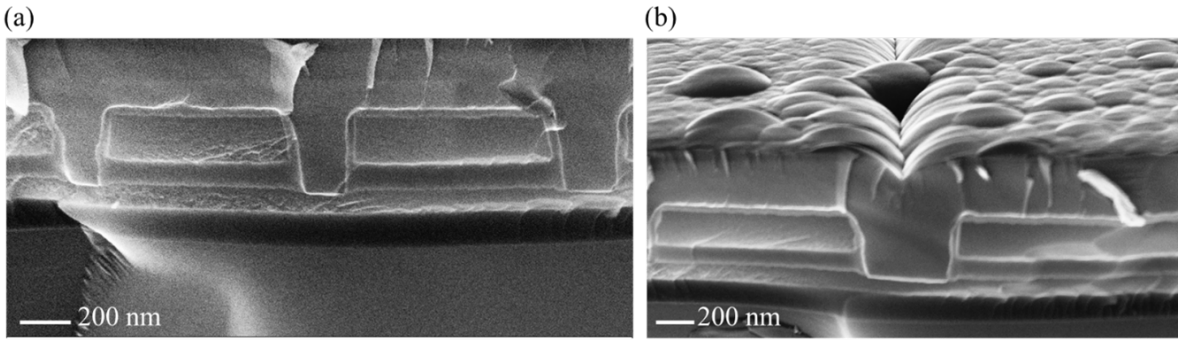

Figure 6.20: SEM cross-sections of trenches post LPCVD deposition. (a) top-down view onto cross-section, tilt angle 0°. (b) 25° tilt angle shows LPCVD dip at trench opening. Machine: Centrotherm Furnace

Following the LPCVD deposition, the material is etched back using Ion Beam Etching (IBE), based on the cross-sectional SEM measurements of the LPCVD a-Si thickness and calibrated IBE etch rates. It's at this step that the buffer SiO_2 layer is useful to avoid damaging the membrane layer if an over-etch occurs. Figure 6.21 shows a few filled membrane holes after the etch-back. One can clearly see the ALD SiO_2 layer shown here as dark rings.

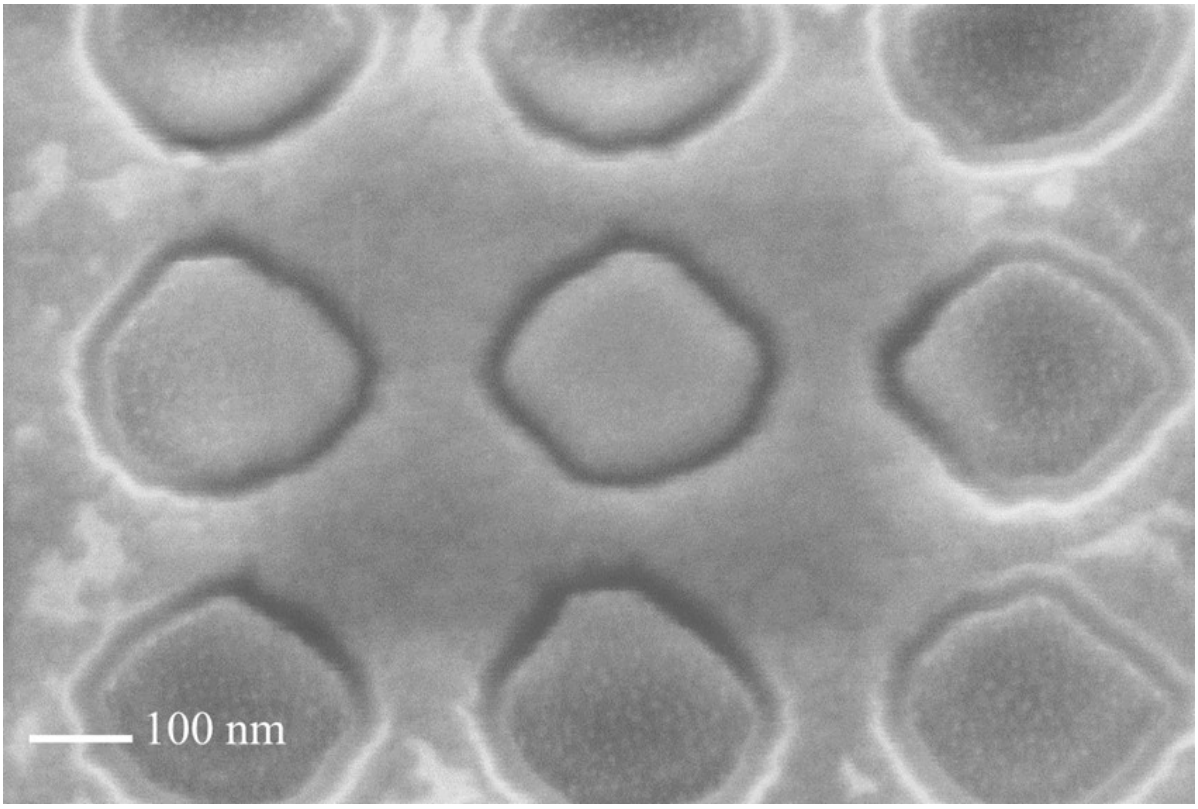

Figure 6.21: SEM image of LPCVD aSi filled membrane holes after IBE etch back. The dark ring around pillars is the thin ALD SiO_2 layer. Machine: Veeco Nexus IBE350

The MEMS device is subsequently released using HF Vapor, and the outcomes are illustrated in Figure 6.22. It is evident that the self-alignment between the pillars and the membrane has been executed successfully, clearly revealing the presence of a well-defined gap.

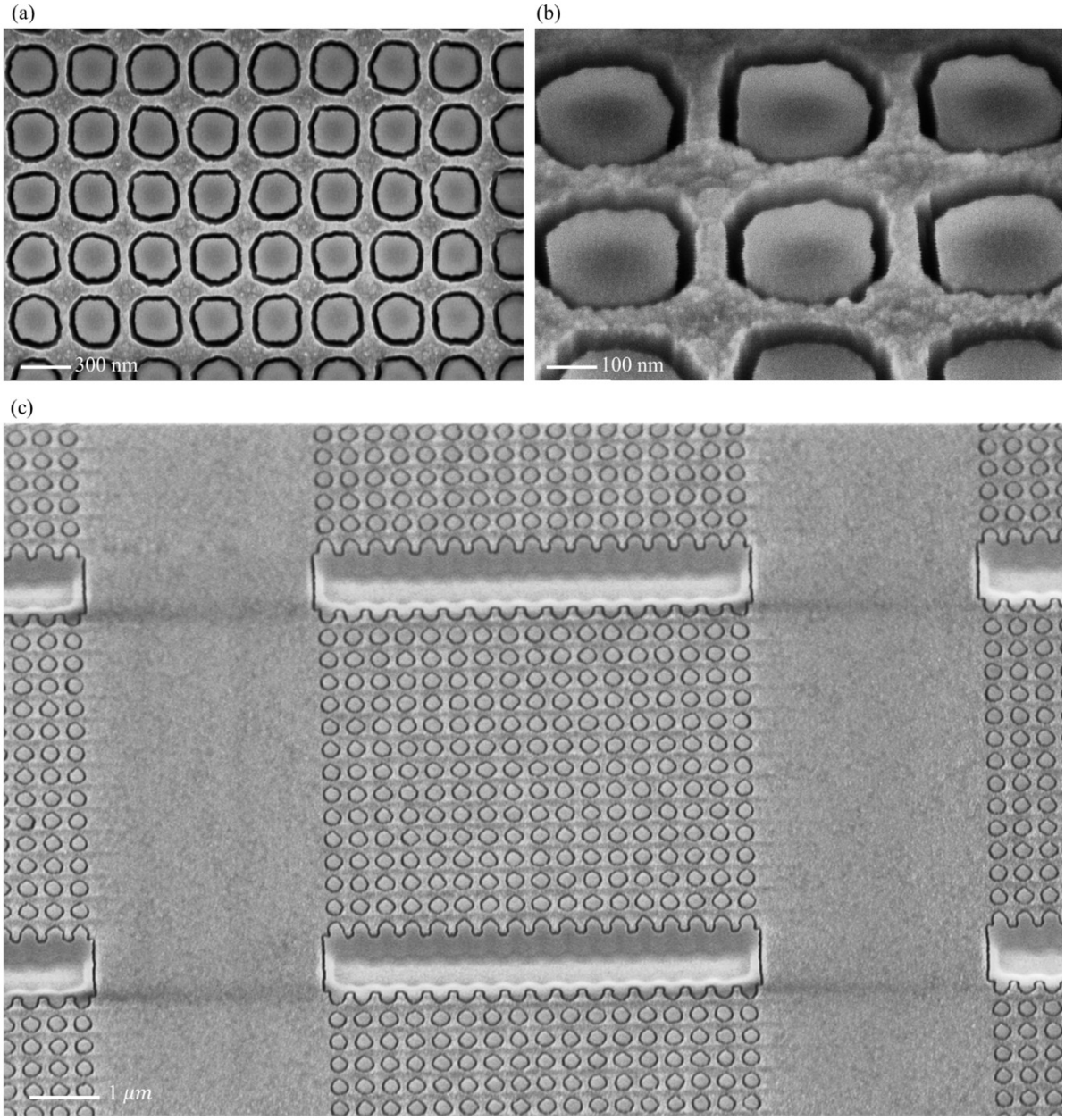

Figure 6.22: SEM images post HF vapor release. (a) top-down view, one can clearly see the gap between pillar and membrane created through the HF vapor etching of the sacrificial conformal ALD SiO_2 deposition. (b) Titled, 30°, a close up SEM image of pillars in the membrane, one can see that the membrane top and the pillar top coincide in height. (c) Pixel array showing the microbridge structures after release. Machine: SPTS uEtch

Finally, for increased conductivity of the membrane as well as improved reflectivity, a 1 nm Ti (adhesion) and a 5 nm Al layer are evaporated. Figure 6.23 provides two perspectives: a cross-sectional view (Figure 6.23a) and a top-down view (Figure 6.23b). In Figure 6.23a, the cross-sectional view of the trench filled with LPCVD aSi clearly demonstrates the successful execution of the earlier steps. The image reveals the gap opening and the removal of the sacrificial membrane-supporting SiO_2, which were crucial for achieving the desired device structure. Additionally, the robust anchoring of the LPCVD to the substrate is distinctly visible, facilitated by the successful removal of the bottom ALD SiO_2. This anchoring is vital for the structural integrity and functionality of the MEMS device. In Figure 6.23b, the top-down view of the pillars further validates the process efficacy. Small aluminum grains are visible, indicative of the Al evaporation process.

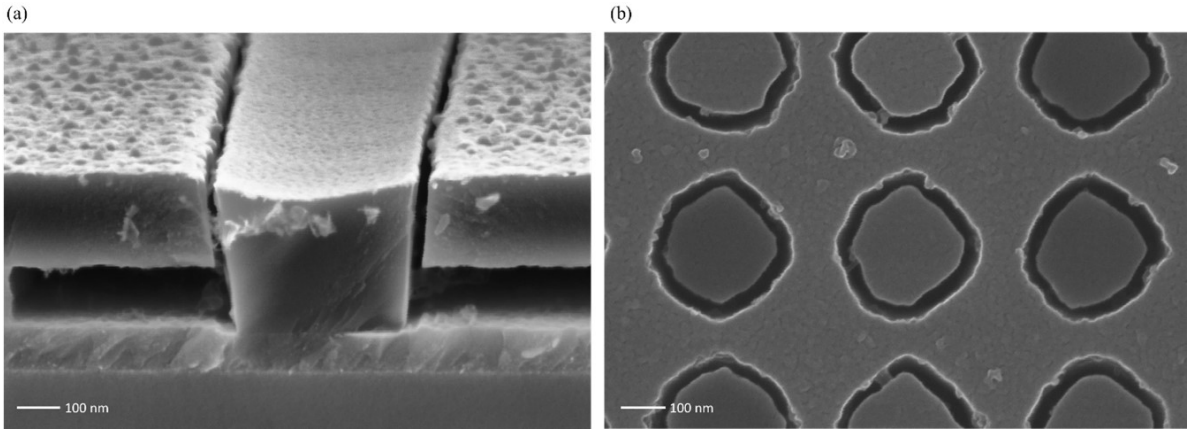

Figure 6.23: SEM images of the device following Al evaporation. (a) Cross-sectional view of the trench filled with LPCVD aSi, distinctly displaying the gap opening and the removed sacrificial membrane supporting SiO_2, along with the solid anchoring of the LPCVD to the substrate, evidencing the successful removal of the bottom ALD SiO_2. (b) Top-down view of the pillars, with small aluminum grains being visible. Machine: Leybold Optics LAB 600H

6.2.4. Characterization

Despite the apparent successful fabrication, no device showed a color change when applying voltages up to 100 V, upon which dielectric breakdown occurred, as can be seen in the two spark-induced dark spots on the microscope image in Figure 6.24. Unfortunately, the exact cause of the non-functioning is not pinpointed. The top-down resistance was measured to be roughly 83 kOhm, not extensive, but in principle sufficient to induce a voltage drop. A structural resonance characterization using Laser Doppler Vibrometry (LDV) yielded no resonance peak.

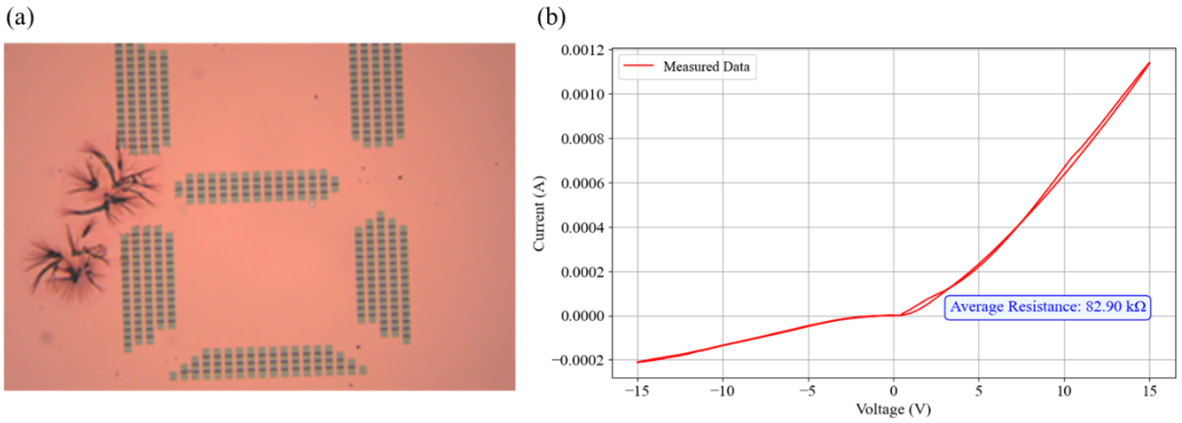

Figure 6.24: Post-fabrication characterization. (a) DC actuation did not yield any change in color, applying 100 V resulted in a break-down short circuit shown here with the two dark spots in the microscope image. (b) Current-Voltage measurement to measure average top-bottom resistance of MEMS device, reported to be 83 kOhm.

Conclusion

In summary, despite the successful fabrication of the device, the intended functionality was not achieved. Applying voltages up to 100 V did not result in the expected color change, and dielectric breakdown occurred instead, as evidenced by the two spark-induced dark spots in Figure 6.24. The precise cause of this non-functionality remains elusive. Although the top-down resistance measured approximately 83 kOhm, which should have induced a voltage drop, it did not lead to the desired outcome. Furthermore, efforts to characterize structural resonance using Laser Doppler Vibrometry (LDV) yielded no discernible results. This outcome underscores the complexity of MEMS device development and the need for further investigation to uncover the underlying issues. Despite these challenges, the fabrication process demonstrated successful self-aligned assembly of pillars into holes surrounded by a well-controlled gap.

7

Conclusion and Outlook

This thesis presents a comprehensive exploration into MEMS-based tunable metasurfaces, with the objective of modulating surface reflectivity for potential applications in reflective displays for mobile devices. The research progresses from initial static models to dynamic prototypes, culminating in insights for scalable manufacturing designs.

1. **Static Prototype and Optical Phenomena:** The initial phase involved constructing a static prototype with amorphous silicon (aSi) nanopillars and flat areas, validating the concept of variable surface reflectivity. The nanostructured areas demonstrated broad spectral light absorption within the visible spectrum, achieving a high contrast ratio of 1:50 compared to flat reflective regions. Key optical phenomena such as Mie resonances and interference effects governing the spectral response were identified.
2. **Dynamic Model and MEMS Operation:** A dynamic model was subsequently introduced, featuring electrostatic actuation to switch between absorptive and reflective states. Despite the slow switching time due to aSi's high resistivity, it successfully demonstrated a transition with a contrast ratio of 1:3 and a switching time of 54 ms. The research also addressed mechanical aspects like pull-in voltages and system dynamics.
3. **Microfabrication Techniques and Scalability:** The thesis then examined microfabrication techniques essential for scalable manufacturing. Two primary methodologies, "pillar-first" and "membrane-first," were scrutinized. The "membrane-first" approach, despite some unresolved actuation failures, showed promise for scalable production, incorporating features like self-aligned pillars.
4. **Computational Analysis and Optimization:** A significant part of the thesis involved developing a Python wrapper for commercial RCWA software, integrating advanced optimization algorithms, including machine learning techniques. This computational framework facilitated detailed analysis correlating geometric parameters with optical performance metrics.

The investigated tunable metasurface and its fabrication can be improved on multiple fronts. From a manufacturing standpoint, LPCVD deposition is not compatible with many materials, especially metals, due to its relatively high deposition temperature. This not only limits the range of materials that can be used but also poses challenges for CMOS compatibility, which is crucial for the direct backplane integration of the electrical driving unit for potential displays. High-power impulse magnetron sputtering (HiPIMS) could serve as a viable alternative for filling the membrane holes with aSi. The key advantage over conventional sputtering is the much larger fraction of ionized sputtered material, allowing for optimized step coverage [208]. Thanks to the team of Prof. Daniel Lundin from Linköping University, Sweden, a nano-trench sample was exposed to HiPIMS sputtering. The cross-sectional SEM image, depicted in Figure 7.1 and obtained after the deposition, shows promising filling percentages. For instance, the filling percentage of the trench with an aspect ratio of 1.5 is close to 60%, compared to 40% with collimators and 20% with conventional sputtering. Such a method could allow for greater material variability and better potential CMOS compatibility.

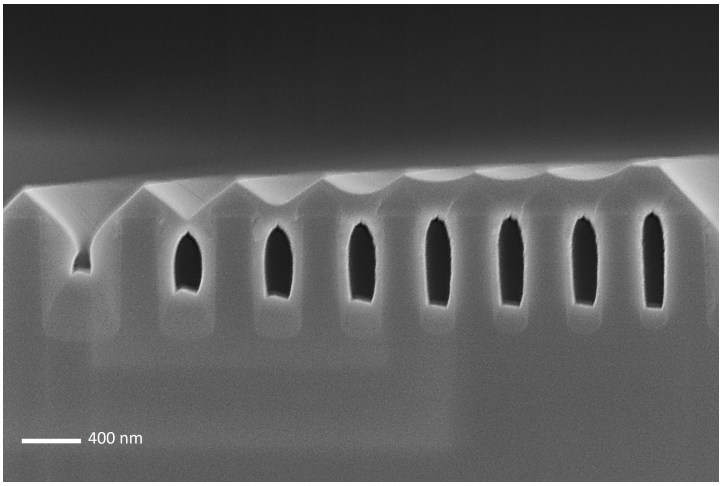

Figure 7.1: Cross-sectional SEM image illustrating nanoscale trenches of 851 nm height with varying widths and their corresponding filling levels. Trenches widths of 553 nm, 420 nm, 331 nm, 327 nm, 288 nm, 245 nm, 263 nm, and 226 nm are displayed. The associated filling ratios are 60%, 40%, 36%, 30%, 25%, 21%, 24%, and 18% respectively.

In terms of geometry, there are three further venues to explore. Pillar arrangement does have an impact on the far field reflection. Moving from a rectangular arrangement to a hexagonal arrangement could slightly improve the optical response, since a hexagonal arrangement provides a more isotropic response in the plane, compared to a rectangular arrangement. Furthermore, in terms of period, the present thesis has mostly focused on a period of 400 nm. This value was selected as the largest possible period without the introduction of diffraction ordered. The focus is on the visible spectrum of light, which ranges from approximately 400 nm to 700 nm. According to the grating equation $m\lambda = d\,(\sin\theta_i + \sin\theta_m)$, where m is the order of diffraction, λ is the wavelength, d is the period and θ_i and θ_m are the incident and diffracted angles, respectively, a period smaller than the shortest wavelength in the visible range ensures that only the 0^{th} order of diffraction occurs for all visible wavelengths. This eliminates the need to consider higher-order diffraction phenomena, thereby simplifying both simulation and interpretation of the optical properties of the structure. However, as shown in the static prototype (see chapter 4) very dark states are also achievable with larger periods. The main benefit of larger periods lies in the fact that it would allow for relaxed fabrication constraints. Thus, in the pursuit of developing displays that achieve true black, diffractive optical elements present both an opportunity and a challenge. While these elements can be engineered to minimize reflection at specific angles, the inherent diffractive nature of these structures leads to reflection orders that can emerge at other, non-normal angles. This phenomenon poses a particular challenge: How can one ensure that the display appears uniformly dark from multiple viewing angles? To address this issue, it is proposed to undertake a comprehensive simulation-based analysis. The objective would be to map the angular brightness distribution of the structure by calculating the diffraction patterns for a broad range of incident light angles. By quantifying the maximum reflection, a viewer could experience over all angles, a threshold can be defined below which the reflection is considered to be 'dark' or 'black'. This rigorous, threshold-based evaluation allows for an informed, objective assessment of the display's performance across varying conditions of illumination and observation. Adopting such a simulation framework can significantly aid in the optimization and engineering of diffractive structures that both allow for larger structures to be fabricated, thus relaxing fabrication constraints, while providing good optical performance at all orders. Next to the pillar arrangement and the period, there is a third variable that might be worth of further investigation: the shape of the pillar. Specifically, due to the self-aligned process flow, pillar base shapes beyond a simple circle are possible. This can potentially lead to higher absorption and/or increased angle insensitivity[209].

To summarize, this thesis provides a comprehensive investigation into the design, fabrication, and characterization of a MEMS-based tunable metasurface based on tunable surface morphology, with potential applications in reflective displays. It presents a scalable manufacturing process, substantiated by experimental data, and includes a significant computational component that aids in design

optimization. The results indicate promising avenues for future work, particularly in the areas of material science, fabrication techniques, and computational methods. While challenges remain in achieving faster switching times, CMOS compatibility, and better optical performances, the groundwork laid by this thesis forms a robust platform for future innovations in tunable MEMS-based metasurface technology. In addition to the avenues for future work already identified, it is essential to address the aspect of optical packaging. The development of effective optical packaging solutions will be crucial to enhance the practical applicability and durability of the MEMS-based tunable metasurfaces, ensuring that they meet the demands of real-world applications.

References

[1] David H Foster. “Color constancy”. In: *Vision research* 51.7 (2011), pp. 674–700.

[2] Masanobu Iwanaga. “All-dielectric metasurface fluorescence biosensors for high-sensitivity antibody/antigen detection”. In: *ACS nano* 14.12 (2020), pp. 17458–17467.

[3] Mohammadreza Khorasaninejad et al. “Polarization-insensitive metalenses at visible wavelengths”. In: *Nano letters* 16.11 (2016), pp. 7229–7234.

[4] Zhengji Xu et al. “CMOS-compatible all-Si metasurface polarizing bandpass filters on 12-inch wafers”. In: *Optics Express* 27.18 (2019), pp. 26060–26069.

[5] Yusuke Nagasaki et al. “Metal-masked mie-resonant full-color printing for achieving free-space resolution limit”. In: *ACS Photonics* 5.9 (2018), pp. 3849–3855.

[6] Chun-Chieh Chang et al. “Invited Article: Narrowband terahertz bandpass filters employing stacked bilayer metasurface antireflection structures”. In: *Apl Photonics* 3.5 (2018).

[7] Jie Hu et al. “A review on metasurface: from principle to smart metadevices”. In: *Frontiers in Physics* 8 (2021), p. 586087.

[8] Pierre Berini. “Optical beam steering using tunable metasurfaces”. In: *ACS Photonics* 9.7 (2022), pp. 2204–2218.

[9] Sergey Lepeshov and Alex Krasnok. “Tunable phase-change metasurfaces”. In: *Nature Nanotechnology* 16.6 (2021), pp. 615–616.

[10] Guixin Li, Shuang Zhang, and Thomas Zentgraf. “Nonlinear photonic metasurfaces”. In: *Nature Reviews Materials* 2.5 (2017), pp. 1–14.

[11] James A Dolan et al. “Broadband liquid crystal tunable metasurfaces in the visible: liquid crystal inhomogeneities across the metasurface parameter space”. In: *Acs Photonics* 8.2 (2021), pp. 567–575.

[12] Sumeet Walia et al. “Flexible metasurfaces and metamaterials: A review of materials and fabrication processes at micro-and nano-scales”. In: *Applied Physics Reviews* 2.1 (2015).

[13] Shaowei He et al. “Recent advances in MEMS metasurfaces and their applications on tunable lens”. In: *Micromachines* 10.8 (2019), p. 505.

[14] Xiaogang Liu et al. “Black silicon: fabrication methods, properties and solar energy applications”. In: *Energy & Environmental Science* 7.10 (2014), pp. 3223–3263.

[15] Renat R Bilyalov et al. “Use of porous silicon antireflection coating in multicrystalline silicon solar cell processing”. In: *IEEE Transactions on electron devices* 46.10 (1999), pp. 2035–2040.

[16] Jihun Oh et al. “Nanoporous black silicon photocathode for H 2 production by photoelectrochemical water splitting”. In: *Energy & Environmental Science* 4.5 (2011), pp. 1690–1694.

[17] Zhihong Huang et al. “Microstructured silicon photodetector”. In: *Applied Physics Letters* 89.3 (2006).

[18] Gustav Mie. “Beiträge zur Optik trüber Medien, speziell kolloidaler Metallösungen”. In: *Annalen der Physik* 25.3 (1908), pp. 377–445. DOI: 10.1002/andp.19083300302. URL: https://onlinelibrary.wiley.com/doi/abs/10.1002/andp.19083300302.

[19] P Spinelli, MA Verschuuren, and A Polman. “Broadband omnidirectional antireflection coating based on subwavelength surface Mie resonators”. In: *Nature communications* 3.1 (2012), p. 692.

[20] Lord Rayleigh. “III. Note on the remarkable case of diffraction spectra described by Prof. Wood”. In: *The London, Edinburgh, and Dublin Philosophical Magazine and Journal of Science* 14.79 (1907), pp. 60–65.

[21] AA Maradudin et al. “Rayleigh and Wood anomalies in the diffraction of light from a perfectly conducting reflection grating”. In: *Journal of Optics* 18.2 (2016), p. 024004.

[22] S. A. Boden and D. M. Bagnall. “Tunable reflection minima of nanostructured antireflective surfaces”. In: *Applied Physics Letters* 93.13 (Sept. 30, 2008), p. 133108. ISSN: 0003-6951. DOI: 10.1063/1.2993231. URL: https://doi.org/10.1063/1.2993231 (visited on 10/02/2023).

[23] Blayne M. Phillips, Peng Jiang, and Bin Jiang. “Biomimetic broadband antireflection gratings on solar-grade multicrystalline silicon wafers”. In: *Applied Physics Letters* 99.19 (Nov. 9, 2011), p. 191103. ISSN: 0003-6951. DOI: 10.1063/1.3660263. URL: https://doi.org/10.1063/1.3660263 (visited on 10/02/2023).

[24] Teresa Goodman. “Overview of the Photometric Characterization of Visual Displays”. In: *Handbook of Visual Display Technology*. Ed. by Janglin Chen, Wayne Cranton, and Mark Fihn. Cham: Springer International Publishing, 2016, pp. 337–350. ISBN: 978-3-319-14346-0. DOI: 10.1007/978-3-319-14346-0_21.

[25] [Author] Hertel. “Evaluating Display Reflections in Reflective Displays and Beyond”. In: *Information Display* 2020 (2020). [doi:10.1002/msid.1099]. URL: https://sid.onlinelibrary.wiley.com/doi/full/10.1002/msid.1099.

[26] DisplayMate. *Tablet and Smartphone Displays Under Bright Ambient Lighting Shoot-Out*. Accessed: Jun. 05, 2023. 2023. URL: https://www.displaymate.com/Mobile_Brightness_ShootOut_2.htm.

[27] H. Chen, G. Tan, and S.-T. Wu. “Ambient contrast ratio of LCDs and OLED displays”. In: *Optics Express* 25.26 (Dec. 2017). [doi:10.1364/OE.25.033643], pp. 33643–33656.

[28] Ranbir Singh et al. “Improving the contrast ratio of OLED displays: An analysis of various techniques”. In: *Optical Materials* 34.4 (Feb. 2012). [doi:10.1016/j.optmat.2011.10.005], pp. 716–723. URL: https://doi.org/10.1016%2Fj.optmat.2011.10.005.

[29] M. Miles et al. “Digital Paper™ for reflective displays”. In: *Journal of the Society for Information Display* 11.1 (Mar. 2003). [doi:10.1889/1.1831708], pp. 209–215. URL: https://doi.org/10.1889%2F1.1831708.

[30] Jason Heikenfeld et al. “Review Paper: A critical review of the present and future prospects for electronic paper”. In: *Journal of the Society for Information Display* 19.2 (2011), p. 129. DOI: 10.1889/jsid19.2.129.

[31] Guisong Yang et al. “Design, Fabrication and Measurement of Full-Color Reflective Electrowetting Displays”. In: *Micromachines* 13.11 (Nov. 2022). [doi:10.3390/mi13112034], p. 2034. URL: https://doi.org/10.3390%2Fmi13112034.

[32] M. E. Howard et al. “Gyricon electric paper”. In: *Journal of the Society for Information Display* 6.4 (1998). [doi:10.1889/1.1985241], p. 215. URL: https://doi.org/10.1889%2F1.1985241.

[33] ALAN Sobel. “Current display research-A survey”. In: *1977 International Electron Devices Meeting*. IEEE. 1977, pp. 64–68.

[34] Dhananjay K. Deshmukh, Jayant Nirmalkar, and Mozammel Haque. “Tb3 Activated High-Color-Rendering Green Light Yttrium Oxyorthosilicates Phosphors for Display Device Application”. In: (Nov. 2020). [doi:10.1201/9780429025334-1], pp. 1–12. URL: https://doi.org/10.1201%2F9780429025334-1.

[35] Barrett Comiskey et al. “An electrophoretic ink for all-printed reflective electronic displays”. In: *Nature* 394.6690 (July 1998). [doi:10.1038/28349], pp. 253–255. URL: https://doi.org/10.1038%2F28349.

[36] Robert J. Fleming. “Fast-Switching Mode with CLEARInk Structure”. In: *E□Paper Displays*. [doi:10.1002/9781119745624.ch4]. John Wiley Sons, Ltd, 2022. Chap. 4, pp. 75–98. ISBN: 9781119745624. DOI: https://doi.org/10.1002/9781119745624.ch4. eprint: https://onlinelibrary.wiley.com/doi/pdf/10.1002/9781119745624.ch4. URL: https://onlinelibrary.wiley.com/doi/abs/10.1002/9781119745624.ch4.

[37] Han-Lim Kang et al. “Analysis of Particle Movement by Dielectrophoretic Force for Reflective Electronic Display”. In: *Journal of Display Technology* 12.7 (July 2016), pp. 747–752. DOI: 10.1109/jdt.2016.2524023. URL: https://doi.org/10.1109%2Fjdt.2016.2524023.

[38] Thomas Whitesides et al. “10.2: Towards Video-rate Microencapsulated Dual-Particle Electrophoretic Displays”. In: *SID Symposium Digest of Technical Papers*. Vol. 35. 1. Wiley Online Library. 2004, pp. 133–135.

[39] *E Ink*. en. Page Version ID: 1157073256. May 2023. URL: https://en.wikipedia.org/w/index.php?title=E_Ink&oldid=1157073256 (visited on 09/22/2023).

[40] bfishadow. *English: Kindle Voyage with origami cover.* Dec. 2014. URL: https://commons.wikimedia.org/wiki/File:Kindle_Voyage_with_cover.jpg (visited on 12/23/2023).

[41] Ming Wang et al. “Electrophoretic display device”. en. US9557623B2. Jan. 2017. URL: https://patents.google.com/patent/US9557623B2/en?oq=US9557623B2+-+Electrophoretic+display+device+ (visited on 09/22/2023).

[42] Hui Du, Haiyan Gu, and Xiaojia Wang. “Silane-containing pigment particles for electrophoretic display”. en. US20120313049A1. Dec. 2012. URL: https://patents.google.com/patent/US20120313049/en?oq=2012-0313049 (visited on 09/22/2023).

[43] G. Seth Roberts et al. “Electrostatic Charging of Nonpolar Colloids by Reverse Micelles”. In: *Langmuir* 24.13 (June 2008). [doi:10.1021/la703908n], pp. 6530–6541. URL: https://doi.org/10.1021%2Fla703908n.

[44] Jonathan Albert et al. “Encapsulated electrophoretic displays having a monolayer of capsules and materials and methods for making the same”. en. US20030137717A1. July 2003. URL: https://patents.google.com/patent/US20030137717/en (visited on 05/09/2023).

[45] Richard M. Webber. “10.4: Image Stability in Active-Matrix Microencapsulated Electrophoretic Displays”. In: *SID Symposium Digest of Technical Papers* 33.1 (2002). [doi:10.1889/1.1830177], p. 126. URL: https://doi.org/10.1889%2F1.1830177.

[46] Mark T. Johnson et al. “High-quality images on electrophoretic displays”. In: *Journal of the Society for Information Display* 14.2 (2006). [doi:10.1889/1.2176120], p. 175. URL: https://doi.org/10.1889%2F1.2176120.

[47] Theodore A. Sjodin. “Methods for driving electro-optic displays”. en. US9672766B2. June 2017. URL: https://patents.google.com/patent/US9672766/en (visited on 09/22/2023).

[48] Lan Cao et al. “Electrophoretic media with improved binder”. en. WO2007050686A2. May 2007. URL: https://patents.google.com/patent/WO2007050686A2/en (visited on 09/22/2023).

[49] Russell J. Wilcox et al. “Electro-optic displays with reduced remnant voltage”. en. US8558783B2. 2013. URL: https://patents.google.com/patent/US8558783B2/en (visited on 09/22/2023).

[50] A. Bouchard et al. “68.5L: Late-News Paper: Advances in Active-Matrix Color Displays Using Electrophoretic Ink and Color Filters”. In: *SID Symposium Digest of Technical Papers* 37.1 (2006). [doi:10.1889/1.2433429], p. 1934. URL: https://doi.org/10.1889%2F1.2433429.

[51] Edzer Huitema and Ian French. “E Ink’s Technicolor Moment: The Road to Color E-Paper Took Two Decades”. In: *IEEE Spectrum* 59.2 (Feb. 2022). [doi:10.1109/mspec.2022.9706404], pp. 30–35. URL: https://doi.org/10.1109%2Fmspec.2022.9706404.

[52] Dirk Hertel et al. “39-1: iDistinguished Paper:/i Gamut Rings of Reflective ePaper Displays with Combined Frontlight and Ambient Illumination”. In: *SID Symposium Digest of Technical Papers* 53.1 (June 2022). [doi:10.1002/sdtp.15528], pp. 485–488. URL: https://doi.org/10.1002%2Fsdtp.15528.

[53] *E INK Gallery 3 vs E INK Kaleido 3 Color E-Paper - Good e-Reader*. URL: https://goodereader.com/blog/e-paper/e-ink-gallery-3-vs-e-ink-kaleido-3 (visited on 09/22/2023).

[54] Chia-Ming Chang, Chih-Hsuan Chiu, and Yuh-Zheng Lee. “P-117: Direct Printed Plastic Color Filter for Color Electrophoretic Displays”. In: *SID Symposium Digest of Technical Papers* 42.1 (June 2011). [doi:10.1889/1.3621156], pp. 1545–1547. URL: https://doi.org/10.1889%2F1.3621156.

[55] Yen-Huei Lai et al. “P-148L:iLate-News Poster/i: Direct Photolithographic Color Filter for 14.1-inch Flexible Color Electrophoretic Displays”. In: *SID Symposium Digest of Technical Papers* 43.1 (June 2012). [doi:10.1002/j.2168-0159.2012.tb06058.x], pp. 1365–1367. URL: https://doi.org/10.1002%2Fj.2168-0159.2012.tb06058.x.

[56] Keiichi Akamatsu et al. “16.3: A 13-inch Flexible Color EPD Driven by Low-Temperature a-Si TFTs”. In: *SID Symposium Digest of Technical Papers* 42.1 (June 2011). [doi:10.1889/1.3621269], pp. 198–201. URL: https://doi.org/10.1889%2F1.3621269.

[57] Hui Du and HongMei Zang. “Color display device”. U.S. pat. 9285649B2. E Ink California LLC. Mar. 15, 2016. URL: https://patents.google.com/patent/US9285649B2/en (visited on 09/22/2023).

[58] “The positive, negative, photo-ER, and electromagnetorheological (EMR) effects”. In: *Studies in Interface Science*. Elsevier, 2005, pp. 83–113. DOI: 10.1016/s1383-7303(05)80018-3. URL: https://doi.org/10.1016/s1383-7303(05)80018-3.

[59] Pengfei Bai, Zichuan Yi, and Guofu Zhou. “An Improved Driving Scheme in an Electrophoretic Display”. In: *International Journal of Engineering and Technology* 3.4 (2013).

[60] Zhenxing Wang and Zhongyuan Liu. *The key technology of ereader based on electrophoretic display*. [doi:10.1109/icste.2010.5608873]. IEEE, Oct. 2010. URL: https://doi.org/10.1109%2Ficste.2010.5608873.

[61] *Physics of electrorheological fluids*. [doi:10.1016/s1383-7303(05)80021-3]. Elsevier, 2005, pp. 235–340. URL: https://doi.org/10.1016%2Fs1383-7303%2805%2980021-3.

[62] Ya-Di Zhang et al. “Backflow Effect Enabling Fast Response and Low Driving Voltage of Electrophoretic E-ink Dispersion by Liquid Crystal Additives”. In: *Scientific Reports* 9.1 (Sept. 2019). [doi:10.1038/s41598-019-50382-y]. URL: https://doi.org/10.1038%2Fs41598-019-50382-y.

[63] R.H. Laughlin and T.G. Hazelton. “Frustrated total internal reflection: An alternative for optical cross-connect architectures”. In: *Conference Proceedings. LEOS’98. 11th Annual Meeting. IEEE Lasers and Electro-Optics Society 1998 Annual Meeting*. Conference held in Orlando, FL, USA, December 1-4, 1998. IEEE. DOI: 10.1109/leos.1998.739516. URL: https://doi.org/10.1109/leos.1998.739516.

[64] Michele A. Mossman, Lorne A. Whitehead, and S. P. Rao. “P-83: Grey Scale Control of TIR Using Electrophoresis of Sub-Optical Pigment Particles”. In: *SID Symposium Digest of Technical Papers* 33.1 (2002). [doi:10.1889/1.1830848], p. 522. URL: https://doi.org/10.1889%2F1.1830848.

[65] Michele A. Mossman, Vincent H. Kwong, and Lorne A. Whitehead. “A novel reflective image display using total internal reflection”. In: *Displays* 25.5 (Dec. 2004). [doi:10.1016/j.displa.2004.09.020], pp. 215–221. URL: https://doi.org/10.1016%2Fj.displa.2004.09.020.

[66] Lorne Whitehead. “Total internal reflection for illumination and displays”. In: *SPIE Newsroom* (2006). [doi:10.1117/2.1200611.0461]. URL: https://doi.org/10.1117%2F2.1200611.0461.

[67] Robert Fleming et al. “36-3: Tablet-size eTIR Display for Low-power ePaper Applications with Color Video Capability”. In: *SID Symposium Digest of Technical Papers* 50.1 (May 2019). [doi:10.1002/sdtp.12967], pp. 505–508. URL: https://doi.org/10.1002%2Fsdtp.12967.

[68] Wenyao He et al. “Driving Waveform Design of Electrophoretic Display Based on Optimized Particle Activation for a Rapid Response Speed”. In: *Micromachines* 11.5 (May 2020), p. 498. DOI: 10.3390/mi11050498. URL: https://doi.org/10.3390/mi11050498.

[69] Hiroshi Kawamoto. “The history of liquid-crystal displays”. In: *Proceedings of the IEEE* 90.4 (2002). [doi:10.1109/JPROC.2002.1002521], pp. 460–500.

[70] W. D. Helfrich and M. D. Schadt. “Lichtsteuerzelle”. U.S. pat. Swiss Patent CH532261A. Hoffmann La Roche. Dec. 31, 1972. URL: https://worldwide.espacenet.com/patent/search/family/004429210/publication/CH532261A?q=pn%3DCH532261A.

[71] D.-K. Yang et al. “Control of reflectivity and bistability in displays using cholesteric liquid crystals”. In: *Journal of Applied Physics* 76.2 (July 1994). [doi:10.1063/1.358518], pp. 1331–1333. URL: https://doi.org/10.1063%2F1.358518.

[72] M. Schadt and W. Helfrich. “VOLTAGE-DEPENDENT OPTICAL ACTIVITY OF A TWISTED NEMATIC LIQUID CRYSTAL”. In: *Applied Physics Letters* 18.4 (Feb. 1971). [doi:10.1063/1.1653593], pp. 127–128. URL: https://doi.org/10.1063%2F1.1653593.

[73] Martin Schadt. “How we made the liquid crystal display”. In: *Nature Electronics* 1.8 (Aug. 2018). [doi:10.1038/s41928-018-0119-8], pp. 481–481. URL: https://doi.org/10.1038%2Fs41928-018-0119-8.

[74] Yoshiharu Nakajima et al. “22.4: Invited Paper: Ultra-Low-Power LTPS TFT-LCD Technology Using a Multi-Bit Pixel Memory Circuit”. In: *SID Symposium Digest of Technical Papers* 37.1 (2006). [doi:10.1889/1.2451410], p. 1185. URL: https://doi.org/10.1889%2F1.2451410.

[75] Masaya Tamaki et al. “A memory-in-pixel reflective-type LCD using newly designed system and pixel structure”. In: *Journal of the Society for Information Display* 22.5 (May 2014). [doi:10.1002/jsid.245], pp. 251–259. URL: https://doi.org/10.1002%2Fjsid.245.

[76] Sharp Kabushiki Kaisha. “Thin-film electroluminescent panel”. In: *Displays* 15.3 (July 1994). [doi:10.1016/0141-9382(94)90012-4], p. 194. URL: https://doi.org/10.1016%2F0141-9382%2894%2990012-4.

[77] G. Friedel. “Les états mésomorphes de la matière”. In: *Annales de Physique* 9.18 (1922). [doi:10.1051/anphys/192209180273], pp. 273–474. URL: https://doi.org/10.1051%2Fanphys%2F192209180273.

[78] H. Kelker. “History of Liquid Crystals”. In: *Molecular Crystals and Liquid Crystals* 21.1-2 (Jan. 1973). [doi:10.1080/15421407308083312], pp. 1–48. URL: https://doi.org/10.1080%2F15421407308083312.

[79] Michel Mitov. “Cholesteric liquid crystals in living matter”. In: *Soft Matter* 13.23 (2017). [doi:10.1039/c7sm00384f], pp. 4176–4209. URL: https://doi.org/10.1039%2Fc7sm00384f.

[80] Michel Mitov. “Cholesteric Liquid Crystals with a Broad Light Reflection Band”. In: *Advanced Materials* 24.47 (Oct. 2012). [doi:10.1002/adma.201202913], pp. 6260–6276. URL: https://doi.org/10.1002%2Fadma.201202913.

[81] Pierre-Gilles De Gennes and Jacques Prost. *The physics of liquid crystals*. 83. Oxford university press, 1993.

[82] Asad Khan et al. “27.4: Super High Brightness Reflective Cholesteric Display”. In: *SID Symposium Digest of Technical Papers* 32.1 (2001). [doi:10.1889/1.1831896], p. 460. URL: https://doi.org/10.1889%2F1.1831896.

[83] Deng-Ke Yang, Xiao-Yang Huang, and Yang-Ming Zhu. “BISTABLE CHOLESTERIC REFLECTIVE DISPLAYS: Materials and Drive Schemes”. In: *Annual Review of Materials Science* 27.1 (Aug. 1997). [doi:10.1146/annurev.matsci.27.1.117], pp. 117–146. URL: https://doi.org/10.1146%2Fannurev.matsci.27.1.117.

[84] *Eye Care - AUO*. URL: https://auo.com/en-global/technologies/index/Display/Eye_Care/ChLCD#lv3AnchorBlock (visited on 09/26/2023).

[85] Tod Schneider et al. “UV Cured Flexible Cholesteric Liquid Crystal Displays”. In: *Radtech UV&EB Curing Technology, Technical Conference Proceedings May*. 2008, pp. 4–7.

[86] David Coates. “Cholesteric Reflective Displays”. In: *Handbook of Visual Display Technology*. [doi:10.1007/978-3-319-14346-0$_93$]. Springer International Publishing, 2016, pp. 2199–2222. URL: https://doi.org/10.1007%2F978-3-319-14346-0_93.

[87] Arne A. F. Froyen et al. “Electrothermal Color Tuning of Cholesteric Liquid Crystals Using Interdigitated Electrode Patterns”. In: *Advanced Electronic Materials* 7.2 (Dec. 2020). [doi:10.1002/aelm.202000958]. URL: https://doi.org/10.1002%2Faelm.202000958.

[88] Yuhua Huang et al. “Tuning the photonic band gap in cholesteric liquid crystals by temperature-dependent dopant solubility”. In: *Optics Express* 14.3 (2006). [doi:10.1364/oe.14.001236], p. 1236. URL: https://doi.org/10.1364%2Foe.14.001236.

[89] Martin Schadt. “LIQUID CRYSTAL MATERIALS AND LIQUID CRYSTAL DISPLAYS”. In: *Annual Review of Materials Science* 27.1 (Aug. 1997). [doi:10.1146/annurev.matsci.27.1.305], pp. 305–379. URL: https://doi.org/10.1146%2Fannurev.matsci.27.1.305.

[90] Tatsuo Uchida and Takahiro Ishinabe. “Reflective Liquid-Crystal Displays”. In: *MRS Bulletin* 27.11 (Nov. 2002). [doi:10.1557/mrs2002.276], pp. 876–879. URL: https://doi.org/10.1557%2Fmrs2002.276.

[91] Kent Displays Incorporated. *Kent_Display_Datasheet_VGA Cholesteric Display Modules and Controller Assemblies*. URL: https://www.datasheetarchive.com/datasheet?id=21442d9816515db270cebc0a1ea27ecf1f37bd&type=P&term=kent%2520display (visited on 08/10/2023).

[92] Yuzuru Takashima and Brandon Hellman. “Review paper: imaging lidar by digital micromirror device”. In: *Optical Review* 27.5 (Sept. 2020). [doi:10.1007/s10043-020-00620-w], pp. 400–408. URL: https://doi.org/10.1007%2Fs10043-020-00620-w.

[93] Timothy Brosnihan et al. “Pixtronix digital micro-shutter display technology: a MEMS display for low power mobile multimedia displays”. In: *MOEMS and Miniaturized Systems IX*. Vol. 7594. SPIE. 2010, pp. 66–74.

[94] M. W. Miles. “A new reflective FPD technology using interferometric modulation”. In: *Journal of the Society for Information Display* 5.4 (1997). [doi:10.1889/1.1985183], p. 379. URL: https://doi.org/10.1889%2F1.1985183.

[95] Mark W. Miles. “MEMS devices with stiction bumps”. en. US7554711B2. June 2009. URL: https://patents.google.com/patent/US7554711/en?oq=20060262380 (visited on 10/15/2022).

[96] M. W. Miles. “5.3: Digital Paper™: Reflective Displays Using Interferometric Modulation”. In: *SID Symposium Digest of Technical Papers* 31.1 (May 2000). [doi:10.1889/1.1832950], pp. 32–35. URL: https://doi.org/10.1889%2F1.1832950.

[97] writegirl. *Mirasol eReader Screen by Qualcomm @ CES*. Jan. 2010. URL: https://www.flickr.com/photos/writegirl/4267311022/ (visited on 12/23/2023).

[98] Manish Kothari. “Method and device for compensating for color shift as a function of angle of view”. en. EP1640314A2. Mar. 2006. URL: https://patents.google.com/patent/EP1640314A2/en (visited on 10/15/2022).

[99] John Hong et al. “Continuous color reflective displays using interferometric absorption”. In: *Optica* 2.7 (June 2015). [doi:10.1364/optica.2.000589], p. 589. URL: https://doi.org/10.1364%2Foptica.2.000589.

[100] Mark W. Miles. “MEMS-based interferometric modulator for display applications”. In: *SPIE Proceedings*. Ed. by Patrick J. French and Eric Peeters. [doi:10.1117/12.360483]. SPIE, Aug. 1999. URL: https://doi.org/10.1117%2F12.360483.

[101] Edward K. Chan et al. “Continuous Color Reflective Display Fabricated in Integrated MEMS-and-TFT-on-Glass Process”. In: *Journal of Microelectromechanical Systems* 26.1 (Feb. 2017). [doi:10.1109/JMEMS.2016.2621119], pp. 143–157. URL: https://doi.org/10.1109%2Fjmems.2016.2621119.

[102] Santiago J. Cartamil-Bueno et al. “Graphene mechanical pixels for Interferometric Modulator Displays”. In: *Nature Communications* 9.1 (Nov. 2018). [doi:10.1038/s41467-018-07230-w]. URL: https://doi.org/10.1038%2Fs41467-018-07230-w.

[103] Brian Gally et al. “5.1: Invited Paper: A 5.7 Color Mirasol® XGA Display For High Performance Applications”. In: *SID Symposium Digest of Technical Papers* 42.1 (June 2011). [doi:10.1889/1.3621326], pp. 36–39. URL: https://doi.org/10.1889%2F1.3621326.

[104] R. Vuilleumier et al. “Bulletin Annuel Societe Suisse de Chronometrie”. In: *Bulletin Annuel Societe Suisse de Chronometrie* 12 (1983), pp. 37–40.

[105] Fabio Jutzi et al. “Low voltage electrostatic 90&amp#x00B0 turning flap for reflective MEMS display”. In: *2010 International Conference on Optical MEMS and Nanophotonics*. [doi:10.1109/omems.2010.5672177]. IEEE, Aug. 2010. URL: https://doi.org/10.1109%2Fomems.2010.5672177.

[106] Fabio Jutzi, Wilfried Noell, and Nico F. de Rooij. “Vertical electrostatically 90° turning flaps for reflective MEMS display”. In: *SPIE Proceedings*. Ed. by Harald Schenk and Wibool Piyawattanametha. [doi:10.1117/12.873840]. SPIE, Feb. 2011. URL: https://doi.org/10.1117%2F12.873840.

[107] Sung Kwon Cho, Hyejin Moon, and Chang-Jin Kim. “Creating, transporting, cutting, and merging liquid droplets by electrowetting-based actuation for digital microfluidic circuits”. In: *Journal of Microelectromechanical Systems* 12.1 (Feb. 2003). [doi:10.1109/jmems.2002.807467], pp. 70–80. URL: https://doi.org/10.1109%2Fjmems.2002.807467.

[108] Jia Li et al. “Current commercialization status of electrowetting-on-dielectric (EWOD) digital microfluidics”. In: *Lab on a Chip* 20.10 (2020), pp. 1705–1712.

[109] Bokke Johannes Feenstra, Robert Andrew Hayes, and Menno Willem Jose Prins. “Display device”. en. US7898718B2. Mar. 2011. URL: https://patents.google.com/patent/US7898718B2/en?oq=B.+J.+Feenstra%2c+R.+A.+Hayes+and+M.+W.+J.+Prins%2c+Display+device%2c+U.S.+Pat.%2c+7898718%2c+2011%2c+ (visited on 03/12/2023).

[110] Robert A. Hayes and B. J. Feenstra. “Video-speed electronic paper based on electrowetting”. In: *Nature* 425.6956 (Sept. 2003). [doi:10.1038/nature01988], pp. 383–385. URL: https://doi.org/10.1038%2Fnature01988.

[111] Frieder Mugele and Jean-Christophe Baret. “Electrowetting: from basics to applications”. In: *Journal of Physics: Condensed Matter* 17.28 (July 2005). [doi:10.1088/0953-8984/17/28/r01], R705–R774. URL: https://doi.org/10.1088%2F0953-8984%2F17%2F28%2Fr01.

[112] IEEE Spectrum. *The Electrowetting Display*. Jan. 2, 2013. URL: https://www.youtube.com/watch?v=Bf1GjCaYzYg (visited on 09/25/2023).

[113] Min Zhou et al. “Simplified dynamical model for optical response of electrofluidic displays”. In: *Displays* 49 (Sept. 2017). [doi:10.1016/j.displa.2017.05.003], pp. 26–34. URL: https://doi.org/10.1016%2Fj.displa.2017.05.003.

[114] E. M. Barston. “Comments on “Electrohydrodynamic Rayleigh-Taylor Bulk Instability””. In: *The Physics of Fluids* 13.11 (Nov. 1970). [doi:10.1063/1.1692876], pp. 2876–2878. URL: https://doi.org/10.1063%2F1.1692876.

[115] Li Wang et al. “Driving Scheme Optimization for Electrowetting Displays Based on Contact Angle Hysteresis to Achieve Precise Gray-Scales”. In: *Frontiers in Physics* 9 (Mar. 2021). [doi:10.3389/fphy.2021.655547]. URL: https://doi.org/10.3389%2Ffphy.2021.655547.

[116] F. Li and F. Mugele. “How to make sticky surfaces slippery: Contact angle hysteresis in electrowetting with alternating voltage”. In: *Applied Physics Letters* 92.24 (June 2008). [doi:10.1063/1.2945803]. URL: https://doi.org/10.1063%2F1.2945803.

[117] Yi-Cheng Chen et al. “56.3: A Charge Trapping Suppression Method for Quick Response Electrowetting Displays”. In: *SID Symposium Digest of Technical Papers* 41.1 (2010). [doi:10.1889/1.3500607], p. 842. URL: https://doi.org/10.1889%2F1.3500607.

[118] John R. Platt. “Electrochromism, a Possible Change of Color Producible in Dyes by an Electric Field”. In: *The Journal of Chemical Physics* 34.3 (Mar. 1961). [doi:10.1063/1.1731686], pp. 862–863. URL: https://doi.org/10.1063%2F1.1731686.

[119] S. K. Deb. “A Novel Electrophotographic System”. In: *Applied Optics* 8.S1 (Jan. 1969). [doi:10.1364/ao.8.s1.000192], p. 192. URL: https://doi.org/10.1364%2Fao.8.s1.000192.

[120] J.S.E.M. Svensson and C.G. Granqvist. “Electrochromic tungsten oxide films for energy efficient windows”. In: *Solar Energy Materials* 11.1-2 (Oct. 1984). [doi:10.1016/0165-1633(84)90025-x], pp. 29–34. URL: https://doi.org/10.1016%2F0165-1633%2884%2990025-x.

[121] Carl M. Lampert. “Electrochromic materials and devices for energy efficient windows”. In: *Solar Energy Materials* 11.1-2 (Oct. 1984). [doi:10.1016/0165-1633(84)90024-8], pp. 1–27. URL: https://doi.org/10.1016%2F0165-1633%2884%2990024-8.

[122] Carl M. Lampert. “&lttitle&gtThe world of large-area glazing and displays&lt/title&gt”. In: *SPIE Proceedings*. Ed. by Carl M. Lampert. [doi:10.1117/12.365772]. SPIE, Oct. 1999. URL: https://doi.org/10.1117%2F12.365772.

[123] C.M. Lampert. “Large-area smart glass and integrated photovoltaics”. In: *Solar Energy Materials and Solar Cells* 76.4 (Apr. 2003). [doi:10.1016/s0927-0248(02)00259-3], pp. 489–499. URL: https://doi.org/10.1016%2Fs0927-0248%2802%2900259-3.

[124] Anna M. Österholm et al. “Four Shades of Brown: Tuning of Electrochromic Polymer Blends Toward High-Contrast Eyewear”. In: *ACS Applied Materials &amp Interfaces* 7.3 (Jan. 2015). [doi:10.1021/am507063d], pp. 1413–1421. URL: https://doi.org/10.1021%2Fam507063d.

[125] Yanan Wang et al. “Pulsed electrochemical deposition of porous WOsub3/sub on silver networks for highly flexible electrochromic devices”. In: *Journal of Materials Chemistry C* 7.7 (2019). [doi:10.1039/c8tc05698f], pp. 1966–1973. URL: https://doi.org/10.1039%2Fc8tc05698f.

[126] Hongtao Yu et al. “Side-chain engineering of green color electrochromic polymer materials: toward adaptive camouflage application”. In: *Journal of Materials Chemistry C* 4.12 (2016). [doi:10.1039/c6tc00197a], pp. 2269–2273. URL: https://doi.org/10.1039%2Fc6tc00197a.

[127] *Post-Synthetic Color Tuning of the Ultra-Effective and Highly Stable Surface-Confined Electrochromic Monolayer: Shades of Green for Camouflage Materials*. [doi:10.1021/acsami.1c09863.s001]. URL: https://doi.org/10.1021%2Facsami.1c09863.s001.

[128] Casey R. Wade, Minyuan Li, and Mircea Dincă. “Facile Deposition of Multicolored Electrochromic Metal-Organic Framework Thin Films”. In: *Angewandte Chemie International Edition* 52.50 (Oct. 2013). [doi:10.1002/anie.201306162], pp. 13377–13381. URL: https://doi.org/10.1002%2Fanie.201306162.

[129] Yu-Mo Zhang et al. “A single-molecule multicolor electrochromic device generated through medium engineering”. In: *Light: Science &amp Applications* 4.2 (Feb. 2015). [doi:10.1038/lsa.2015.22], e249–e249. URL: https://doi.org/10.1038%2Flsa.2015.22.

[130] Lukas Niklaus et al. “Redox Electrolytes for Hybrid Type II Electrochromic Devices with Fe-MEPE or Nisub1-ix/i/subO as Electrode Materials”. In: *ChemElectroChem* 7.15 (July 2020). [doi:10.1002/celc.202000583], pp. 3274–3283. URL: https://doi.org/10.1002%2Fcelc.202000583.

[131] Shankar Bogati, Andreas georg, and Wolfgang Graf. “Sputtered Si3N4 and SiO2 electron barrier layer between a redox electrolyte and the WO3 film in electrochromic devices”. In: *Solar Energy Materials and Solar Cells* 159 (Jan. 2017). [doi:10.1016/j.solmat.2016.08.023], pp. 395–404. URL: https://doi.org/10.1016%2Fj.solmat.2016.08.023.

[132] Shankar Bogati, Rabin Basnet, and Andreas Georg. “Iridium oxide catalyst for hybrid electrochromic device based on tetramethylthiourea (TMTU) redox electrolyte”. In: *Solar Energy Materials and Solar Cells* 189 (Jan. 2019). [doi:10.1016/j.solmat.2018.09.026], pp. 206–213. URL: https://doi.org/10.1016%2Fj.solmat.2018.09.026.

[133] Yuyang Wang et al. “A multicolour bistable electronic shelf label based on intramolecular proton-coupled electron transfer”. In: *Nature Materials* 18.12 (Sept. 2019). [doi:10.1038/s41563-019-0471-8], pp. 1335–1342. URL: https://doi.org/10.1038%2Fs41563-019-0471-8.

[134] Xiaojun Wang et al. “Reversible bond/cation-coupled electron transfer on phenylenediamine-based rhodamine B and its application on electrochromism”. In: *ACS Applied Materials & Interfaces* 9.23 (2017). [doi:10.1021/acsami.7b03199.s001], pp. 20196–20204.

[135] Haijin Shin et al. “Energy saving electrochromic windows from bistable low-HOMO level conjugated polymers”. In: *Energy &amp Environmental Science* 9.1 (2016). [doi:10.1039/c5ee03160e], pp. 117–122. URL: https://doi.org/10.1039%2Fc5ee03160e.

[136] Tyler S Hernandez et al. “Bistable black electrochromic windows based on the reversible metal electrodeposition of Bi and Cu”. In: *ACS Energy Letters* 3.1 (2017). [doi:10.1021/acsenergylett.7b01072.s001], pp. 104–111.

[137] Shengliang Zhang et al. “Alsup3/sup intercalation/de-intercalation-enabled dual-band electrochromic smart windows with a high optical modulation, quick response and long cycle life”. In: *Energy &amp Environmental Science* 11.10 (2018). [doi:10.1039/c8ee01718b], pp. 2884–2892. URL: https://doi.org/10.1039%2Fc8ee01718b.

[138] Zhiguang Sun and Yurui Fang. “Fabry-Pérot Interference Cavity Length Tuned by Plasmonic Nanoparticle Metasurface for Nanophotonic Device Design”. In: *ACS Applied Nano Materials* 3.11 (Oct. 2020). [doi:10.1021/acsanm.0c01967], pp. 10732–10738. URL: https://doi.org/10.1021%2Facsanm.0c01967.

[139] Marika Gugole et al. “Electrochromic inorganic nanostructures with high chromaticity and superior brightness”. In: *Nano Letters* 21.10 (2021). [doi:10.1021/acs.nanolett.1c00904.s002], pp. 4343–4350.

[140] Ting Xu et al. “High-contrast and fast electrochromic switching enabled by plasmonics”. In: *Nature Communications* 7.1 (2016), p. 10479.

[141] Tohru Yashiro et al. “Flexible electrochromic display”. In: *Proc. IDW*. Vol. 13. 2013, pp. 1300–1303.

[142] Bo-Han Chen et al. “Printed Multicolor High-Contrast Electrochromic Devices”. In: *ACS Applied Materials &amp Interfaces* 7.45 (Nov. 2015). [doi:10.1021/acsami.5b08061], pp. 25069–25076. URL: https://doi.org/10.1021%2Facsami.5b08061.

[143] Kunli Xiong et al. “Electronic Paper: Plasmonic Metasurfaces with Conjugated Polymers for Flexible Electronic Paper in Color (Adv. Mater. 45/2016)”. In: *Advanced Materials* 28.45 (Dec. 2016). [doi:10.1002/adma.201670318], pp. 10103–10103. URL: https://doi.org/10.1002%2Fadma.201670318.

[144] Norihisa Kobayashi et al. “Organic electrochromism for a new color electronic paper”. In: *Solar Energy Materials and Solar Cells* 92.2 (Feb. 2008). [doi:10.1016/j.solmat.2007.02.027], pp. 136–139. URL: https://doi.org/10.1016%2Fj.solmat.2007.02.027.

[145] Tohru Yashiro et al. “Flexible Electrochromic Display”. en. In: ().

[146] Seung Il Cho et al. “Nanotube-based ultrafast electrochromic display”. In: *Advanced Materials* 17.2 (2005). [doi:10.1002/adma.200400499], pp. 171–175.

[147] Matthias Wuttig. “Towards a universal memory?” In: *Nature Materials* 4.4 (Apr. 2005). [doi:10.1038/nmat1359], pp. 265–266. URL: https://doi.org/10.1038%2Fnmat1359.

[148] Harish Bhaskaran and Peiman HOSSEINI. “Display device based on phase-change materials”. en. US20170031231A1. Feb. 2017. URL: https://patents.google.com/patent/US20170031231A1/en (visited on 11/30/2022).

[149] Christine Koch et al. “Investigating the Influence of Resonant Bonding on the Optical Properties of Phase Change Materials (GeTe)subix/i/subSnSbsub2/subSesub4/sub”. In: *Chemistry of Materials* 29.21 (Oct. 2017). [doi:10.1021/acs.chemmater.7b03299], pp. 9320–9327. URL: https://doi.org/10.1021%2Facs.chemmater.7b03299.

[150] Stanford R. Ovshinsky. “Reversible Electrical Switching Phenomena in Disordered Structures”. In: *Disordered Materials*. [doi:10.1007/978-1-4684-8745-9$_2$]. Springer US, 1991, pp. 11–13. URL: https://doi.org/10.1007%2F978-1-4684-8745-9_2.

[151] Eiji Ohno et al. “TeGeSnAu Alloys for Phase Change Type Optical Disk Memories”. In: *Japanese Journal of Applied Physics* 28.7R (July 1989). [doi:10.1143/jjap.28.1235], p. 1235. URL: https://doi.org/10.1143%2Fjjap.28.1235.

[152] Peiman Hosseini, C. David Wright, and Harish Bhaskaran. “An optoelectronic framework enabled by low-dimensional phase-change films”. In: *Nature* 511.7508 (July 2014). [doi:10.1038/nature13487], pp. 206–211. URL: https://doi.org/10.1038%2Fnature13487.

[153] Peiman Hosseini, C David Wright, and Harish Bhaskaran. “An optoelectronic framework enabled by low-dimensional phase-change films”. In: *Nature* 511.7508 (2014). [doi:10.1038/nature13487], pp. 206–211.

[154] Mikhail A Kats et al. “Nanometre optical coatings based on strong interference effects in highly absorbing media”. In: *Nature materials* 12.1 (2013). [doi:10.1038/nmat3443], pp. 20–24.

[155] Kostiantyn Shportko et al. “Resonant bonding in crystalline phase-change materials”. In: *Nature Materials* 7.8 (July 2008). [doi:10.1038/nmat2226], pp. 653–658. URL: https://doi.org/10.1038%2Fnmat2226.

[156] Kostiantyn Shportko et al. “Resonant bonding in crystalline phase-change materials”. In: *Nature materials* 7.8 (2008). [doi:10.1038/nmat2226], pp. 653–658.

[157] Ben Broughton et al. “38-4: solid-state reflective displays (SRD®) utilizing ultrathin phase-change materials”. In: *SID Symposium Digest of Technical Papers*. Vol. 48. 1. Wiley Online Library. 2017, pp. 546–549.

[158] Sergio Garcia Castillo et al. “57-4: solid state reflective display (SRD®) with LTPS Diode backplane”. In: *SID Symposium Digest of Technical Papers*. Vol. 50. 1. [doi:10.1002/sdtp.13044]. Wiley Online Library. 2019, pp. 807–810.

[159] Omid Hemmatyar et al. “Advanced phase-change materials for enhanced meta-displays”. In: *arXiv preprint arXiv:2105.01313* (2021).

[160] Tong Zhou et al. “Electrically Tunable Non-volatile Reflective Display Pixel Structure Based on Phase Change Material”. In: *Journal of Physics: Conference Series* 1544.1 (May 2020). [doi:10.1088/1742-6596/1544/1/012034], p. 012034. URL: https://doi.org/10.1088%2F1742-6596%2F1544%2F1%2F012034.

[161] Eli Yablonovitch. “Inhibited spontaneous emission in solid-state physics and electronics”. In: *Physical review letters* 58.20 (1987). [doi:10.1103/physrevlett.58.2059], p. 2059.

[162] Sajeev John. “Strong localization of photons in certain disordered dielectric superlattices”. In: *Physical review letters* 58.23 (1987). [doi:10.1103/physrevlett.58.2486], p. 2486.

[163] Zaky A. Zaky and Arafa H. Aly. “Novel smart window using photonic crystal for energy saving”. In: *Scientific Reports* 12.1 (June 2022). [doi:10.1038/s41598-022-14196-9]. URL: https://doi.org/10.1038%2Fs41598-022-14196-9.

[164] Hui Wang and Ke-Qin Zhang. “Photonic crystal structures with tunable structure color as colorimetric sensors”. In: *Sensors* 13.4 (2013). [doi:10.3390/s130404192], pp. 4192–4213.

[165] Geoffrey A Ozin and Andre C Arsenault. “P-Ink and Elast-Ink from lab to market”. In: *Materials Today* 11.7-8 (2008). [doi:10.1016/s1369-7021(08)70148-2], pp. 44–51.

[166] Insook Lee et al. “Quasi-amorphous colloidal structures for electrically tunable full-color photonic pixels with angle-independency”. In: *Advanced Materials* 22.44 (2010). [doi:10.1002/adma.201001954], pp. 4973–4977.

[167] Chongjun Jin et al. “Photonic gap in amorphous photonic materials”. In: *Physical Review B* 63.19 (2001). [doi:10.1103/physrevb.63.195107], p. 195107.

[168] Kazuhide Ueno et al. “A soft glassy colloidal array in ionic liquid, which exhibits homogeneous, non-brilliant and angle-independent structural colours”. In: *Chemical communications* 24 (2009). [doi:10.1039/b905108b], pp. 3603–3605.

[169] Yiquan Fang et al. “In Situ Dynamic Study of Color-Changing in Liquid Colloidal Crystals for Electrophoretic Displays”. In: *ACS Applied Nano Materials* 5.8 (2022). [doi:10.1021/acsanm.2c02391], pp. 11249–11261.

[170] Gaowen Chen et al. “Development of bright and low angle dependence structural colors from order-disorder hierarchical photonic structure”. In: *Dyes and Pigments* 161 (2019). [doi:10.1016/j.dyepig.2018.09.039], pp. 464–469.

[171] Nicolas Vogel et al. “Color from hierarchy: Diverse optical properties of micron-sized spherical colloidal assemblies”. In: *Proceedings of the National Academy of Sciences* 112.35 (2015). [doi:10.1073/pnas.1506272112], pp. 10845–10850.

[172] Ken Werner. “LA Chapter’s One-Day Conference Covers North American Display Activity”. In: *Information Display* 35.4 (2019), pp. 34–36.

[173] Ming Wang et al. “59.1: Invited paper: electrophoretic display platform comprising B, W, R particles”. In: *SID Symposium Digest of Technical Papers*. Vol. 45. 1. Wiley Online Library. 2014, pp. 857–860.

[174] Wieger Markvoort, Hjalmar Edzer Ayco Huitema, and Leendert Mark Hage. *Sequential addressing of displays*. US Patent 8,866,733. Oct. 2014.

[175] Asad Khan et al. “Recent advances and product enhancements in reflective cholesteric displays”. In: *Emerging Liquid Crystal Technologies* 5741 (2005). [doi:10.1117/12.591065], pp. 1–6.

[176] Ming Zheng Duan et al. “A reflective display technology based on electrofluidics”. In: *Applied Mechanics and Materials* 670 (2014). [doi:10.4028/www.scientific.net/amm.670-671.976], pp. 976–981.

[177] David Corr et al. “Coloured electrochromic “paper-quality” displays based on modified mesoporous electrodes”. In: *Solid State Ionics* 165.1-4 (2003). [doi:10.1016/j.ssi.2003.08.054], pp. 315–321.

[178] *Ink epaper ED103TC2 Datasheet*. URL: https://www.data-modul.com/sites/default/files/products/VB3300-KCD-specification-12051789.pdf.

[179] Robert Fleming et al. “48-2: Electronic Paper 2.0: Frustrated eTIR as a Path to Color and Video”. In: *SID Symposium Digest of Technical Papers*. Vol. 49. 1. Wiley Online Library. 2018, pp. 630–632.

[180] Ik Jang Ko et al. “An optically efficient full-color reflective display with an electrochromic device and color production units”. In: *Journal of Information Display* 20.3 (July 2019). [doi:10.1080/15980316.2019.1649310], pp. 155–160. URL: https://doi.org/10.1080%2F15980316.2019.1649310.

[181] SJ Wilson and MC Hutley. “The optical properties of’moth eye’antireflection surfaces”. In: *Optica Acta: International Journal of Optics* 29.7 (1982), pp. 993–1009.

[182] Tomoya Yano, Hiroyuki Sugawara, and Jun Taniguchi. “Moth-eye structured mold using sputtered glassy carbon layer for large-scale applications”. In: *Micro and Nano Engineering* 9 (2020), p. 100077.

[183] Hemant Kumar Raut et al. “Anti-reflective coatings: A critical, in-depth review”. In: *Energy & Environmental Science* 4.10 (2011). [doi:10.1039/c1ee01297e], pp. 3779–3804.

[184] *The NEW rE Monitor by SVD - Our 32” RLCD with more connectivity!* en. URL: https://www.sunvisiondisplay.com/product/The-NEW-rE-Monitor-Featuring-32-Color-RLCD-Technology (visited on 09/23/2023).

[185] *Modal and C Methods Grating Software*. 2023. URL: https://mcgrating.com/ (visited on 09/16/2023).

[186] Dorian Herle. *MC_Grating_Advanced_Python*. original-date: 2023-06-27T08:59:55Z. June 28, 2023. URL: https://github.com/dorianherle/MC_Grating_Advanced_Python (visited on 09/16/2023).

[187] Xiaohui Hu, R.C. Eberhart, and Yuhui Shi. “Engineering optimization with particle swarm”. In: *Proceedings of the 2003 IEEE Swarm Intelligence Symposium. SIS’03 (Cat. No.03EX706)* (2003), pp. 53–57. DOI: 10.1109/SIS.2003.1202247.

[188] *Particle swarm optimization (PSO) with constraint support — pyswarm 0.6 documentation*. URL: https://pythonhosted.org/pyswarm/ (visited on 09/16/2023).

[189] *A Standard Default Color Space for the Internet - sRGB*. URL: https://www.w3.org/Graphics/Color/sRGB.html (visited on 09/16/2023).

[190] *IEC 61966-2-1:1999 | IEC Webstore*. URL: https://webstore.iec.ch/publication/6169 (visited on 09/16/2023).

[191] G. Ke et al. “LightGBM: A Highly Efficient Gradient Boosting Decision Tree”. In: *Advances in Neural Information Processing Systems* 30 (2017), pp. 3149–3157. URL: https://www.microsoft.com/en-us/research/wp-content/uploads/2017/11/lightgbm.pdf.

[192] Emmanuel Saucedo-Flores et al. “Study of the pull-in voltage for MEMS parallel plate capacitor actuators”. In: *MRS Online Proceedings Library (OPL)* 782 (2003), A5–86.

[193] Gabriel M Rebeiz. *RF MEMS: theory, design, and technology*. John Wiley & Sons, 2004.

[194] Dorian Herle et al. “Broadband Mechanically Tunable Metasurface Reflectivity Modulator in the Visible Spectrum”. In: *ACS photonics* (2023).

[195] Stefan Mühlig et al. “Multipole analysis of meta-atoms”. In: *Metamaterials* 5.2-3 (2011), pp. 64–73.

[196] Benjamin Gallinet, Andreas M Kern, and Olivier JF Martin. “Accurate and versatile modeling of electromagnetic scattering on periodic nanostructures with a surface integral approach”. In: *JOSA A* 27.10 (2010), pp. 2261–2271.

[197] Andreas M Kern and Olivier JF Martin. “Surface integral formulation for 3D simulations of plasmonic and high permittivity nanostructures”. In: *JOSA A* 26.4 (2009), pp. 732–740.

[198] Marco Riccardi et al. “Multipolar expansions for scattering and optical force calculations beyond the long wavelength approximation”. In: *Physical Review B* 106.11 (2022), p. 115428.

[199] Daniel T Pierce and Wo E Spicer. “Electronic structure of amorphous Si from photoemission and optical studies”. In: *Physical Review B* 5.8 (1972), p. 3017.

[200] B Lukyanchuk et al. “Colossal magnetic fields in high refractive index materials at microwave frequencies”. In: *Scientific Reports* 11.1 (2021), p. 23453.

[201] Hsiang-Chu Wang and Olivier JF Martin. “Pitfalls in the spectral measurements of polarization-altering metasurfaces”. In: *Applied Optics* 61.27 (2022), pp. 8100–8107.

[202] Nguyen Van Dong, Y Fournier, and JY Le Ny. “Electrical and optical properties of sputtered amorphous silicon films prepared under a reduced pumping speed”. In: *Applied physics letters* 42.7 (1983), pp. 594–596.

[203] Michael Totzeck et al. “Pushing deep ultraviolet lithography to its limits”. In: *nature photonics* 1.11 (2007), pp. 629–631.

[204] Jon Tomas Gudmundsson and Daniel Lundin. “Introduction to magnetron sputtering”. In: *High power impulse magnetron sputtering*. Elsevier, 2020, pp. 1–48.

[205] Stephen A Campbell. “Fabrication engineering at the micro-and nanoscale”. In: *(No Title)* (2008).

[206] Jeffrey Cook. “Angular distribution of sputtered atoms in physical vapor deposition and collimated sputtering”. In: *Thin Solid Films* 338.1-2 (1999), pp. 81–87.

[207] M Hasegawa and K Nanbu. “Numerical analysis of film growth and step coverage in the collimation sputtering method”. In: *Vacuum* 48.10 (1997), pp. 825–831.

[208] Daniel Lundin and Kostas Sarakinos. “An introduction to thin film processing using high-power impulse magnetron sputtering”. In: *Journal of Materials Research* 27.5 (2012), pp. 780–792.

[209] Jiangnan Si et al. “Broadened angle-insensitive near-perfect absorber based on mie resonances in amorphous silicon metasurface”. In: *Nanomaterials* 10.9 (2020), p. 1733.

[210] Henzen Alex et al. “Introduction of a New Disruptive Display Technology in the Existing Display Manufacturing Infrastructure”. In: *Proceedings of the International Display Workshops*. [doi:10.36463/idw.2020.0739]. 2020, p. 739.

[211] J Heikenfeld et al. “Electrofluidic displays using Young–Laplace transposition of brilliant pigment dispersions”. In: *Nature Photonics* 3.5 (2009). [doi:10.1038/nphoton.2009.68], pp. 292–296.

[212] Mingliang Jin et al. “Optofluid-based reflective displays”. In: *Micromachines* 9.4 (2018). [doi:10.3390/mi9040159], p. 159.

[213] Chang Gu et al. “Emerging electrochromic materials and devices for future displays”. In: *Chemical Reviews* 122.18 (2022), pp. 14679–14721.

[214] Qianqian Fu et al. “Electrically responsive photonic crystals with bistable states for low-power electrophoretic color displays”. In: *Nature Communications* 13.1 (2022). [doi:10.1038/s41467-022-34745-0], p. 7007.

A

Appendix

A.1. State of the art - Comparison Table

Type	Reflectance (%)	Contrast	Frequency (Hz)	Dots Per Inch (DPI)	Refresh Energy Density (mJ/cm^2)
Electrophoretic Microcapsule	35[173] 44[172] 43[178]	23[173] 15[172] 14[178]	2.1[174]	226[178]	0.58[178]
Electrophoretic Total Internal Reflection	55[65] 83[179] 40[67]	20[179] 16[67]	28[65] 30[179]	212[179] 227[67]	0.029[67]
LCD Reflective	9[184]	25[184]	60[184]	69[184]	0.03[184]
LCD Cholesteric	30[175] 35[91]	10[175] 25[91]	0.8[91]	100[91]	4.7[91]
Electrowetting	40[210] 65[176] 55[211]	1.7[176] 3.3[31]	62[176] 56[31]	N/A	0.013[210]
MEMS Interferometric Modulator	17[103]	80%[103]	40 Hz[212]	224[103]	0.05[103]
MEMS Continuous Color Reflective	90[99]	30[101]	120[101]	364[101]	0.004[101]
Phase Change	44[160]	2.5[160]	2[41]	N/A	104[160]
Electrochromic	40[177] 47[180]	12[177] 10[180]	1[177]	200[213]	1.1[180]
Tunable Photonic Crystals	60-30[169]	N/A	1[169] 0.125[214] 20[30]	N/A	N/A

Table A.1: Comparative study of performance metrics of reflective display technologies

The refresh energy density is usually not directly given in the references cited but is computed from given power consumption, active area, and frame refresh time. Since some technologies are more experimental, not all data is available.

A.2. Derivation of reflection form hemisphere

The amount of light reflected at an interface between two media with different refractive indices, n_1, and n_2, can be derived using the Fresnel equations. The power reflection for s and p polarized light can be derived using the Fresnel Equations and Snell's law. For s-polarized light, the reflection coefficient R_S is given by:

$$R_S = \left(\frac{n_1 \cos(\theta_1) - n_2 \cos(\theta_2)}{n_1 \cos(\theta_1) + n_2 \cos(\theta_2)} \right)^2 \tag{A.1}$$

For p-polarized light, the reflection coefficient R_p is given by:

$$R_p = \left(\frac{n_1 \cos(\theta_2) - n_2 \cos(\theta_1)}{n_1 \cos(\theta_2) + n_2 \cos(\theta_1)} \right)^2 \tag{A.2}$$

In many cases, when analyzing the effects of light, it is necessary to consider unpolarized light. This type of light is composed of equal parts of both the s and p polarizations, resulting in an effective reflectivity that is the average of the two reflectivities.

$$R_{\text{eff}} = \frac{1}{2}(R_S + R_S) \tag{A.3}$$

Under normal incidence, the equation for the reflection R can be simplified to:

$$R_{\text{eff}} = \left(\frac{n_1 - n_2}{n_1 + n_2}\right)^2 \tag{A.4}$$

Clearink does not use a flat surface as a reflective element, but a semi-sphere:

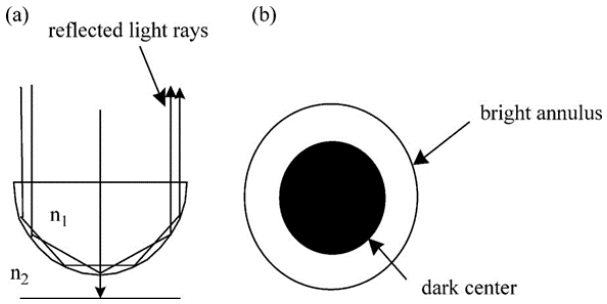

Figure A.1: Hemisphere as TIR element. (a) Schematic cross-section showing of total reflected light within a semi-sphere, (b) top view showing bright region (TIR) and dark center (transmission) [65]

The fractional amplitude between reflected light (due to total internal reflection) and the transmitted light is equal to the ratio of the bright area to the total hemisphere area.

$$r = \frac{A_{\text{Bright}}}{A_{\text{Total}}} \tag{A.5}$$

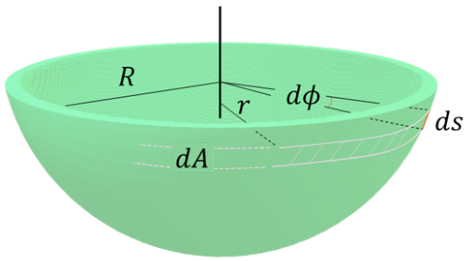

Figure A.2: Schematic representation of a hemisphere with radius R, distance from center line r, $1D$ segment ds, spanned by the infinitesimal angle $d\phi$, and the infinitesimal strip area dA.

In general, the area of a slice of the hemisphere is:

$$\begin{aligned} dA &= 2\pi r ds = 2\pi r R d\phi = 2\pi R^2 \cos(\phi) d\phi \\ A &= \int_0^{\phi} 2\pi R^2 \cos(\phi) d\phi = 2\pi R^2 \sin(\phi) \end{aligned} \tag{A.6}$$

Relating ϕ to the incidence angle θ between light rays and surface normal:

$$\phi = \frac{\pi}{2} - \theta \tag{A.7}$$

We get:

$$A = 2\pi R^2 \cos(\phi) \tag{A.8}$$

The area in which total reflection occurs, A_{Bright}, is:

$$A_{\text{Bright}} = 2\pi R^2 \cos\left(\arcsin\left(\frac{n_2}{n_1}\right)\right) = 2\pi R^2 \sqrt{1 - \left(\frac{n_2}{n_1}\right)^2} \tag{A.9}$$

The fractional amplitude thus becomes:

$$r = \frac{A_{\text{Bright}}}{A_{\text{Total}}} = \sqrt{1 - \left(\frac{n_2}{n_1}\right)^2} \tag{A.10}$$

The fractional amplitude coefficient r must be squared to get reflection intensity for normal incident light:

$$\boxed{R = 1 - \left(\frac{n_2}{n_1}\right)^2} \tag{A.11}$$

A.3. Modified pyswarm Python package

```
from __future__ import division
import numpy as np
import sys
import re
import time

import matplotlib.pyplot as plt
import matplotlib
matplotlib.use('Qt5Agg')

def pso(func, lb, ub,initial_param=[], ieqcons=[], f_ieqcons=None, args=(), kwargs={},
        swarmsize=100, omega=0.5, phip=0.5, phig=0.5, maxiter=100,
        minstep=1e-8, minfunc=1e-8, debug=False, use_initial_param=False, plot_score=False):
    """
    Perform a particle swarm optimization (PSO)

    Parameters
    ==========
    func : function
        The function to be minimized
    lb : array
        The lower bounds of the design variable(s)
    ub : array
        The upper bounds of the design variable(s)

    Optional
    ========
    ieqcons : list
        A list of functions of length n such that ieqcons[j](x,*args) >= 0.0 in
        a successfully optimized problem (Default: [])
    f_ieqcons : function
        Returns a 1-D array in which each element must be greater or equal
        to 0.0 in a successfully optimized problem. If f_ieqcons is specified,
        ieqcons is ignored (Default: None)
    args : tuple
        Additional arguments passed to objective and constraint functions
        (Default: empty tuple)
    kwargs : dict
        Additional keyword arguments passed to objective and constraint
        functions (Default: empty dict)
    swarmsize : int
        The number of particles in the swarm (Default: 100)
    omega : scalar
        Particle velocity scaling factor (Default: 0.5)
    phip : scalar
        Scaling factor to search away from the particle's best-known position
        (Default: 0.5)
```

```
    phig : scalar
        Scaling factor to search away from the swarm's best known position
        (Default: 0.5)
    maxiter : int
        The maximum number of iterations for the swarm to search (Default: 100)
    minstep : scalar
        The minimum stepsize of swarm's best position before the search
        terminates (Default: 1e-8)
    minfunc : scalar
        The minimum change of swarm's best objective value before the search
        terminates (Default: 1e-8)
    debug : boolean
        If True, progress statements will be displayed every iteration
        (Default: False)

    Returns
    =======
    g : array
        The swarm's best known position (optimal design)
    f : scalar
        The objective value at ``g``

    """
    scores = []

    f = open("log_file.txt",'w+',encoding='utf8')
    f.close()



    assert len(lb)==len(ub), 'Lower- and upper-bounds must be the same length'
    assert hasattr(func, '__call__'), 'Invalid function handle'
    lb = np.array(lb)
    ub = np.array(ub)
    assert np.all(ub>lb), 'All upper-bound values must be greater than lower-bound values'

    vhigh = np.abs(ub - lb)
    vlow = -vhigh

    # Check for constraint function(s) #########################################
    obj = lambda x: func(x, *args, **kwargs)
    if f_ieqcons is None:
        if not len(ieqcons):
            if debug:
                print('No constraints given.')
            cons = lambda x: np.array([0])
        else:
            if debug:
                print('Converting ieqcons to a single constraint function')
            cons = lambda x: np.array([y(x, *args, **kwargs) for y in ieqcons])
    else:
        if debug:
            print('Single constraint function given in f_ieqcons')
        cons= lambda x: np.array(f_ieqcons(x, *args, **kwargs))

    def is_feasible(x): # ADDED np.floor() !!
        check = np.all(cons(np.floor(x))>=0)
        if check is not True:
            return check

    # Initialize the particle swarm ############################################
```

```
    S = swarmsize
    D = len(lb)  # the number of dimensions each particle has

    initial_outside_range = False

    # INITIAL PARAMETERS
    if use_initial_param:
        print("Using Initial Parmeters")
        print("-----------------------")
        print("-----------------------")

        x_initial = np.array([])

        for i in range(D):

            #Check if initial parameters are within bounds
            if  initial_param[i]-lb[i] < 0 or ub[i] - initial_param[i] <0:
                initial_outside_range = True
                sys.exit("Initial Parameters Are Outside Of Upper Or Lower Bounds")

            x_initial=np.append(x_initial ,(lb[i] - initial_param[i])/(lb[i] - ub[i]))

        x_random = np.random.rand(S-1, D)
        # particle positions -> values between 0 and 1,used to find particles within the
            upper and lower bounds afterwards
        x = np.vstack((x_initial, x_random))


    else:
        x = np.random.rand(S, D)  # particle positions -> values between 0 and 1,
        #used to find particles within the upper and lower bounds afterwards


    v = np.zeros_like(x)  # particle velocities
    p = np.zeros_like(x)  # best particle positions
    fp = np.zeros(S)  # best particle function values
    g = []  # best swarm position
    fg = 1e100  # artificial best swarm position starting value

    if plot_score:
        plt.figure()

    for i in range(S):


        # Initialize the particle's position
        x[i, :] = np.floor(lb + x[i, :]*(ub - lb)) # ADDED np.floor() !!

        # Initialize the particle's best known position
        p[i, :] = x[i, :]


        # Calculate the objective's value at the current particle's,
        # ONLY IF CONSTRAINTS ARE OK,
        # IF NOT -> ASSIGN EXTREMLY HIGH OBJECTIVE FUNCTION RESULT
        if is_feasible(p[i, :]):

            fp[i] = obj(p[i, :])

            if plot_score == True:
                # ADDED SCORES
```

```
                scores.extend([fp[i]])
                plt.plot(scores, marker=".", color="k")
                plt.pause(0.001)
        else:
            fp[i] = fg

        # SWARMS BEST POSITIOM
        # At the start, there may not be any feasible starting point, so just
        # give it a temporary "best" point since it's likely to change
        if i==0:
            g = p[0, :].copy()

        # If the current particle's position is better than the swarm's,
        # update the best swarm position
        if fp[i]<fg and is_feasible(p[i, :]):
            fg = fp[i]
            g = p[i, :].copy()

        # Initialize the particle's velocity
        v[i, :] = vlow + np.random.rand(D)*(vhigh - vlow)



    # Iterate until termination criterion met ##################################
    it = 1
    while it<=maxiter:

        rp = np.random.uniform(size=(S, D))
        rg = np.random.uniform(size=(S, D))
        for i in range(S):

            # Update the particle's velocity
            v[i, :] = omega*v[i, :] + phip*rp[i, :]*(p[i, :] - x[i, :]) + \
                      phig*rg[i, :]*(g - x[i, :])

            # Update the particle's position, correcting lower and upper bound
            # violations, then update the objective function value
            x[i, :] = np.floor(x[i, :] + v[i, :]) # ADDED np.floor() !!

            mark1 = x[i, :]<lb
            mark2 = x[i, :]>ub
            x[i, mark1] = lb[mark1]
            x[i, mark2] = ub[mark2]



            # Calculate the objective's value at the current particle's,
            # ONLY IF CONSTRAINTS ARE OK,
            # IF NOT -> ASSIGN EXTREMLY HIGH OBJECTIVE FUNCTION RESULT
            if is_feasible(x[i, :]):

                fx = obj(x[i, :])

                if plot_score == True:
                    # ADDED SCORES
                    scores.extend([fx])

                    plt.plot(scores, marker=".", color="k")
                    plt.pause(0.001)

```

```
            else:
                fx = fg


            # Compare particle's best position (if constraints are satisfied)
            if fx<fp[i] and is_feasible(x[i, :]):
                p[i, :] = x[i, :].copy()
                fp[i] = fx

                # Compare swarm's best position to current particle's position
                # (Can only get here if constraints are satisfied)
                if fx<fg:
                    if debug:
                        print(" ")
                        print("************************************************")
                        print('New best for swarm at iteration {:}: {:} {:}'.format(it, x[i,
                             :], fx))
                        print("************************************************")

                        f = open('log_file.txt','a',encoding='utf8')
                        f.write('New best for swarm at iteration {:}: {:} {:}'.format(it, x[
                            i, :], fx))
                        f.close()
                        print("storing in log file ")

                    tmp = x[i, :].copy()
                    stepsize = np.sqrt(np.sum((g-tmp)**2))
                    if np.abs(fg - fx)<=minfunc:

                        print('Stopping search: Swarm best objective change less than {:}'.
                            format(minfunc))
                        print("************************************************")
                        return tmp, fx
                    elif stepsize<=minstep:

                        print('Stopping search: Swarm best position change less than {:}'.
                            format(minstep))
                        print("************************************************")
                        return tmp, fx
                    else:
                        g = tmp.copy()
                        fg = fx




        if debug:
            print("************************************************")
            print('Best after iteration {:}: {:} {:}'.format(it, g, fg))
            print("************************************************")
            f = open('log_file.txt','a',encoding='utf8')
            f.write('Best after iteration {:}: {:} {:}'.format(it, g, fg))
            f.close()
        it += 1

    print('Stopping search: maximum iterations reached --> {:}'.format(maxiter))

    if not is_feasible(g):
        print("However, the optimization couldn't find a feasible design. Sorry")
    return g, fg
```

A.4. Spectrum to sRGB

```python
import colour
import numpy as np
def rgb_from_spectrum(wavelenghts,reflection_intensity):
    w_start = wavelenghts[0]
    w_end = wavelenghts[-1]

    spectrum_dict = dict(zip(wavelenghts,reflection_intensity))
    spd = colour.SpectralDistribution(spectrum_dict) #colour.SpectralPowerDistribution(
        spectrum_dict)
    # Interpolating the copied sample spectral power distribution.
    spd.interpolate(colour.SpectralShape(w_start, w_end, 1));
    cmfs = colour.MSDS_CMFS['CIE 1931 2 Degree Standard Observer']
    illuminant = colour.SDS_ILLUMINANTS['D65'] # colour.ILLUMINANTS_RELATIVE_SPDS['D65'] has
         been renamed
    # Calculating the sample spectral power distribution *CIE XYZ* tristimulus values.
    XYZ = colour.sd_to_XYZ(spd, cmfs, illuminant) # has been renamed ColourUsageWarning: "
        colour.spectral_to_XYZ" object has been renamed to "colour.sd_to_XYZ".
    # The output domain of *colour.spectral_to_XYZ* is [0, 100] and the input
    # domain of *colour.XYZ_to_sRGB* is [0, 1]. We need to take it in account and
    # rescale the input *CIE XYZ* colourspace matrix.
    sRGB = colour.XYZ_to_sRGB(XYZ / 100)

    # Clipping the values outside the sRGB boundary for plotting -> To avoid negative values
    # why ? https://github.com/colour-science/colour/issues/257
    sRGB_clip = np.clip(sRGB, 0, 1)

    return sRGB_clip
```

A.5. Reflectivity dip in the idle state of the measured spectrum

The discrepancy between the initial simulated reflection spectrum and the measured reflection spectrum in the idle state can be explained by a geometry difference between the designed and effectively fabricated structures. As SEM images and digital holographic (DHM) measurements reveal, the microbridge is buckled upwards in the idle state and its thickness is 80 nm instead of the designed 100 nm. Inputting these values into the RCWA simulation code reveals a closed match between the simulation and measured reflection spectra, as indicated in Figure A.3.

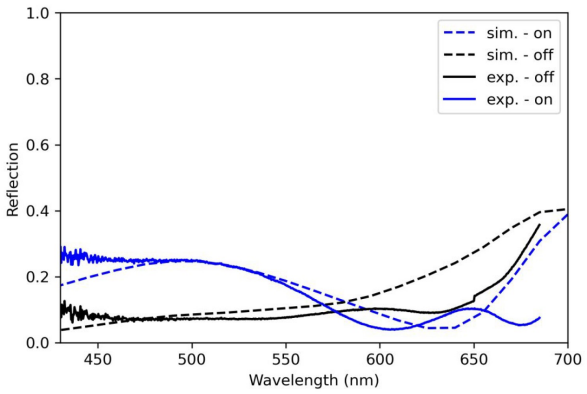

Figure A.3: Simulated and experimental reflection spectrum. Geometry: 80 nm buckled upwards, period: 400 nm, pillar diameter: 200 nm, trench: 50 nm, membrane thickness: 80 nm.

The reflectivity dip observed in the idle state of the measured spectrum - yielding the blue appearance of the pixels - can be explained by thin film destructive interference. Figure A.4 visualizes the simplified analytic model used.

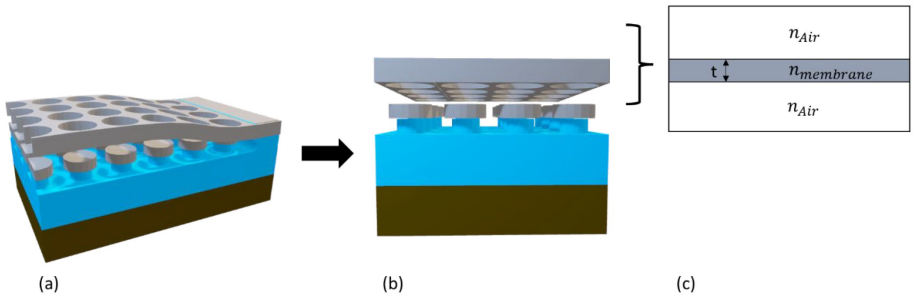

Figure A.4: Visualization of the simplified model - The buckled membrane (a) is simplified to a membrane with constant offset from the pillar (b), and further simplified (c) to represent an infinite slab of thickness t and equivalent refractive index $n_{membrane}$.

Through digital holographic measurements it can be shown that the membrane is buckled upwards in the idle state. Thus, most of its perforations are filled with air, leading to an approximate equivalent refractive index of 3 when taking the geometrical average:

$$\begin{aligned} n_{\text{membrane}} &= n_{aSi}\frac{\left(P^2-\frac{\pi}{4}H^2\right)}{A_{\text{total}}} + n_{\text{Air}}\frac{\frac{\pi}{4}H^2}{A_{\text{total}}} \\ &= 4.5\frac{400^2-\frac{\pi}{4}300^2}{400^2} + 1\frac{\frac{\pi}{4}300^2}{400^2} \\ &= 2.95 \approx 3 \end{aligned} \tag{A.12}$$

where P is the period and H is the diameter of a hole in the microbridge.

In the following we will assume an infinite slab of refractive index 3, surrounded (top/bottom) by air. For this configuration ($n_{\text{Air}} < n_{\text{Slab}} < n_{\text{Air}}$), destructive interference is given when the thickness of the slab equals to:

$$t = \frac{m\lambda}{2n} \tag{A.13}$$

for m = 1, 2, 3, ...

Thus, for m $= 1,$ n $= 3,$ and $\lambda = [500\,\text{nm} - 700\,\text{nm}]$ a destructive interference is obtained when the thickness is between 83 nm $- 117$ nm. As the thickness of the microbridge is within these values, this is a strong indication as to why a reflectivity dip is seen in the (buckled) ON state.

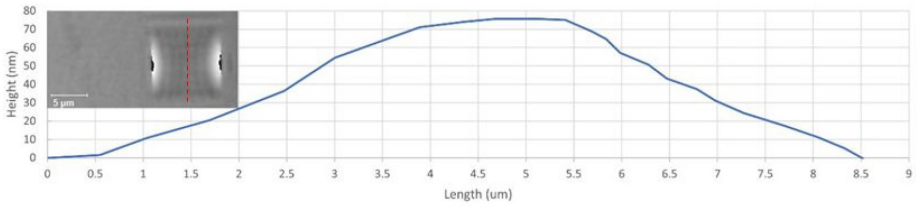

Figure A.5: Figure S6 Digital Holographic Microscopy measurement of the buckled membrane. A maximum amplitude of approx. 80nm deflection is measured at the centre of the membrane. Red dotted line: measurement line.

A.6. Runcard: Scalable Process Flow

Table A.2: Runcard for the Process

Step	Machine	Parameters
1	Oxford Instruments PlasmaPro 100, ICP CVD	200 nm Gate Oxide 100 nm PECVD aSi 100 nm PECVD SiO2 200 nm PECVD aSi 50 nm PECVD SiO2
2	Tepla, Z11	Recipe: 07 Abort after 5min
3	Spin Coat Ebeam Resist	CSAR 13 4000 rpm (300nm)
4	Raith EBPG5000+	Beam: 5nA Dose: 340 uC/cm^2
5	E-Beam Development	Amyl-Acetane: 1min30 ZEP Rinse: 1min Blow dry with nitrogen gun
6	Tepla, Z02	10s Low (descum)
7	SPTS Advanced Plasma System (APS)	`SiO2_PR_3:1`, 24s
8	Alcatel AMS 200 SE	`Si_Opto_HR_0deg`, 40s
9	SPTS Advanced Plasma System (APS)	`SiO2_PR_3:1`, 24s
10	PR Strip Wet	
11	Tepla, Z11	Recipe: 07 Abort after 5min
12	BENEQ TFS200 (ALD 1)	1.1 Angstrom/cycle
13	SPTS Advanced Plasma System (APS)	`SiO2_Soft` etch_depth = 2.58*etch_time-4.97
14	LPCVD aSi	350 nm No RCA (Has shown to etch ALD SiO2)
15	SEM Inspection	Measure thickness using SEM Cross-section
16	Veeco Nexus IBE350	Medium
17	SPTS uEtch	Recipe 1, Etch rate: 12 nm/min
18	LAB 600	1 nm Ti, 5nm Al